Energy Performance of Semi-transparent PV Modules for Applications in Buildings

Fung Yu Yan

A thesis submitted in partial fulfillment of the requirements for the Degree of Doctor of Philosophy

Department of Building Services Engineering

The Hong Kong Polytechnic University

May, 2006

CERTIFICATE OF ORIGINALITY

I hereby declare that this thesis is my own work and that, to the best of my knowledge and belief, it reproduces no material previously published or written, nor material that has been accepted for the award of any other degree or diploma, except where due acknowledgement has been made in the text.

_____ (Signed)

Fung Yu Yan (Name of student)

Department of Building Services Engineering

The Hong Kong Polytechnic University

Hong Kong, China

May, 2006

ABSTRACT

Abstract of thesis entitled	:	Energy Performance of Semi-transparent PV Modules for Applications in Buildings
Submitted by	:	Fung Yu Yan
For the degree of	:	Doctor of Philosophy

at The Hong Kong Polytechnic University in May, 2006.

Owing to the increasing awareness on energy conservation and environmental protection, building-integrated photovoltaic (BIPV) has been developed rapidly in the past decade. A number of research studies have been conducted on the energy performance of BIPV systems. However, most of the previous studies focused on the systems that incorporated with opaque type PV modules, little attention has been devoted to semi-transparent type PV modules, which have been commonly integrated in modern architectures. This thesis aims at evaluating the energy performance of the semi-transparent BIPV modules, including heat gains to the indoor environment, power generation from the PV modules and daylight utilization.

Solar radiation intensity on PV module's surfaces is an essential parameter for assessing energy performance of the PV modules. Different slope solar radiation models are analyzed and compared. The model that best suits Hong Kong situations is selected for the further development of the energy performance of the BIPV modules. The optimum orientation and tilted angle are determined in the analysis.

In addition to the solar radiation models, a detailed investigation on the heat gain through the semi-transparent BIPV modules is carried out in this study. A one-dimensional transient heat transfer model, the SPVHG model, for evaluating the

thermal performance of the semi-transparent BIPV modules is developed. The SPVHG model considers in detail the energy that is transmitted, absorbed and reflected in each element of the BIPV modules such as solar cells and glass layers. A computer program of the model is written accordingly. By applying the SPVHG model, the heat gain through the semi-transparent BIPV module of any thickness can be determined for any solar irradiance level. The annual performance can also be assessed by inputting annual weather data to the model.

In order to verify the SPVHG model, laboratory tests have been carried out on semi-transparent BIPV modules. A well-insulated calorimeter box and an adjustable steady-state type solar simulator which can provide up to 1600 W/m^2 have been used in the tests. Energy that transmitted through the semi-transparent BIPV modules and entered the calorimeter box was evaluated. It was found that the experimental results and the simulated results support each other. The SPVHG model is validated and can be used for further studies.

Other than heat transfer, power production and the daylight utilization are also the vital parts in the energy performance assessment of the semi-transparent BIPV module for applications in building facades. Power generation models of both opaque and semi-transparent BIPV modules are investigated in this study. In order to test the validity of the power generation model, measurements on a BIPV system of an existing building are carried out. The measurement results reveal a good validity of the power generation model. Only a minor modification to the model is required. The daylight utilization is evaluated by using an indoor illuminance model. The model estimates the mean internal illuminance on the working plane of a room when there is

both sunlight and skylight. Consequently, the power saving due to the daylight utilization can be determined.

By using the SPVHG model together with the power generation model and the indoor illuminance model, the energy performance, in terms of electricity benefit, of building facades that incorporated with semi-transparent BIPV modules is evaluated. Different scenarios are studied by changing various parameters such as the window to wall ratios, thickness and efficiency of the solar cells. The results show that the solar cells within the semi-transparent BIPV modules significantly reduce the solar heat gain and thus reduce the power consumption of air-conditioning systems. Taking into account the impacts of PV electricity generation and daylight utilization, the optimum solar cell area ratio in the PV modules varies from 0.7 to 0.9 for different window-to-wall ratios of the building façade. The largest net electricity benefit of the BIPV façade under the simulation conditions is around 120 kWh/m^2.

The SPVHG model developed in this study is a precise model for calculating the amount of heat gains through the semi-transparent BIPV modules. By considering also the power generation and daylight utilization, the electricity benefit of different BIPV façade configurations can be simulated. This information should help engineers predict the cooling load due to the BIPV façade and thus review their designs for energy efficiency optimization. On the whole, the results of this study provide valuable reference to local engineers, designers and professionals for efficient BIPV façade applications.

PUBLICATIONS ARISING FROM THE STUDIES

Yang, H and Fung, Y., 2005. Building-integrated photovoltaics: its' past, present and future applications in Hong Kong, *Proceedings of 15th International Photovoltaic Science and Engineering Conference*, Shanghai, China, 10-15 October 2005.

Fung, Tady Y. Y. and Yang, H. X., 2005. Study on optimum inclination angle of solar collecting surface in Hong Kong, *Transactions Hong Kong Institution of Engineers, Vol. 12, No. 1*, pp. 44-48.

Fung, Tady Y. Y. and Yang, Hongxing, 2004. Thermal Performance of Semi-Transparent Type BIPV Modules, *Proceeding of the World Renewable Energy Congress VIII*, Denver, Colorado, USA, 29 August – 3 September 2004.

Yang, H. X. and Fung, Y. Y., 2003. Energy Performance Simulation and Experiments of Different BIPV Facades, *Proceeding of the 6th International Conference on Advances in Power System Control, Operation and Management*, Hong Kong, 11-14 November 2003.

Yang, H. X. and Fung, Y. Y., 2003. Building-integrated photovoltaic application –Its practice in Hong Kong, *Proceeding of the 3rd World Conference on Photovoltaic Energy Conversion*, Osaka, Japan, 11-17 May 2003.

Fung, Tady Y. Y. and Yang, H., 2005. Energy performance of Semi-transparent-type BIPV glazing *(Submitted to Energy and Buildings)*

ACKNOWLEDGEMENTS

I would like to express my sincere gratitude to my chief supervisor, Dr. Yang Hongxing, for his valuable and constructive suggestions during this research project. He has also given me patient guidance and encouragement throughout my work.

I would like to thank all the members in the Renewable Energy Research Group for their help and advice in my work, in particular Lu Lin, Lou Gang, Zhou Wei, Li Yutong and Cui Ping. Special thanks are also due to the technical staff in the laboratory of the Department of Building Services Engineering for their technical assistant in my experiment. I am also grateful to Dr. Stephen Evans and Dr. Gail Forey for their advice on my English writing.

Last but not least, I would like to give my deep gratitude to my family, especially my parents. Without their patient support and endless love, completion of this thesis would not have been possible.

TABLE OF CONTENTS

LIST OF FIGURES

LIST OF TABLES

CHAPTER 1

INTRODUCTION

Nowadays, energy supply is essential for mankind. Most of the activities in the current industrial age require the supply of electrical power. The two most prevailing kinds of primary energy resources are oil and coal. According to a recent world energy statistics (BP, 2005), in 2004, oil and coal constitute more than 60% of the world's energy supply among various energy sources. However, the use of the oil and coal causes serious adverse environmental problems, such as air pollution, acid rain and climate change due to the emissions of green house gases from fossil fuel combustion. In addition to environmental threats, the limited reserves of ordinary energy sources in the world have also been widely concerned. It is anticipated that, at current consumption rates, the supply of coal will last for around 200 years and oil for approximately 40 years (Boyle, 2004). The shortage of fossil fuels will happen in the foreseeable future. Owing to the negative effects and the finite supply of fossil fuels, the development of new sources of energy that is sustainable and environmental friendly, such as renewable energy, is necessary. Among the various types of renewable energy, solar photovoltaic is one of the popular and well-developed options.

1.1 DEVELOPMENT OF BUILDING INTEGATED PHOTOVOLTAIC (BIPV)

Photovoltaic (PV) technology has received serious concern since the 1970s. Building Integrated Photovoltaic (BIPV) is a common application of photovoltaic technology. Early projects integrated PV into residential houses. In the late 1970s and early 1980s, much effort has been paid on PV integration in commercial developments (Strong, 1996). As scientists and political have continued to look at alternative energy and conservation as solution of pollution and global climate change, BIPV applications have developed rapidly worldwide in the past two decades. A number of BIPV systems have been installed in many countries over the period (Strong, 1996; Pearsall and Wilshaw, 1996; Schoen, 2001; Bhargava, 2001; Yoo, and Lee, 2002; Yang and Fung, 2005). In recent years, BIPV technology has developed widely because of its characteristic which combines energy production with other functional features on building facade. PV modules integrated into the building envelop can reduce the overall cost by forming part of the façade and replacing traditional building elements. Sunshade and PV claddings are typical applications of the BIPV systems to achieve an aesthetically pleasing outlook and energy efficient in buildings.

In addition to sunshade and PV claddings, architects and building engineers have tended to use semi-transparent BIPV modules to replace the traditional glazing in recent years for energy efficiency and aesthetic consideration. Electricity can be produced by the solar cells in the modules and at the same time, solar heat gain is reduced due to the blocking of solar radiation by the solar cells. Increasing the solar

cell area in the semi-transparent BIPV modules can result more electric power and reduce more solar heat gain. However, daylight utilization can be reduced due to the shading of the solar cells. Therefore, a balance should be made between daylight utilization, solar heat gain and power generation from the solar cells. To date, detailed study on heat transfer due to solar radiation on the newly developed semi-transparent BIPV modules is not available. Most previous studies on energy performance of building envelop concentrated on the traditional transparent glass window. However, the applications of the semi-transparent BIPV modules have increased gradually because of its energy efficient features, and thus more attention should be paid on the energy performance of the modules.

1.2 OBJECTIVES OF THE RESEARCH

The use of semi-transparent BIPV modules is popular in BIPV systems. However, few studies have examined the impacts on energy performance of the semi-transparent modules. It is necessary to investigate the energy performance of the semi-transparent BIPV modules in detail.

The main objective of this research is to develop a method to assess the thermal performance of the semi-transparent BIPV modules, in particular the heat gain through the PV modules. The evaluation of the overall energy performance of the semi-transparent BIPV modules is another objective to be achieved in this study. The overall energy performance can be evaluated in various aspects including the amount

of heat gain through the module, the indoor illuminance level and the power generated by the module. The specific objectives of the current research are as follows:

- To develop a method for calculating the amount of heat gain through the semi-transparent BIPV module;
- to assess the level of daylight utilization of the semi-transparent BIPV modules;
- to develop a power generation model for both opaque and semi-transparent BIPV modules for local applications;
- to investigate into the overall energy performance by combining the three effects above by case studies;
- to study the effects of different parameters of the semi-transparent BIPV modules such as solar cell area, glass thickness, efficiency of the solar cells and orientations on the energy performance.

1.3 ORGANIZATION OF THE THESIS

This thesis is organized into 10 chapters. The current chapter is an introductory chapter which introduces background information related to the topic, and outlines the content of this thesis. The objectives of the thesis are established in this chapter and justified with reference to relevant studies in the area.

Chapter 2 summarizes the general information on BIPV systems. In addition, the potential of BIPV applications and the current status of BIPV applications in Hong Kong are presented. Literature review of the thermal and energy performance of

window glass and PV glazing are given in this chapter.

Chapter 3 outlines the methodologies of the current research in order to achieve the objectives. It illustrates how to formulate the simulation models for evaluating the heat gains, PV power generation and indoor daylight level. The experimental methods for the validation of the models are also presented in this chapter.

Chapter 4 analyzes the solar radiation densities on an inclined surface. Different solar radiation models are compared and the optimum orientation and inclination of the surface are proposed with reference to the theoretical and experimental study. The results of this chapter provide the foundation of the models developed in the following chapters.

Chapter 5 describes the development of a novel heat gain simulation model, the SPVHG model, which is the main contribution to this thesis. The heat transfer mechanisms within the elements of the semi-transparent BIPV module are analyzed so that the corresponding energy equations are established. The optical properties of the glass layer, and the heat exchange between the module and the ambient environment are considered in the model. The model is able to predict the heat gain of the PV modules that have different parameters and under various orientations and solar incident angles.

Chapter 6 presents the power generation models of the BIPV systems. An existing power generation model of PV claddings is described. An on-site measurement on a local BIPV system has been carried out. The measurement results are analyzed and the existing power generation model is modified according to the measurement results so that the model suits the local conditions. Another power generation model for the semi-transparent BIPV module is also described in this

chapter. All the power generation models calculate the amount of power produced by the PV modules. They are used in the assessment of the total energy performance of the PV façade described in Chapter 8.

Chapter 7 describes a theoretical method for evaluating the indoor daylight level under different window areas and different solar cell areas of the semi-transparent modules. The indoor daylight illuminance level and the power consumption of the artificial lighting can be determined by this method. This method is also used in the assessment of the total energy performance of the PV façade.

Chapter 8 reports the experimental study on the heat gain of semi-transparent BIPV modules. The aim of the experimental study is to validate the SPVHG model developed in Chapter 4. The experimental procedure and results are presented in detail in this chapter.

Chapter 9 presents the simulation results of the SPVHG model. Different module's parameter such as the solar cell area ratio, the efficiency of the solar cell, the module thickness and its orientation are studied for their impacts on the annual heat gain. A separate simulation study which considers the thermal performance, the power production and the daylight utilization of the PV module is described in this chapter. Therefore, the net electricity benefit of the PV façade can be determined.

Chapter 10 concludes the results of the simulation and experimental studies of the thermal performance of the semi-transparent BIPV modules, and summarizes the energy performance of different arrangements of PV modules on a PV façade. Recommendations for future research are also suggested in this chapter.

CHAPTER 2

LITERATURE REVIEW

A successful BIPV solution requires interaction between building design and PV system design. Various approaches to installing PV arrays in buildings have been developed. This chapter provides an overview of the integration types of the BIPV system in different building parts such as flat roofs and vertical facades, as well as glazed roof and sunshade devices. The components of BIPV systems are also introduced in this chapter.

Before planning the installation of a BIPV system, it is vital to understand the feasibility of adopting this technology for the local situation. A critical assessment of the potential application of the BIPV systems in Hong Kong in terms of solar radiation, area and cost considerations are provided in this chapter.

Although Hong Kong is not playing the leading role in BIPV market, a number of BIPV projects have been completed in the past decade. The developers of these projects include local institutions, the government and private developers. This chapter gives an overview of the status of BIPV development in Hong Kong, and highlights some significant projects in detail.

A literature review is also presented in this chapter. The literature review focuses on modeling of heat transfer through glass, as well as the methods of assessing the energy performance of PV facades including semi-transparent BIPV glazing.

2.1 OVERVIEW OF BIPV SYSTEMS

BIPV systems have been well-developed all over the world among the other types of PV applications. This is because the BIPV systems require no additional land and they can provide electricity near the point of use. In the past decade, a number of new buildings have been integrated with BIPV systems as an alternative power source. The following section will give a brief overview on the type and components of the BIPV system that are commonly found in current applications.

2.1.1 Integrating approach

All parts of the surface of the building are suitable for installing photovoltaic arrays, provided that the surface can receive adequate amount of solar radiation. The installation methods of the photovoltaic arrays can be categorized into three main types according to their approaches of integration, namely, roof-mounted systems, sunshades systems and façade systems. The characteristics of each type of the system are described separately in the following three paragraphs.

(i) *Roof-mounted systems*

PV modules in this kind of system are installed on the roof of the buildings. The PV modules can be either installed as an independent array on the rooftop or combined with the roof structural system. The slope and orientation of the independent module array can be selected so that the most solar radiation can be captured. This arrangement can avoid a substantial amount of heat gain due to

sunshine on the building roof. However, water proofing issues have to be considered. For PV modules that are integrated to the roof structure, typical application can be found on the top of an atrium. Semi-transparent PV modules are used together with clear glazing in this case for providing daylight to the indoors. Not surprisingly, the roof-mounted BIPV system is the most prevalent one among the other types of integration because it receives more solar energy for low-latitude areas and PV modules installed on the roof are less likely to be shaded by other obstacles. Also, this system will bring less impact to the appearance of the building. However, special attention should be paid to the structural and weather-proofing issues.

Figure 2.1 Roof top PV arrays on the EMSD Headquarter of HK

Figure 2.2 PV skylight in an university in the UK

(ii) *Sunshading systems*

PV modules can be installed as awnings outside the windows to shade direct sunlight. As a result, the system can provide energy benefits not only though the electricity generation by the PV modules but also through the reduction of solar heat gain to the building. The inclination of the PV modules can also be designed to maximize energy production. However, compromise should be made with the

aesthetic consideration because the PV modules can be easily seen from the outside of the building. The sunshaded systems also incur higher installation cost among the others because of the addition structural requirement. Figure 2.3 shows a photo of a sunshading BIPV system.

Figure 2.3 A sunshading BIPV system

(iii) Façade systems

In these kinds of systems, PV modules act as a part of the outer skin of the building. The PV modules used in the systems can be either opaque or semi-transparent. Therefore, these kinds of systems can be further divided into two sub-categories; they are PV cladding and semi-transparent PV glazing, which are shown in Figure 2.4 and 2.5 respectively.

Mounting a series of opaque PV modules on building façade can form a PV cladding. The modules are usually mounted on cladding rails in order to provide a ventilation gap between the building structure and the PV modules. The gap has the beneficial effect of reducing the temperature of the modules, thus increasing power converting efficiency.

In the case of a semi-transparent PV module, opaque solar cells are encapsulated in between two glass sheets to form a “glass-solar cells-glass” structure. This kind of PV module can be used in window systems to admit daylight as well as produce electricity. Further, the PV modules can be incorporated into double-glazed curtain wall systems by using the modules as the outer pane of the system. The area of the

space between the solar cells can be selected by balancing the daylight requirement and the electricity yield. This kind of integration is highly cost effective because the PV modules can replace the traditional glass on the building façades to reduce the installation cost.

It is necessary to mention that a kind of “see-through” thin film solar cell has been invented as semi-transparent BIPV module. The structure of the solar cell is the same as the ordinary thin film solar cells but with microscopic holes to make the cell semi-transparent. However, the electricity conversion efficiency of the thin film type solar cells (e.g. amorphous silicon) is usually low (around 5% - 8%) (Sonnenenergie, 2005), they are therefore not being considered in this study.

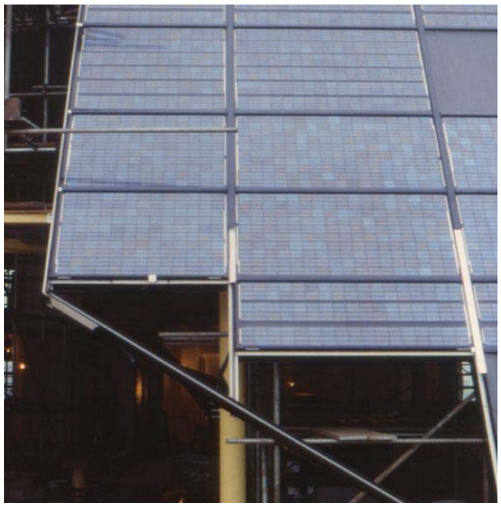

Figure 2.4 A PV cladding under construction

Figure 2.5 A semi-transparent BIPV façade

2.1.2 System components

The previous section mentioned the integration of PV modules. Other than the PV modules, there are other components in a BIPV system. In general, a BIPV system

includes the following components:

- Photovoltaic modules;
- Power conditioning and control equipment;
- Energy storage equipment (Batteries);
- Back-up generator.

The above components may not necessarily appear in all kinds of BIPV systems. The need for each component depends on the application and related statuary requirements. Generally speaking, there are two categories of BIPV systems distinguished by their connections, namely the stand-alone and the grid-connected system. In a stand-alone system, the power generated by PV arrays will be stored in a group of batteries. The batteries are charged during sunshine and discharged in nighttime or cloudy days. This kind of system is isolated from utility system so its operation and maintenance is relatively simple, but more space is needed for the accommodation of the batteries and it is more expensive. In contrast, a grid-connected system treats the grid source as both storage element and back-up generator. The flexibility and reliability is higher than stand-alone system. However, technical and administrative issues have to be resolved with the power company prior to assessing the utility grid. The schematic diagrams of stand-alone and grid-connected system are illustrated in Figure 2.6 and 2.7 respectively.

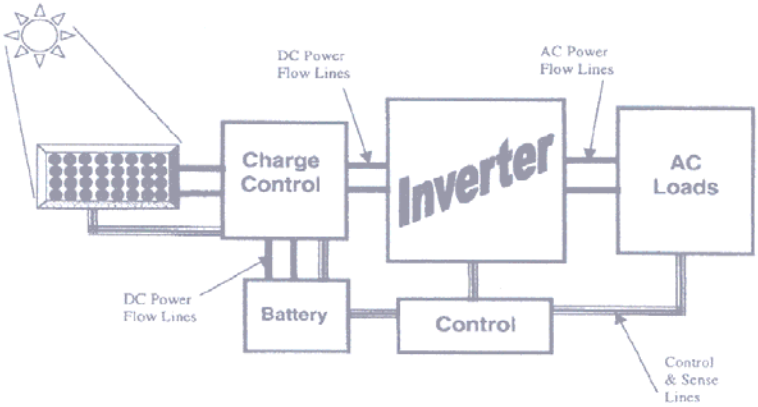

Figure 2.6 A schematic diagram of a stand-alone system

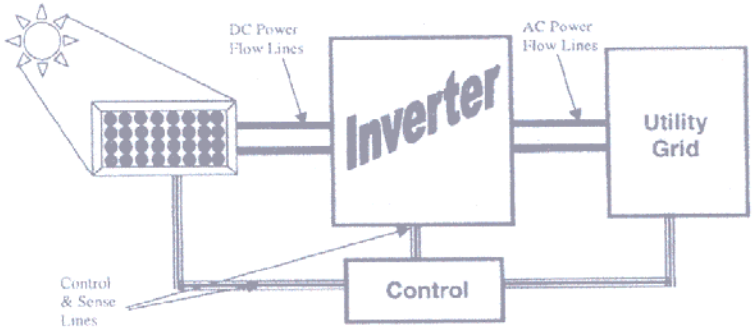

Figure 2.7 A schematic diagram of a grid-connected system

Figure 2.8 shows the worldwide cumulative installed power capacity for different connections of PV systems. As shown in the figure, the installed power capacity increased by more than 23 times from 1992 to 2003 (110 MW in 1992 to 2596 MW in 2004). The grid-connected applications showed a continuously increasing trend in the past decade. From 1999 onward, the installed power of grid-connected systems has exceeded that of stand-alone systems and took up more than 80% of the total power capacity in 2004. This reveals that grid-connected PV systems are the prevalent option in the global PV applications market.

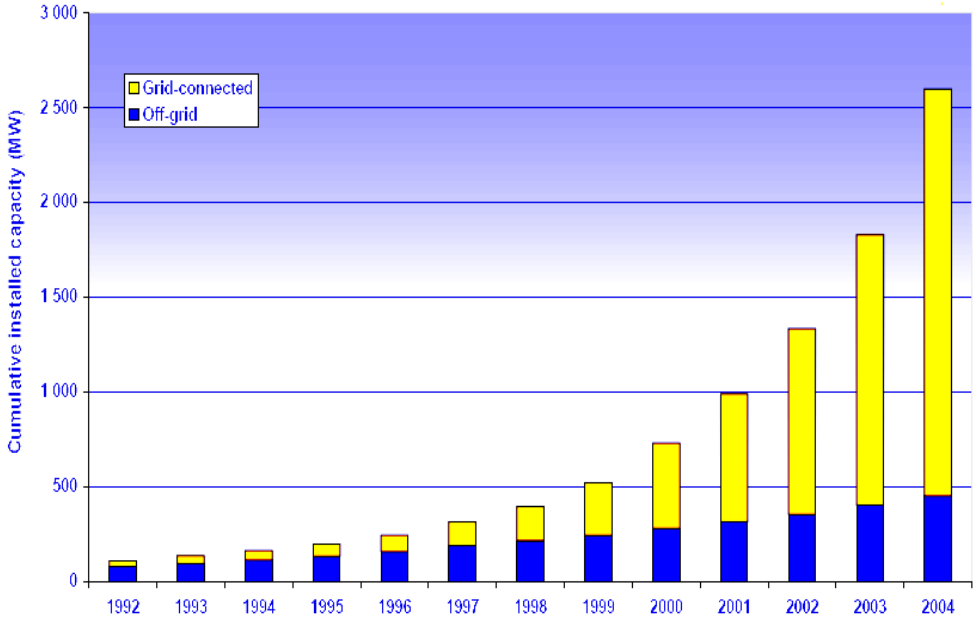

Figure 2.8 Cumulative installed PV power capacity
(source: IEA-PVPS website*)

*: The data from the source only includes the countries participated in the survey conducted by the IEA-PVPS. There are totally 20 countries participated in the survey, which includes the countries that have high PV applications such as Japan, Germany, USA etc. Please refer to IEA-PVPS website for details.

2.2 BIPV APPLICATIONS IN HONG KONG

2.2.1 Potential of BIPV applications in Hong Kong

Burning of fossil fuels results in detrimental effects to the environment. As a city that mainly relies on fossil fuels as the dominant source of energy production, Hong Kong's air quality is deteriorated significantly in recent years. In consequence, the energy efficiency and environmental protection issues have become more prominent in Hong Kong. More and more efforts have been paid on the development of renewable energy such as BIPV applications.

The effectiveness of deployment of BIPV depends on technical and administrative factors. Before any administrative issues are considered, technical feasibility is a pre-requisite of BIPV applications and has to be evaluated in advance. From the perspective of technical aspect, the availability of both solar radiation and area for mounting PV modules are the crucial factors to be considered. This section explores the potential of BIPV applications in Hong Kong in terms of the solar radiation and area availability. In addition to technical issues, cost considerations for the Hong Kong situation are also briefly discussed in this section.

2.2.1.1 Available solar radiation in Hong Kong

In Hong Kong, the mean daily global solar radiation on horizontal surface is found to be 14.46 MJ/m^2. This value was obtained according to the meteorological data recorded by the Hong Kong Observatory from 1961 to 1990. The value is higher than that of other countries or cities such as Japan, Germany, some sites in the United

States and London (Lu, 2004). Therefore, compared with other countries, the solar radiation resource in Hong Kong is fairly abundant.

Figure 2.9 shows the monthly profile of solar radiation in 1989, which has been found to be the most representative weather records in Hong Kong (Wong and Ngan, 1993). As shown in the figure, the largest amount of solar radiation appears in the summer (from June to August), while the spring has the least solar radiation (from March to May) in Hong Kong. The annual total solar radiation is more than 4700 MJ/m^2. If this amount of solar radiation is converted to electricity by PV technology, it is expected to generate a total of 141.8 kWh/year per m^2 of PV panel, provided that the PV panels are oriented horizontally and the PV system efficiency is 10.8% (Electrical and Mechanical Services Department, HKSAR, 2002). If all the lands in Hong Kong were filled with horizontal PV panels, nearly 155,700 GWh of electricity could be produced per year, which is about 4 times of the electricity demand in 2003 (38,454 GWh). It can therefore be concluded that Hong Kong has abundant resource of solar radiation.

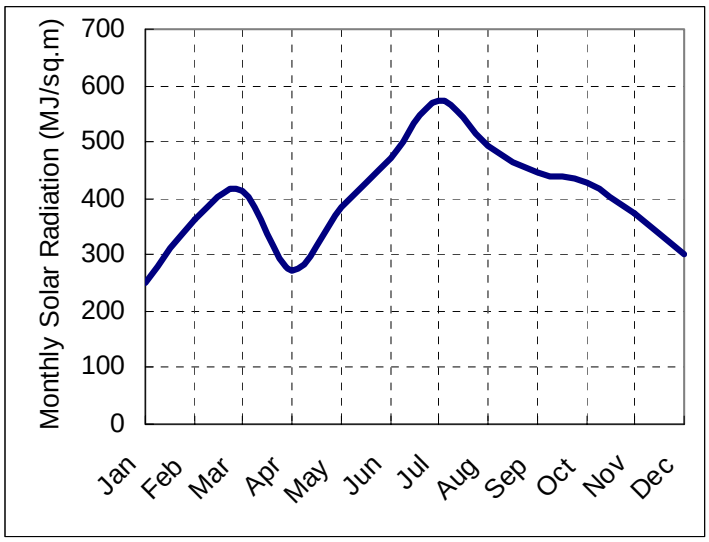

Figure 2.9 Annual Solar Radiation profile in Hong Kong

2.2.1.2 Available area in Hong Kong for BIPV applications

The available electricity will be much smaller for actual situation due to the constraints of land use. A term "equivalent horizontal area" was introduced to estimate the potential energy yielded from BIPV technology by the Electrical and Mechanical Services Department, HKSAR. However, BIPV modules, especially semi-transparent type modules, are usually integrated vertically into the building facades rather than placed horizontally, so it is more practical to estimate the energy output from the vertical facades. The potential energy yielded for different vertical orientations are estimated and compared in Table 2.1. The values of potential energy yielded shown in Table 2.1 are calculated by the following equation,

$$P_{pv}(\theta) = G_{total}(\theta) \cdot \eta \cdot A_{equiv} \tag{2.1}$$

where η is the PV system efficiency and A_{equiv} is the equivalent horizontal area, $G_{total}(\theta)$ is the annual total solar radiation received on a surface with inclination of θ degree, which can be obtained according to a separated model. The details of the model are discussed in Chapter 3.

According to Table 2.1, if all available equivalent horizontal areas were installed with PV modules, the potential power generation is 6,324 GWh. This is equivalent to about 16.4% of the electricity consumption in 2003. Instead of the horizontal position, assuming the PV modules were installed vertically on building facades of different orientations, the south-east façade could produce the largest amount of electricity.

Hong Kong has a very good potential of BIPV applications in terms of available area because there are many high rise buildings in Hong Kong. In addition to the deployment opportunity in future developments, many existing buildings may also provide opportunities for retrofitting BIPV system to capture solar energy.

Table 2.1 Potential power generation from BIPV systems in Hong Kong

Building type	Area (km^2)	Assumed Ratio of Equivalent Horizontal area for PV coverage	Equivalent Horizontal Area (km^2)	Potential Power Generation of different surfaces (GWh)					
				Horizontal	**East**	**South-East**	**South**	**South-West**	**West**
1. Residential	45	30%	13.5	1,914	1,088	1,211	1,153	1,069	930
2. Public rental housing	14	30%	4.2	596	338	377	359	333	289
3. Commercial	2	50%	1	142	81	90	85	79	69
4. Industrial	11	50%	5.5	780	443	493	470	435	379
5. Government, institution and community facilities	21	20%	4.2	596	338	377	359	333	289
6. Temporary housing areas	1	0%	0	0	0	0	0	0	0
7. Vacant development land	27	60%	16.2	2,297	1,305	1,453	1,383	1,283	1,116
			Total:	***6,324***	***3,594***	***4,000***	***3,809***	***3,531***	***3,073***

2.2.1.3 Cost considerations

Cost is always the greatest hindrance in the application of BIPV systems. The unacceptable payback period and the comparatively higher average tariff rate of PV electricity generation discourage the use of the technology (HKD$2.2 to HKD$4.1 per kWh for PV electricity generation while conventional power rates at around HKD$0.9 per kWh in 2002 (Electrical and Mechanical Services Department, HKSAR, 2002)). The high generation cost is due to the high cost of PV panels. However, the price of PV panels has declined in recent years. The trend will continue falling due to the rapid growth rate of PV panels production. The cost of PV electricity generation is expected to become much more competitive compared with the traditional energy sources in the near future.

Installation of BIPV modules also takes a substantial portion of the total cost. The use of the Semi-transparent PV module (on which this thesis is focused) is highly cost effective since it can replace the ordinary window glass or act as an alternative curtain wall material to cover part of the installation cost. According to the quotation from contractors, the cost of different cladding materials are: aluminium cladding at HKD$2,000/m^2, stone cladding at HKD$9,000/m^2 and PV panels at HKD$6,000/m^2 in 2002 (Electrical and Mechanical Services Department, HKSAR, 2002). The cost of PV installation and the energy efficiency are expected to improve in the future. With rapid development of BIPV technology and design, the growing potential of BIPV is favorable.

By studying the potential of BIPV applications in terms of cost consideration, availability of solar radiation and area, it is found that Hong Kong is technically favorable for BIPV applications. If more administrative support can be provided by

the Government and power companies, the development of BIPV in Hong Kong will be faster for a more sustainable environment.

2.2.2 The status of BIPV development in Hong Kong

Awareness of developing renewable energy applications in Hong Kong has been increasing in recent years. The HKSAR Government has started to promote the use of renewable energy by conducting feasibility studies and implementing pilot projects. Between 2000 and 2004, the Electrical and Mechanical Services Department (EMSD) of the HKSAR commissioned a feasibility study of renewable energy applications in Hong Kong. As revealed by the study, most of the PV applications in Hong Kong are related to BIPV systems. A number of BIPV projects implemented by the Government, local tertiary education institutions and major developers were completed in the past few years. Up to the first quarter of 2005, more than 740 kW of BIPV power have been installed in Hong Kong (Yang and Fung, 2003; EMSD, 2002 and 2005; Lo, 2005). More BIPV projects are under-construction or in the planning stage. Although the projects in Hong Kong only vary from small to medium scale compared with those in foreign countries, the growing trend is rather important. In the following section, some examples of BIPV projects in Hong Kong will be reviewed. As the current study mainly focuses on the semi-transparent PV modules, the review will concentrate on the projects incorporated with this kind of module.

2.2.2.1 Examples of BIPV projects incorporated with semi-transparent PV module

The use of semi-transparent PV modules is commonly found in the BIPV projects in Hong Kong. The Headquarter of the Electrical and Mechanical Services Department of the HKSAR Government is one of the examples. Up to 2005, this project has the largest installed capacity of the PV development in Hong Kong. The total rated power capacity of the system is 350 kW, which comprises both BIPV glazing and roof-mounted array. For the BIPV glazing system, 20 pieces of 1680 x 1902 mm semi-transparent PV modules were integrated into the glazing roof cover of the viewing gallery of the building, which contributes 3 kW to the total rated power of the whole PV system. Figure 2.11 shows a picture of the BIPV glazing system in the EMSD headquarter.

The BIPV system in Wan Chai Tower is another government BIPV project installed with semi-transparent PV modules. This is a retrofit project which involves the replacement of some of the existing building structures with the PV panels. A total of 96m^2 of semi-transparent PV modules are integrated vertically to replace some of the glass-infill of the existing glass atrium at the front entrance hall of the building. This arrangement can provide skylight to the entrance hall as well as generate power. Another 232m^2 semi-transparent PV modules are mounted externally on the building façade to provide shading for the upper portion of all south-facing windows on the 1st to 12th floor. Figure 2.12 shows a photo of the BIPV shading. This project is a pilot project implemented by the HKSAR in 2002 to demonstrate to the general public the potential applications of PV technology in buildings.

A number of BIPV projects with semi-transparent PV modules in Hong Kong of

different scales are in service. Some of their photos are shown in Figure 2.10 to Figure 2.13. Table 2.2 summarizes the major BIPV projects in Hong Kong. Due to the versatility of function and integrating format of the modules, semi-transparent PV modules will play an important role in BIPV development. It is anticipated that this kind of module will become a prevailing architectural feature in modern buildings. The energy performance of the module should be investigated in order to have a comprehensive knowledge in the impact of this kind of PV module on the building energy use.

Similar to ordinary windows, semi-transparent BIPV modules act as a thermal barrier against outdoors environment. Studying the heat gain through the modules is a good starting point for assessing its energy performance. Reviews of research studies related to heat transfer through glass are presented in the next section.

Figure 2.10 Semi-transparent BIPV modules have been installed on the roof the Hong Kong's new landmark – One Peking

Figure 2.11 The BIPV skylight system in EMSD Headquater

Figure 2.12 Sunshade BIPV modules in Wan Chai Tower

Figure 2.13 BIPV modules on the façade of an office building in Science Park

Table 2.2 Major BIPV projects in Hong Kong

Year of installation	Project	Power capacity	Type of integration
1999	The H.K. Polytechnic University	8 kW	Roof and wall integrated
2001	C.Y.C. building in the H.K. University	4.3 kW	Vertical façade
2002	Kadoorie Farm reception building	4 kW	Roof array
2002	Wai Chai Tower	55 kW	Vertical façade with semi-transparent modules, roof integrated
2003	No. 1 Peking Road	7.2 kW	Semi-transparent modules integrated into curtain wall
2003	Ma Wan Primary School	40 kW	Roof integrated array and semi-transparent modules, wall integrated
2004	Penny Bay fire station	80 kW	Roof integrated semi-transparent modules
2002 - 2004	Hong Kong Science Park	198 kW	Semi-transparent modules as vertical façade, sunshaded type modules, roof integrated modules
2005	EMSD Headquarter	350 kW	Roof integrated array and semi-transparent modules

2.3 REVIEW OF PAST STUDIES

The preceding section has outlined the overview of the BIPV system and the development of the semi-transparent BIPV projects in Hong Kong. This section concentrates on reviewing the past research regarding heat transfer and energy performance studies of window glass, semi-transparent BIPV modules and PV façades.

2.3.1 Methods of modeling heat transfer through glass

Research on the heat transfer through ordinary glazing has been undertaken for over a half century. As little research regarding the semi-transparent PV glazing has been conducted, the knowledge of heat transfer through ordinary glazing is a good reference for developing a methodology on modeling the heat transfer through semi-transparent PV glazing.

The heat gain through a glass sheet can be evaluated by steady state method and transient state method. Due to the differences in calculation approach and assumption made for the both methods, the accuracy and the time for computing are different. The steady state method is usually less accurate but consumes a shorter computing time, while the converse applies for the transient state method. Using the transient state method may cause unacceptable computing time in some cases. For most of the applications in building energy simulation, the steady state method is accurate enough as well as providing acceptable computing time. However in some scenarios such as changing ambient environment and complicated structure of the glass, the transient state method is necessary to tackle the situation.

The steady state method is widely used in building energy simulation. Its principle can be found in various textbooks and reference books (Threlkeld, 1970; Jones, 2001; ASHRAE, 2001). Basically, the modes of heat transfer through a piece of glass include: (a) reflection, absorption and transmission of direct and diffuse solar radiation; (b) convection and radiation of absorbed solar radiation; (c) conduction and convection due to indoor-outdoor temperature difference. The first two components are affected by the amount of solar radiation, and they can be represented by the term

solar heat gain coefficient (*SHGC*), which combines the transmitted solar radiation and the inward-flowing fraction of the absorbed solar radiation as follows,

$$SHGC = \tau + N_i \alpha \tag{2.2}$$

where τ and α are the solar transmittance and solar absorptance of the glass respectively. N_i is the inward-flowing fraction of the absorbed radiation, which can be affected by many parameters such as inside and outside convective coefficient, glass overall heat transfer coefficient, zone geometry and zone radiation properties. However, for simplification, N_i can be expressed in terms of inside (h_i) and outside (h_o) convective coefficient for simple glass as follows,

$$N_i = \frac{h_i}{h_o + h_i} \tag{2.3}$$

SHGC represents the fraction of heat gain to the indoors due to solar radiation. It relates to the optical properties of the glass as shown in equation (2.2). The optical properties of the glass varies with the incident angle of the solar radiation. Many studies regarding this issue have been conducted by various experts. Gueymard (1989) proposed a simplified model for computing the transmitted energy through windows at different incident angles based on the Fresnel and Stokes equations. The model is applicable to window up to four layers. Karlsson and Roos (2000) presented a method to model the angular dependence of the solar energy transmission through coated glass. In their model, the type of coating was categorized by the authors so that the detailed information about the coating composition was not needed.

Heat gain due to solar radiation (or solar heat gain, Q_{sol}) can be obtained when the *SHGC* is multiplied by the solar radiation striking on the glass surface (S_t), that is,

$$Q_{sol} = (\tau + N_i \alpha) \cdot S_t \tag{2.4}$$

The heat gain due to solar radiation has also been investigated in detail by Rubin (1982). He introduced a detailed procedure for modeling the net radiative heat flux between glass surfaces. Therefore the optical properties of the glass can be found accordingly. The procedure from Rubin was used in the computer program WINDOW which was developed by the Lawrence Berkeley Laboratory, USA. Arasteh et al. (1989) modified Rubin's model by considering the centre-of-glass area, edge-of-glass area and frame area for a complete fenestration system.

The heat gain due to the temperature difference between indoors and outdoors can be determined by multiplying the overall heat transfer coefficient (U_o) of the glass to the indoor-outdoor temperature difference ($T_{out} - T_{in}$):

$$Q_T = U_o \cdot (T_{out} - T_{in}) \tag{2.5}$$

where U_o can be evaluated using the thermal conductivity of the glass, the indoor and outdoor convective heat transfer coefficients . It can be expressed as,

$$U_o^{-1} = \frac{1}{1/h_o + 1/h_i + d/k} \tag{2.6}$$

where d and k are the thickness and the thermal conductivity of the glass respectively. Combining equations (2.4) and (2.5) can yield the total heat gain through the glass.

If the glass is subjected to a sudden change in environment, an unsteady state method can be used to model the heat transfer process. The heat transfer across the glass thickness can be represented by a general heat conduction equation as follows, assuming three-dimensional situation is considered,

$$\frac{\partial T}{\partial t} = \lambda_g \left(\frac{\partial^2 T}{\partial x^2} + \frac{\partial^2 T}{\partial y^2} + \frac{\partial^2 T}{\partial z^2} \right) \tag{2.7}$$

where T is the glass temperature at time t. λ_g is the thermal diffusivity of the glass. x, y and z denote the three directions of the heat transfer process within the glass. The boundary conditions of equation (2.7) can be represented by the convective and radiative heat transfer equations of the heat exchange between the glass surfaces and the ambient environment.

Various researchers have investigated the thermal performance of window glass using transient state method. Ismail and Henriquez (2003) modeled the heat transfer across a simple glass window of different thickness with two-dimensional transient equations. Various solar heat gain indices such as solar heat gain coefficient and shading coefficient were evaluated using the model. Two-dimensional heat transfer analysis has also been adopted by Curcija and Goss (1994) and Wright and Sullivan (1995). They focused on the heat transfer through insulated glazing unit with gas filling cavity. Alvarez et al. (1998) studied the thermal effects of chemically deposited solar control coating on a laminated glazing using one-dimensional transient state model. Ismail and Henriquez (1998) presented a one-dimensional thermal model for the double-sealed glass filled with phase changing material (PCM). Both the models of Alvarez and Ismail were solved by finite difference method.

When comparing the steady state method and the transient state method, it can be seen that steady state method offers a simplified approach which facilitates a shorter computing time, while transient state method gives a detailed simulation so that the temperature distribution across the glass thickness can be calculated. The choice of using different approaches should be determined by the actual situation of the

problem.

2.3.2 Energy performance of PV façade

As the BIPV technology is becoming mature, an increasing number of applications can be found worldwide. BIPV modules are integrated onto the outer skin of a building. In order to reduce the module's temperature and improves the energy performance of the PV modules, an air gap can be designed behind the module to allow natural ventilation between the modules and the building walls (Brinkworth et al., 1997). Therefore, more consideration is needed in evaluating the heat transfer through the PV façade.

A considerable number of studies on the heat transfer and energy performance of the PV façade have been carried out. Brinkworth et al. (1997) validated that PV module temperature and heat gain into the building can be significantly reduced by a ventilated air gap behind the PV module. Similar studies on the heat transfer characteristics of ventilated PV facade have also been conducted by various specialists (Moshfegh and Sandberg, 1998; Brinkworth et al., 2000; Yang et al., 2000; Infield et al., 2004).

Another comprehensive study on thermal characteristics of PV façade was conducted by Jones and Underwood (2001). They established a model of PV module temperature by differential equations. Convective and radiative heat exchange between the PV module and the ambient as well as the solar irradiance input to the module were considered in the model. The authors also included the PV modules' electrical power output in the equation. The model was a non-steady state equation of

the module's temperature and was solved numerically by Euler method.

Other than the heat transfer characteristics, the optimum area of PV module on a solar façade has also been investigated. According to Vartiainen (2000), a solar façade was defined as a façade which was composed of clear or diffusive glazing, semi-transparent PV glazing and opaque area covered by PV modules. Vartiainen has developed a detailed daylight simulation program to predict the daylight availability of different layouts of the solar façade. For various solar façade patterns, he predicted the electricity benefits of the solar façade by taking into account the energy output from the PV modules and the energy saving due to daylight utilization. However, Vartiainen's study mainly focused on the daylight simulation, the analysis on PV element was relatively simple, and only the optimum window area was presented.

2.3.3 Energy performance of semi-transparent PV modules

Other than considering a PV façade, the heat transfer across an individual opaque PV module was also studied by various experts. Krauter and Hanitsch (1996) considered the optical performance (inter-reflection) of various layers of material in a PV module in addition to the heat transfer mechanism. They established a relationship between the heat dissipation and efficiency of PV module. Zhu et al. (2002) presented a numerical analysis of heat transfer in a opaque PV module. Two-dimensional transient equations were established for describing the heat transfer process in different layers within the PV module. The effects of thermal storage as well as the optical energy absorption were considered in their model.

To date, only a limited amount of research has been conducted for the energy

performance of semi-transparent PV modules. The most representative work on this issue was carried out by Boer and Helden (2001). They modeled the cooling and heating demand as well as the daylight distribution inside an office room which incorporated with semi-transparent PV module in Madrid. The authors first generated the optical and thermal properties of the PV modules of different solar cell area ratios by the software program WINDOW 4.1. They evaluated the refraction and transmission of the module by taking the area weighted average of the whole surface. The data was then input to the transient simulation software, TRNSYS, as part of the building element properties to perform hourly building energy simulation. However, the heat gain through window glass is calculated by steady-state models in the TRNSYS.

Another study on semi-transparent PV module was carried out by Miyazaki et al. (2005). The study concentrated on the “see-through” type film solar cells which transparent characteristic is formed by microscopic holes within the cells. The authors investigated the effects of the module transmittance on daylight utilization, electricity production, heating load and cooling load of an office building. They also used the program WINDOW and another energy simulation program package for the simulation work. In their study, the optical properties of different layers of the PV module were treated separately in different ways. The transmittance and reflectance of the cover and back glass were retrieved from the glass library of WINDOW, while the optical properties of the solar cell layer were co-related to the area occupied by the solar cells. The information was then input to the energy simulation program, EnergyPlus, which deploys heat balance method to model the heat gain through windows as well as the cooling load of the whole building.

2.4 SUMMARY

After studying the potential of BIPV applications in Hong Kong, it has been found that the practical electricity production by BIPV systems can provide 10% of the total demand in 2003. These significant findings encourage the deployment of PV technology as an alternative energy source.

The heat transfer of traditional glass has been investigated for many years. However, there have been limited investigations into the heat transfer characteristics of semi-transparent PV module. Although few studies on semi-transparent PV module can be found, the previous studies only use existing simulation program to evaluate the heat gain through the module. In fact the simulation programs only treat the semi-transparent PV module as ordinary clear glass because there is not such kind of glass in their database. Users have to make a series of modifications to the glass properties before input. Under this circumstance, the simulation only deals with an ordinary window glass with different optical properties rather than a glass with solar cells inside.

The modeling methods of existing simulation programs may also not be suitable for estimating the heat gain through the PV module. Most of cooling load simulation programs adopt either one of the two main approaches, referred to as weighting factor method and heat balance method for heat gain modeling. Although these two methods can accurately calculate the heat gain through ordinary glazing, they fail to take account of the effects of the solar cell layer inside the PV modules as a uniform temperature across the glass thickness is assumed. The heat absorbed by the solar cell is ignored. Since solar cells are made up of semi-conductors, their heat capacity is

much higher than that of the glass and thus affects the temperature distribution inside the PV modules.

In addition to thermal effects, impacts on daylight availability and power generation due to the use of semi-transparent BIPV module have also been overlooked. Semi-transparent BIPV modules integrated into a building can act as a power generator. Besides, solar radiation can be blocked by the solar cells within the modules to reduce solar heat gain to the building. However, the indoor daylight level will also be reduced at the same time, thus more artificial lighting is required. The amount of electricity generation, heat gain and daylight reduction are directly affected by the solar cell area in the module. Increasing the solar cell area results in more electricity power and larger heat gain reduction, but more artificial lighting power is required. The converse happens if the solar cell area is reduced. The solar cell area critically affects the energy performance of the module. To date, little research has been devoted to model the energy impacts on the building due to the use of the semi-transparent BIPV modules in detail. There is clearly a need for studying the energy performance of the semi-transparent BIPV modules.

CHAPTER 3

METHODOLOGY

This chapter describes the methodologies of the current study in achieving the project aims. The methodologies of this study involve theoretical work and experimental work. As mentioned previously, there is no accurate method for modeling the amount of heat gain of the semi-transparent BIPV modules. The theoretical studies in this thesis are to solve this issue. In addition to the heat gain modeling, the theoretical studies include the development of power generation model and indoor illuminance model for assessing the total energy performance of the BIPV façades.

The experimental work aims at examining the validity of the simulation models. The methods of the experiments and models' validation are described in this chapter.

3.1 THEORETICAL WORK

In order to evaluate the energy performance of the semi-transparent BIPV modules, a number of simulation models were developed. The simulation models were divided into three main parts: the first part is a heat gain model; the second part is a PV power generation model and the last part is a daylight level model. Prior to the

development of the above models, the solar radiation intensity on the surface of the PV modules has to be determined by using a solar radiation model because the amount of solar radiation reaches the PV module's surface is a necessary input to the three mentioned models.

Although the solar radiation on an inclined surface is essential, this information is not readily available because only horizontal irradiance values are available from the Hong Kong Observatory records. It is required to predict the amount of solar radiation on an inclined surface of different orientations. Four well-known solar radiation models are analyzed by incorporating the typical weather data of Hong Kong. The four models are then compared with the solar radiation data collected on site. As a result, the solar radiation model that best suit the Hong Kong conditions is deployed for the development of other simulation models. In addition, the optimum inclination and orientation of the any solar collecting surface for Hong Kong situations can be determined after the analysis.

With regard to the heat gain model, the Semi-transparent Photovoltaic module Heat Gain (SPVHG) model is developed to simulate the heat gain due to the semi-transparent BIPV module. In order to take into account the transient conditions and non-homogeneous elements of the PV modules, transient energy balancing equations are established for analyzing the heat conduction problems of the PV modules. The optical properties of the glass layers of the PV modules are also considered in the equations. Owing to the time depending characteristics of the equations, they are solved by a numerical method. The effects of different parameters such as solar cell area, glass thickness, solar cell efficiency and orientation are assessed using the model. The electricity consumed by the air-conditioning systems

due to the cooling load was then estimated in different scenarios.

A power generation model is established for calculating the electricity generated by the BIPV module on building façade. Both opaque and semi-transparent type BIPV modules are considered in the model. The fundamental solar cell's diode model is use as the basis of the power generation model. The diode model is then modified by incorporating the data collected from on-site measurements. Further, the model can be validated by the measured data. Regarding the power generation of the semi-transparent BIPV modules, the electrical parameters of this kind of PV modules are always absent. Therefore, the fundamental solar cell diode model is not applicable. The power generation of this kind of PV modules is evaluated by considering the solar cell efficiency, solar radiation intensity and other optical characteristics of the PV modules.

In addition to heat gain and power generation, daylight utilization has to be assessed in order to determine the total energy performance of BIPV façades. An indoor illuminance model is developed for calculating the indoor daylight level for the applications of the semi-transparent BIPV modules in building facades. Since the main theme of the current study is not to study the principle of daylight modeling in detail, existing methods for modeling indoor illuminance are investigated and modified for the applications of this study. After obtaining the indoor daylight level by using the illuminance model, the artificial lighting power and the corresponding power saving can then be estimated.

Finally, the results of the three parts were combined to obtain the overall energy performance. Typical weather data of Hong Kong recorded by the Hong Kong Observatory are used with the models to predict the year-round performance.

3.2 EXPERIMENTAL WORK

In order to examine the validity of the simulation models, a number of experiments were carried out. The experimental studies were divided into two components. The first component is the on-site measurement of BIPV electricity production, and the second is the investigation of heat gain through a semi-transparent BIPV module. The results of both components were used to verify the corresponding simulation models.

The first component of the experimental work was carried out in the BIPV system that installed on the roof of an amenities building in the campus of The Hong Kong Polytechnic University. The BIPV system comprises 98 opaque PV modules of total rated power 7.8 kW, which included: (a) PV array mounted on the east, south and west façades; (b) another inclined PV array toward south installed on the roof. The system was connected to the utility grid and provided part of the lighting power for the amenities building. The solar irradiance, module surface temperature, ambient temperature, electrical current and voltage produced by the BIPV system were recorded. The measured power output from the BIPV system and the simulated power calculated by the power generation model of each orientation are compared in order to validate the model. Figure 3.1 shows the photos of the BIPV system.

Regarding the experimental study on the heat transfer through a semi-transparent BIPV module, a test rig was set up in the solar simulation laboratory in the Department of Building Services Engineering of the Hong Kong Polytechnic University. The test rig included a well insulated calorimeter box and a solar simulator which provides uniform simulated light to the module surface. The calorimeter box,

which was mounted with a PV module on its front side, was placed under the solar simulator so that a constant solar radiation was struck on the module surface and heat was transmitted through the module as well. The interior temperature of the calorimeter box was kept constant by a chilled water circulation system. The amount of heat transmitted through the PV module was evaluated by measuring the heat rejected by the chilled water. The exterior and interior temperature of the calorimeter box, the ambient temperature, the water flow rate, the water inlet and outlet temperature were logged at constant time interval. The SPVHG model can then be validated by comparing the measured module's surface temperatures and the total heat gain at the equilibrium state with the corresponding calculated values by the model. Figure 3.3 is a photo of the test rig.

Figure 3.1 BIPV system in the campus of The Hong Kong Polytechnic Unversity

Figure 3.2 The Solar simulator

Figure 3.3 The test rig for studying heat transfer through a semi-transparent BIPV module

3.3 SUMMARY

The methodology of the current research has been described in this chapter. The methods for the current research involve both theoretical studies and experimental studies. Theoretical studies include the development of various simulation models, namely the SPVHG model, a power generation model and an indoor illuminance model. The SPVHG model is established by formulating transient heat transfer equations for the elements of the PV modules, while the power generation model and the indoor illuminance model are developed by modifying existing models. As a result, the overall energy performance of the semi-transparent BIPV modules can be evaluated in terms of heat gain, power production and daylight admission.

In order to verify the reliability of the simulation models, a number of experiments are designed. The experiments are carried out under realistic conditions using an existing BIPV system, as well as laboratory conditions for controlling particular parameters. The experimental data was analyzed and compared against the results from the simulation models to show the validity of the models.

CHAPTER 4

SOLAR RADIATION ON AN INCLINED SURFACE AND OPTIMUM INCLINATION

The semi-transparent BIPV modules are usually installed vertically if they are used as window glazing. The modules can also be installed at different orientations and inclinations in order to enhance energy efficiency and to harmonize the appearance of the building. Since the amount of heat transmitted through a semi-transparent BIPV module and its daylight utilization level are highly affected by the amount of solar radiation that strikes on its surface, it is necessary to model the solar radiation on a module's surface of different inclinations and orientations is necessary in order to assess the energy performance of the BIPV module.

The Hong Kong Observatory has regular records on the global solar radiation on horizontal surfaces. However, the solar radiation on different orientations and inclination is not available. Simulation models that estimate the solar radiation received on different orientations and inclinations will be described in this chapter. Four well established diffuse radiation models for inclined surface are compared and analyzed. The optimum position and tilted angle can subsequently be determined for Hong Kong conditions. The solar radiation models were also validated by experimental studies. In addition to semi-transparent BIPV modules, the models and the results described in this chapter are suitable for other kinds of solar applications such as solar thermal collectors and daylight utilization.

4.1 BACKGROUND

The amount of solar radiation captured by a solar collecting surface, no matter whether it is a solar thermal collector or a photovoltaic module, is affected by the inclination and orientation of the surface. In recent years, a considerable number of studies have been carried out on the investigation of solar radiation on inclined surfaces (Asl-Soleimani et al., 2001; Bari 2000; Burlon et al., 1991; Mahmound et al., 1990; Shariah et al., 2002; Tiris et al., 1997; Yakup, et al., 2001 and Zuhairy, et al., 1995). The total solar radiation can be evaluated by adding the three components: (a) beam component; (b) reflected component and (c) sky diffuse component. Beam and ground-reflected components can be calculated in a straight-forward way while more considerations are required in the calculation of sky diffuse component due to the ever changing sky conditions. A number of diffuse solar radiation models have been developed by various scholars. In this chapter, four important diffuse radiation models for inclined surface, including Liu & Jordan (1960), Perez et al. (1990), Hay & Davies (1980) and Reindl et al. (1990), are reviewed and compared. Horizontal global solar radiation records of year 1989 were used as part of the inputs to the models. The five most favorable orientations for Hong Kong solar applications, including east, south-east, south, south-west and west were studied for the solar energy received at different slope. The results are applicable to all kinds of solar applications, such as solar thermal collectors, opaque and semi-transparent BIPV modules etc. Engineers can also make reference to the results in their design of solar collecting systems.

4.2 SOLAR RADIATION ON AN INCLINED SURFACE

The total radiation (in J/m^2) on a tilted surface, $G_{tot,T}$, comprises three components: beam radiation (G_{bT}), reflected radiation (G_{gT}) and diffuse radiation (G_{dT}). The total radiation is the sum of the three components. In mathematical form, it can be written as,

$$G_{tot,T} = G_{bT} + G_{gT} + G_{dT} \tag{4.1}$$

The three components can be evaluated individually. Each of them is discussed separately in the following sections.

4.2.1 Beam radiation on an inclined surface

The beam solar radiation that reaches a surface is related to the various solar angles and local latitude. In order to establish the relationship between the tilted angles and the solar radiation on the corresponding surface, one should start from solar geometry.

According to Duffie and Beckman (1980), for a tilted surface with β degree, the angle of incidence of beam radiation, θ, is given by,

$$\begin{aligned}\cos\theta = {} & \sin\delta\sin\phi\cos\beta - \sin\delta\cos\phi\sin\beta\cos\gamma \\ & + \cos\delta\cos\phi\cos\beta\cos\omega \\ & + \cos\delta\sin\phi\sin\beta\cos\gamma\cos\omega \\ & + \cos\delta\sin\beta\sin\gamma\sin\omega\end{aligned} \tag{4.2}$$

As shown in equation (4.2), the beam radiation incidence angle is a function of a series of solar geometry angles. ϕ is the local latitude, which equals to 22.3° N for Hong Kong. ω is the hour angle, which represents the angle between the meridian of

the sun and the local meridian. γ is called surface azimuth, which is the angle between the vertical plane containing the normal to wall and the vertical plane running north-south. The surface azimuth is measured from the south, which is negative when the sun is to the east of south but positive when the sun is to the west of south. δ is the solar declination which defines the angle between the sun-earth line and the equatorial plane. It varies from +23.5° to -23.5° throughout a year. On the equinoxes, δ is 0° while on summer solstice and winter solstice, δ is +23.5° and -23.5° respectively. Accurate values of δ on a particular day can be determined by the following equation by inputting the day number *n*,

$$\delta = 23.45 \sin\left(\frac{360 \cdot (284 + n)}{365}\right) \tag{4.3}$$

For a horizontal surface, β equals 0°. The angle of incidence is the zenith angle of the sun, which is denoted by θ_z. Equation (4.2) becomes:

$$\cos\theta_z = \cos\delta\cos\phi\cos\omega + \sin\delta\sin\phi \tag{4.4}$$

For a tilted surface, a relationship between the angle of incidence and the tilted angle was described by Duffie and Beckman (1980). They stated that the surfaces with slope β have the same angular relationship to beam radiation as a horizontal surface at the location that having latitude of (ϕ–β). Figure 4.1 shows this relationship for the northern hemisphere. For a surface facing south, and replacing ϕ with (ϕ–β) in equation (4.4) yields,

$$\cos\theta = \cos(\phi - \beta)\cos\delta\cos\omega + \sin(\phi - \beta)\sin\delta \tag{4.5}$$

The beam solar radiation on a tilted surface can be obtained by multiplying a ratio R_b to the horizontal beam solar radiation. The ratio R_b is defined as the ratio of

beam radiation on a tilted surface to horizontal surface. It was developed by Hottel and Woertz 1942 (cited in Duffie and Beckman 1980: p.16). It can be expressed in terms of the angle of incidence and the zenith angle of the sun as follows,

$$R_b = \frac{G_{bT}}{G_b} = \frac{G_{bn}\cos\theta}{G_{bn}\cos\theta_z} = \frac{\cos\theta}{\cos\theta_z} \tag{4.6}$$

where G_b is the horizontal beam radiation, G_{bn} is the direct normal radiation to the surface. As a result, modifying equation (4.6), beam radiation on a tilted surface can be evaluated by,

$$G_{bT} = G_b \cdot R_b = G_b \cdot \frac{\cos\theta}{\cos\theta_z} \tag{4.7}$$

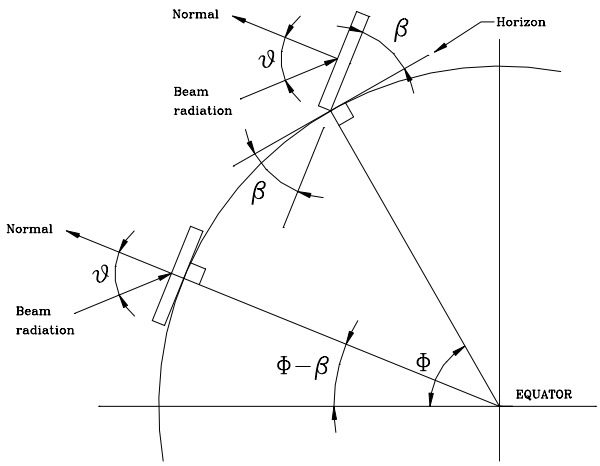

Figure 4.1 Angular relationship between a horizontal surface and an inclined surface with tilted angle β

By using equation (4.7), the beam component of the solar radiation of an inclined surface can be determined.

4.2.2 Reflected radiation on an inclined surface

The reflected component of the solar radiation takes into account all the reflected radiation from other surfaces in the surroundings. In general, it is not possible to calculate the reflected energy from the surfaces in detail because of the changing solar radiation incident on them, and their changing reflectances. In order to calculate the reflected term, it is assumed that all the surrounding surfaces are condensed into one large horizontal, diffusely reflecting ground. The radiation reflected from this composite "ground" contributes to the reflected component.

The inclined surface with β degree to the horizontal has a view factor to the ground of $(1-\cos\beta)/2$. If the ground has a reflectance of ρ for the total solar radiation, the reflected radiation from the ground, G_{gT} can be written as,

$$G_{gT} = (G_b + G_d)\rho(\frac{1-\cos\beta}{2}) \tag{4.8}$$

where G_d is the horizontal diffuse radiation.

The ground reflectance ρ is assumed to be 0.2 for the Hong Kong weather where there is no snow. For other situations, for example if there is a fresh snow cover, the value should be 0.7.

4.2.3 Diffuse radiation on an inclined surface

Diffuse radiation on a tilted surface is the most difficult component to be modeled accurately due to its spatial distribution. Many previous studies have been conducted on the mathematical modeling of diffuse radiation on a slope. These models differ in the assumed diffuse radiance distribution at different states of

cloudiness. It is vital to choose a suitable model for the diffuse radiation in order to reduce the error. Four popular diffuse radiation models for inclined surface were selected for comparisons. The following sections give a brief description of each of the models.

4.2.3.1 The Liu & Jordan model

Liu & Jordan (1960) assumed an isotropic distribution of the diffuse radiance of the hemisphere in their model. Using this assumption, the diffuse radiation on a slope can be calculated by the product of the horizontal diffuse radiation (G_d) and the view factor from the surface to the sky as follows,

$$G_{dT} = G_d \left(\frac{1+\cos\beta}{2}\right) \tag{4.9}$$

This assumption simplified the calculation. Under a completely cloudy sky, this model gives accurate results. However, as the sky gets clearer, this model becomes unreliable due to the presence of circumsolar and horizon brightening anisotropic effect.

4.2.3.2 The Perez model

Perez et al. (1986) first developed a diffuse radiation model in 1986. They revised the model several times afterwards (Perez et al., 1987 & 1990). In the latest version of their model, the circumsolar and the horizon/zenith anisotropy are controlled by the coefficient F'_1 and F'_2 respectively. These coefficients are functions of the sky's clearness ε, the sky's brightness Δ and the solar zenith angle θ_z. The solar zenith angle θ_z was defined in equation (4.4), while the sky's clearness ε and

the sky's brightness Δ are defined as follows,

$$\varepsilon = \frac{(G_{dh} + G_{bn}/G_{dh}) + 1.041\vartheta_z^3}{1 + 1.041\vartheta_z^3} \tag{4.10}$$

$$\Delta = \frac{G_{dh} \cdot m}{G_o} \tag{4.11}$$

where m is the air mass, G_o is the extraterrestrial radiation and θ_z is in radian. G_o in an hour period can be estimated according to the method proposed by Duffie and Beckman (1980) as follows,

$$\begin{aligned} G_o = & \frac{12 \times 3600}{\pi} S_{sc} \left[1 + 0.033 \cos \frac{360n}{365} \right] \\ & \times \left[\cos\phi \cos\delta (\sin\omega_2 - \sin\omega_1) + \frac{2\pi(\omega_2 - \omega_1)}{360} \sin\phi \sin\delta \right] \end{aligned} \tag{4.12}$$

where S_{sc} is the solar constant which equals to 1367 W/m^2 (Sonnenenergie, 2005).

The coefficient F'_1 and F'_2 can be determined as a function of ε, Δ and θ_z with a table of 48 experimental coefficients. The coefficients of the most updated version announced by Perez et al. (1990) were used in the current comparison.

By assuming that all circumsolar radiance originates from a point source, the diffuse radiation on a slope can be estimated by,

$$G_{dT} = G_d \left[F_1' \frac{\cos\vartheta}{\cos\vartheta_z} + (1 - F_1') \cos^2\left(\frac{\beta}{2}\right) + F_2' \sin\beta \right] \tag{4.13}$$

4.2.3.3 The Hay & Davies model

Hay & Davies (1980) proposed an index A_I to weigh the circumsolar and the isotropic irradiance components. The index is used to account for the circumsolar anisotropy under clear sky conditions at the circumsolar area of the sky since that area

is usually brighter than the sky on average. A_I is defined as follows,

$$A_I = \frac{G_b}{G_o} \tag{4.14}$$

The diffuse radiation on an inclined surface in the Hay & Davies model can be expressed as,

$$G_{dT} = G_d \left[(1 - A_I) \frac{(1 + \cos\beta)}{2} + A_I \frac{\cos\vartheta}{\cos\vartheta_z} \right] \tag{4.15}$$

4.2.3.4 The Reindl model

Reindl et al. (1990) added a horizon brightening diffuse term to the Hay & Davies model to form their model. The magnitude of the horizon brightening is controlled by a modulating function *f*, which is given by,

$$f = \sqrt{\frac{G_b}{G_{tot}}} \tag{4.16}$$

where G_{tot} is the total horizontal radiation.

Reindl modified the model proposed by Temps and Coulson (1977) by multiplying the modulating function *f* to the horizon brightening correction term $\sin^3(\beta/2)$. Thus, the diffuse radiation on an inclined surface in the Reindl model can be evaluated from the equation:

$$G_{dT} = G_d \left[(1 - A_I)(1 + f \sin^3(\beta/2)) \frac{(1 + \cos\beta)}{2} + A_I \frac{\cos\vartheta}{\cos\vartheta_z} \right] \tag{4.17}$$

4.2.4 Diffuse radiation on a horizontal surface

As can be seen in the previous section, the total and diffuse solar irradiance on

horizontal surfaces are necessary inputs to the radiation models for inclined surface. Although the total horizontal solar radiation can be obtained from The Hong Kong Observatory, data on beam and diffuse solar radiation on horizontal surface are not readily available. Therefore, a correlation between horizontal diffuse and horizontal total solar radiation is required. A model which is based on local measured data was developed by Yik et al. (1995) to simulate the relationship between the horizontal diffuse radiation (G_d) and horizontal total radiation (G) for Hong Kong conditions. The correlations are as follows,

$$\frac{G_d}{G} = 1 - 0.435 \cdot k_T \qquad \text{For} \quad 0 \le k_T < 0.325 \tag{4.18}$$

$$\frac{G_d}{G} = 1.41 - 1.695 \cdot k_T \qquad \text{For} \quad 0.325 \le k_T \le 0.679 \tag{4.19}$$

$$\frac{G_d}{G} = 0.259 \qquad \text{For} \quad k_T > 0.679 \tag{4.20}$$

The above correlation involves the sky clearness, k_T, which is defined as the ratio of the total horizontal radiation (G_{tot}) to the extraterrestrial radiation (G_0). By using equations (4.18) to (4.20), G_d can be evaluated, thus the horizontal beam solar radiation (G_b) can also be obtained. Hence, the three components of the total radiation on a tilted surface (G_{bT}, G_{gT} and G_{dT}) can be calculated by using the radiation models as described in section 4.2. As a result, the total solar radiation on a slope at any orientation is obtained by simply applying equation (4.1).

The result obtained from equation (4.1) is the hourly total solar radiation in J/m^2. Since the average solar intensity (i.e. solar irradiance) in W/m^2 is usually desired in the application of the Semi-transparent PhotoVoltaic Heat Gain (SPVHG) model, the solar radiation value can be divided by 3600 to obtain the average value. The total

solar irradiance on a tilted surface is denoted as S_o.

4.3 ANNUAL SOLAR RADIATION MODELING

The hourly solar radiation on different inclinations and orientations throughout a year was calculated by using the horizontal solar radiation data in the typical year 1989. Data from the year 1989 was used because the weather in that year has been found to be the most representative based on a statistical analysis of Hong Kong weather data performed by Wong and Ngan (1993). The hourly results were then combined to obtain the annual total radiation for each inclination and orientation. Since the amount of beam and ground-reflected radiation is the same for all the radiation models, the differences in the results are only due to the diffuse radiation. In this chapter, results from different models are compared firstly. The effects of the tilted angle and the orientation are then described.

4.3.1 Comparisons of different models

4.3.1.1 East- and southeast-oriented surface

On the east- and the southeast-oriented surface, the Perez model predicts the smallest value of annual solar radiation among the four models on average, especially on east-oriented surfaces. The difference between the results from the Perez model and the other models is comparatively large. The greatest difference between the

results from the Perez model and the other models of 16.4% was recorded at 90° inclination (vertical position), while the other three models give the similar results on both east- and the southeast-oriented surfaces.

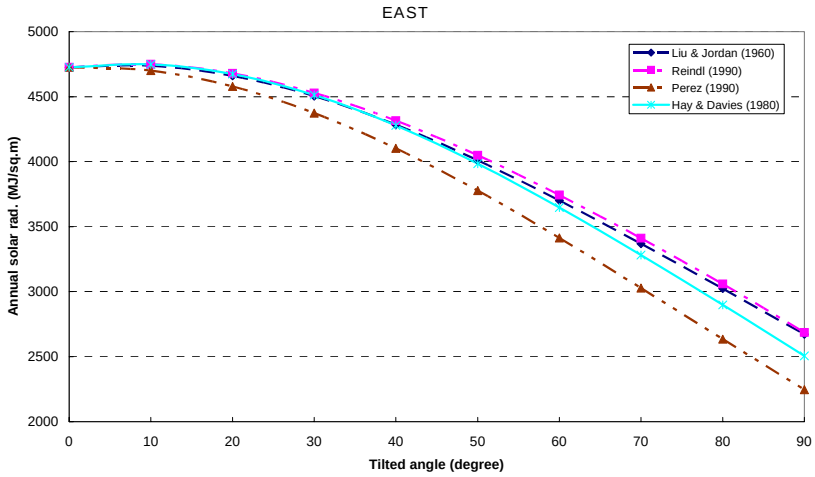

Figure 4.2 Annual solar radiation for east-oriented surface

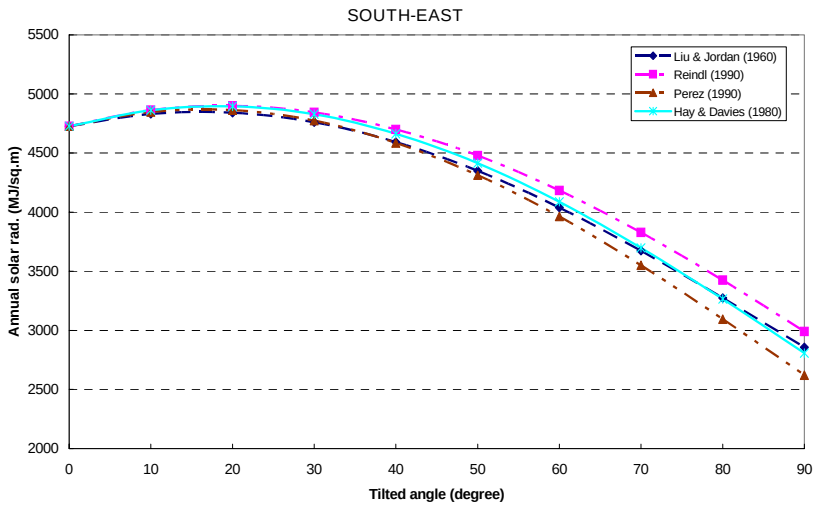

Figure 4.3 Annual solar radiation for southeast-oriented surface

4.3.1.2 South-oriented surface

For the south-oriented surface, the results from all four models are similar. The Liu & Jordan model gives the smallest annual solar radiation on average. At large

tilted angles, the results from the Reindl model slightly deviate from that of the other models.

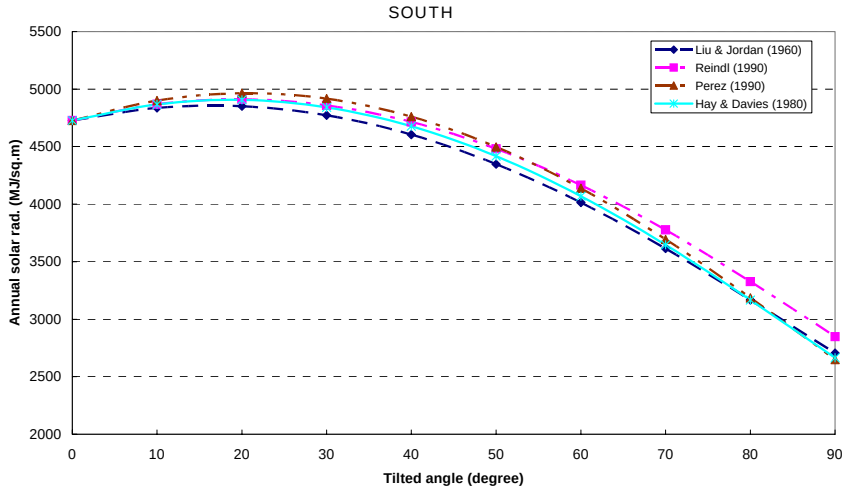

Figure 4.4 Annual solar radiation for south-oriented surface

4.3.1.3 Southwest- and west-oriented surface

In general, the results from all four models are similar for the southwest- and west-oriented surface, except the results from the Perez model and the Hay & Davies model at some ranges of tilted angle. The results of the Perez model deviate from the other models obviously at tilted angles from 20° to 60°. The Hay & Davies model leads to a large difference on west surface at a tilted angle greater than 60°, while the Reindl model and the Liu & Jordon model agree with each other at other tilted angles for the southwest and the west-oriented surface.

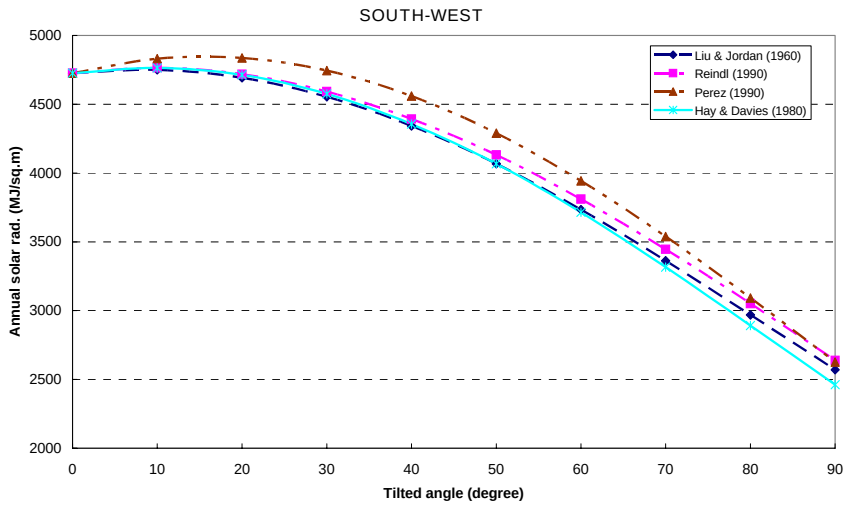

Figure 4.5 Annual solar radiation for southwest-oriented surface

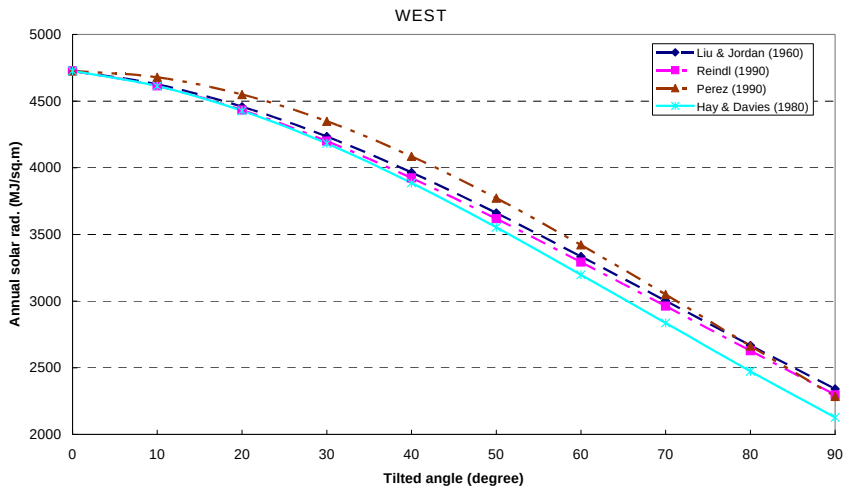

Figure 4.6 Annual solar radiation for west-oriented surface

4.3.2 Comparisons of different orientations

In addition to comparisons of different models, comparison of different orientations is also a major objective of this study. Taking the Reindl model as a demonstrative example, the annual solar radiation of different orientations and tilted angles were plotted in Figure 4.7. As shown in the figure, the south and southeast

surfaces tilted at around 20° receive the greatest amount of solar radiation. The values of annual solar radiation for these two orientations are very similar at tilted angle from 0° to 60°. When the tilted angle exceeds 60°, southeast-oriented surface receives slightly more solar radiation than the south-oriented surface.

To analyze further the solar radiation for different orientations, three tilted angles including 0°, 20° and 90° were chosen for comparison. 0° and 90° are the horizontal and vertical positions respectively. 20° was chosen because the optimum angle is near 20° for the south and southeast-oriented surface as revealed in Figure 4.7. The results of the comparison are shown in Figure 4.8. It can be seen that at 20° tilted surface, due south is the best choice, and due southeast also has a similar performance to the south direction. For vertical position (90°), southeast performs the best while the next is the south. On the whole, the best three orientations are southeast, south and southwest. Conversely, the least solar radiation can be received when the surface is oriented due west.

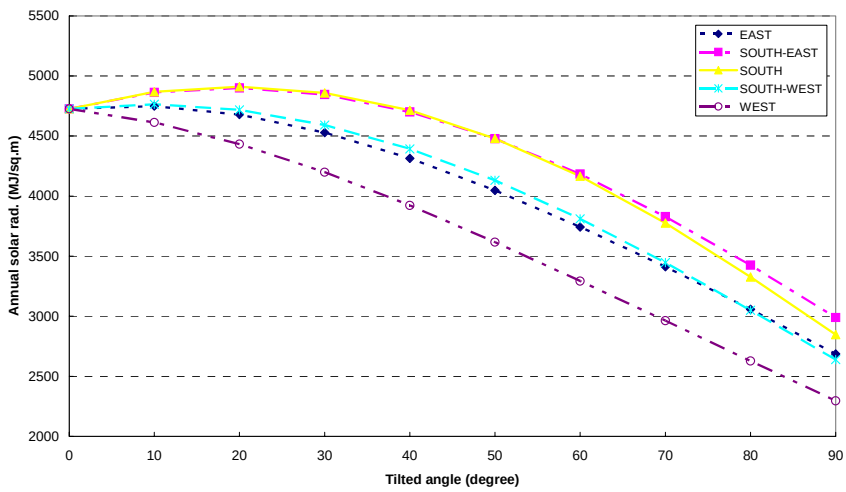

Figure 4.7 Annual solar radiation of different orientation

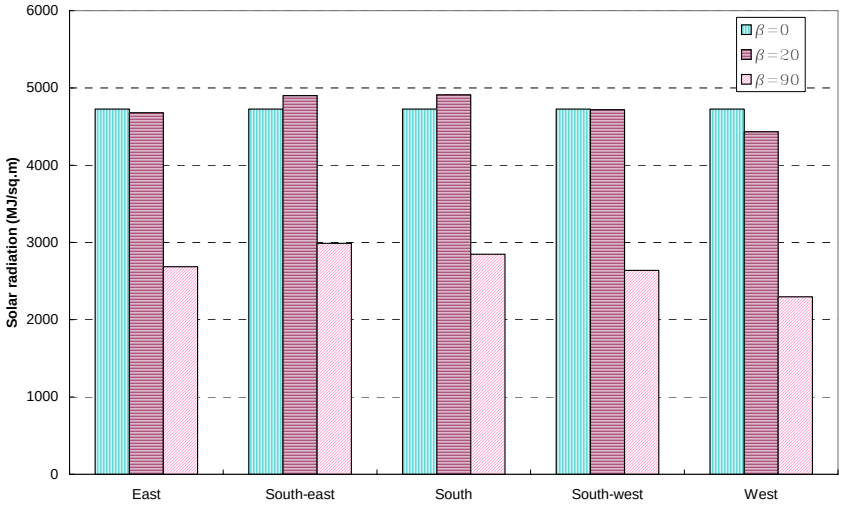

Figure 4.8 Annual solar radiation at tilted angle equals 0 ˚, 20 ˚ and 90 ˚

It can be observed that more solar radiation is yielded at east-oriented surfaces than that of west-oriented surfaces. This result is different from the general perception that west-oriented surfaces receive more sunshine than the east in Hong Kong. In order to explain this discrepancy, the solar radiation data in the year 1989 (the data adopted in the simulation) have been examined. It was found that the total amount of solar radiation in morning time (from 0500 to 1200) is greater than that in the afternoon time (from 1200 to 1900) by 27.5%. Therefore, it is reasonable that the east-oriented surface receives more solar radiation than the west-oriented surface. However, when conducting the same comparison by using the data in other five years (1900-1994), the reverse was observed. Although the solar radiation pattern in the year 1989 is different from the other years, the weather data in this year was found to be the most representative weather data (Wong and Ngan, 1993). Therefore, as illustration purpose, the 1989 weather data set was adopted in this study. However, it is suggested to critically examine the solar radiation data of different years to select an

appropriate test reference year for solar energy application study in Hong Kong.

As the results shown in section 4.3.1 reveal, more solar radiation can generally be received at the small tilted angles than large tilted angles in Hong Kong. As shown in Figure 4.7, the maximum solar radiation occurs at tilted angle of around 15° to 20°. When the tilted angle exceeds 40°, the values of solar radiation drop sharply. This phenomenon can be explained by the geographical location of Hong Kong. The local latitude of Hong Kong is 22.3° N, which is within the tropical region. It is therefore reasonable that small inclination angles that close to the local latitude value perform better throughout a year. However, the optimum angle may not necessarily equal to the local latitude. This fact will be elaborated in the following paragraph.

The optimum angles at different orientations were obtained by using the Reindl model and the Perez model. The maximum point of each curve in Figure 4.2 to Figure 4.6 is the point where optimum inclination occurs. Table 4.1 summarizes the optimum angles and corresponding solar radiation at the optimum angle for each of the orientations calculated by the two models.

As indicated in Table 4.1, smaller optimum tilted angles were obtained from east- and west-oriented surfaces, and even 0° (horizontal position) was obtained on west-oriented surface. For the south-oriented surface, the simulation result shows that the optimum angle is smaller than the local latitude (22.3°) rather than exactly the same as the local latitude for both models.

Table 4.1 Optimum angles and corresponding solar radiation

Orientation		Reindl model	Perez model
East	Optimum angle:	7.2 °	2.7 °
	Sol. Radiation (MJ/m^2):	4752.8	4730
Southeast	Optimum angle:	19.0 °	16.0 °
	Sol. Radiation (MJ/m^2):	4901.3	4867.2
South	Optimum angle:	19.5 °	20.7 °
	Sol. Radiation (MJ/m^2):	4911.5	4963.7
Southwest	Optimum angle:	9.4 °	15.6 °
	Sol. Radiation (MJ/m^2):	4765.0	4846.5
West	Optimum angle:	0 °	0 °
	Sol. Radiation (MJ/m^2):	4726.4	4726.4

The reasons for this are closely related to local meteorology. In Hong Kong, there are many cloudy days in winter and spring. In contrast, more sunny days and stronger solar radiation are available in the summer. Thus, the tilted angle chosen should be such that it suits better the summer conditions in Hong Kong in order to maximize the solar radiation availability in a year. In summer, the altitude of the sun (i.e. the angle between the sun's beam radiation and the horizontal plane) is larger than that of winter. Therefore, the tilted angle of the surface should be smaller in summer than in winter in order to receive more beam solar radiation.

In fact, the optimum angle of a solar collecting surface depends greatly on the type of application, such as PV grid connected system, PV stand-alone system and solar hot water system. For grid connected system, PV modules' tilted angle should be the angle at which the annual electricity production is maximized. If a stand-alone system is adopted, the tilted angle of PV modules should be selected so that the modules can receive the most solar energy during the seasons which have the least

solar radiation (e.g. in spring). This angle is not necessarily equal to the one which maximizes the annual energy generation. The reason for this is to make sure that the energy demand can still be satisfied even though the available solar radiation is less in those seasons. Another advantage of this design is that it can minimize the storage battery size. The concept of designing the optimum tilted angle for solar hot water system is similar to that of PV stand-alone system. The optimum tilt angle of solar hot water system is not necessarily equal to the one which maximizes the solar radiation collection. Instead, the angle should be the one that maximizes the annual solar fraction (i.e. the fraction of load supplied by solar energy) of the system in a year. Further research should be carried out to study the optimum inclination for various solar energy applications in Hong Kong.

4.4 VERIFICATION OF SOLAR RADIATION MODELS

Comparisons between the solar radiation models and on-site solar radiation data have been carried out by various researchers in different countries (Muneer, 1990; Skiba, 1996; Vartiainen, 2000). Li (2000) also performed a solar radiation comparison using three anisotropic models with the measured data in Hong Kong. However, only vertical surfaces were considered in Li's study. In order to draw a more comprehensive conclusion for Hong Kong conditions, it is important to include various tilted surfaces. Measurements and comparisons of the solar radiation on both the tilted surfaces and vertical surfaces have been conducted in this study. In this

section, the comparisons of different radiation models for the inclined surfaces with the measured data are presented. The Reindl and the Perez model were selected for the comparison because these two models have been proven by various studies to be the most accurate model among the others (Muneer, 1990; Skiba, 1996; Vartiainen, 2000; Li, 2000; Lu, 2004).

4.4.1 Solar radiation measurements

The solar radiation data was collected on the roof of the Shaw Amenities building at the Hong Kong Polytechnic University. This does not receive any shading from other buildings nearby throughout a day. The measurement was carried out between mid June and mid July of 2003. The data taken in this period is comprehensive because both sunny and overcast sky conditions were included. The data were logged at five-minute intervals. Hourly solar radiation values were obtained by taking the hourly average of the logged values.

Two identical Kipp & Zonen pyranometers of model CM11 were used to measure global solar irradiance. One of the pyranometers measured the global horizontal solar irradiance, and the other was oriented to the south and inclined with 23° to the horizontal, or placed vertically facing the east, south or west. In this way, two sets of solar irradiance data were recorded, one is the horizontal irradiance and the other is the inclined irradiance.

4.4.2 Results of the verification

The hourly horizontal irradiance values recorded were input to the two radiation

models for inclined surface to obtain the tilted solar irradiance values. The values were then compared to the corresponding measured values. Figure 4.9 and 4.10 show the comparison results of the 23° tilted surface and vertical surface on different measuring days. As can be seen in the figure, both the Reindl and the Perez models agree well with the experimental data in general, especially for the 23° tilted surface as shown in Figure 4.9. For the vertical surfaces, the two simulation models predict the actual situation well in general, but comparatively larger discrepancies are observed at the early morning and late afternoon because of the increased amount of diffuse solar radiation. To enable further analysis of the performance evaluation of the models, the mean bias error (MBE) and the root mean square error (RMSE) were also calculated. The definitions of the two parameters are as follows,

$$MBE = \left(\frac{\sum_{j=1}^{n} (G_{j,sim} - G_{j,meas})}{n} \right) \Bigg/ \left(\frac{\sum_{j=1}^{n} G_{j,meas}}{n} \right) \tag{4.21}$$

$$RMSE = \left(\sqrt{\frac{\sum_{j=1}^{n} (G_{j,sim} - G_{j,meas})^2}{n}} \right) \Bigg/ \left(\frac{\sum_{j=1}^{n} G_{j,meas}}{n} \right) \tag{4.22}$$

The values of the MBE and RMSE of different cases are shown in Table 4.2. Satisfactory results of small errors were obtained from both models for the 23° tilted surface. However, the results of vertical surfaces have larger errors than the 23° tilted surface. It is because the vertical surfaces received more diffuse radiation. The simulation models have a less satisfactory performance in predicting the diffuse radiation. Therefore, further improvement should be carried out on the solar radiation

models to enhance their accuracies especially in the extreme conditions such as the early morning and the late afternoon. Also, for more comprehensive results, solar radiation data of at least one year should be compared. Since the focus of the current research is not on the development of solar radiation model, only a brief study was carried out.

When comparing the Reindl and the Perez models, Reindl model has smaller values of both MBE and RMSE for most of the cases. This implies the Reindl model is more accurate than the Perez model when applying to local conditions.

Table 4.2 MBE and RMSE of the two radiation models for different surfaces

Orientation		**Reindl model**	**Perez model**
23 degree tilted, due South	**MBE**	0.6%	1.7%
	RMSE	6.3%	7.9%
East (Vertical)	**MBE**	31.6%	-7.6%
	RMSE	77.2%	50.6%
South (Vertical)	**MBE**	-6.3%	-27.3%
	RMSE	55.8%	58.4%
West (Vertical)	**MBE**	-0.8%	-4.7%
	RMSE	44.2%	57.7%

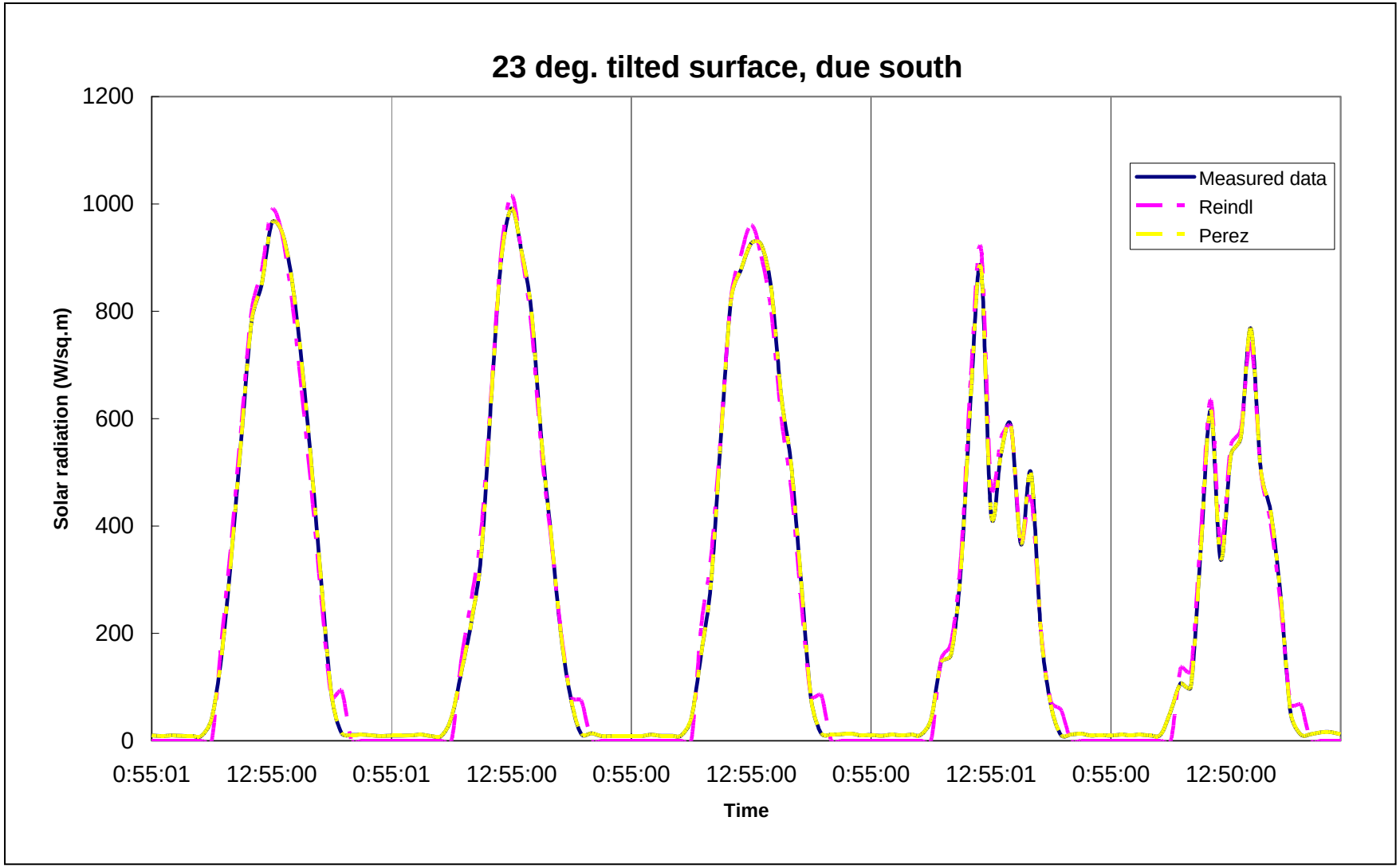

Figure 4.9 Comparisons on the results from the Reindls's and Perez's models with the measured data of 23° tilted surface on five typical days

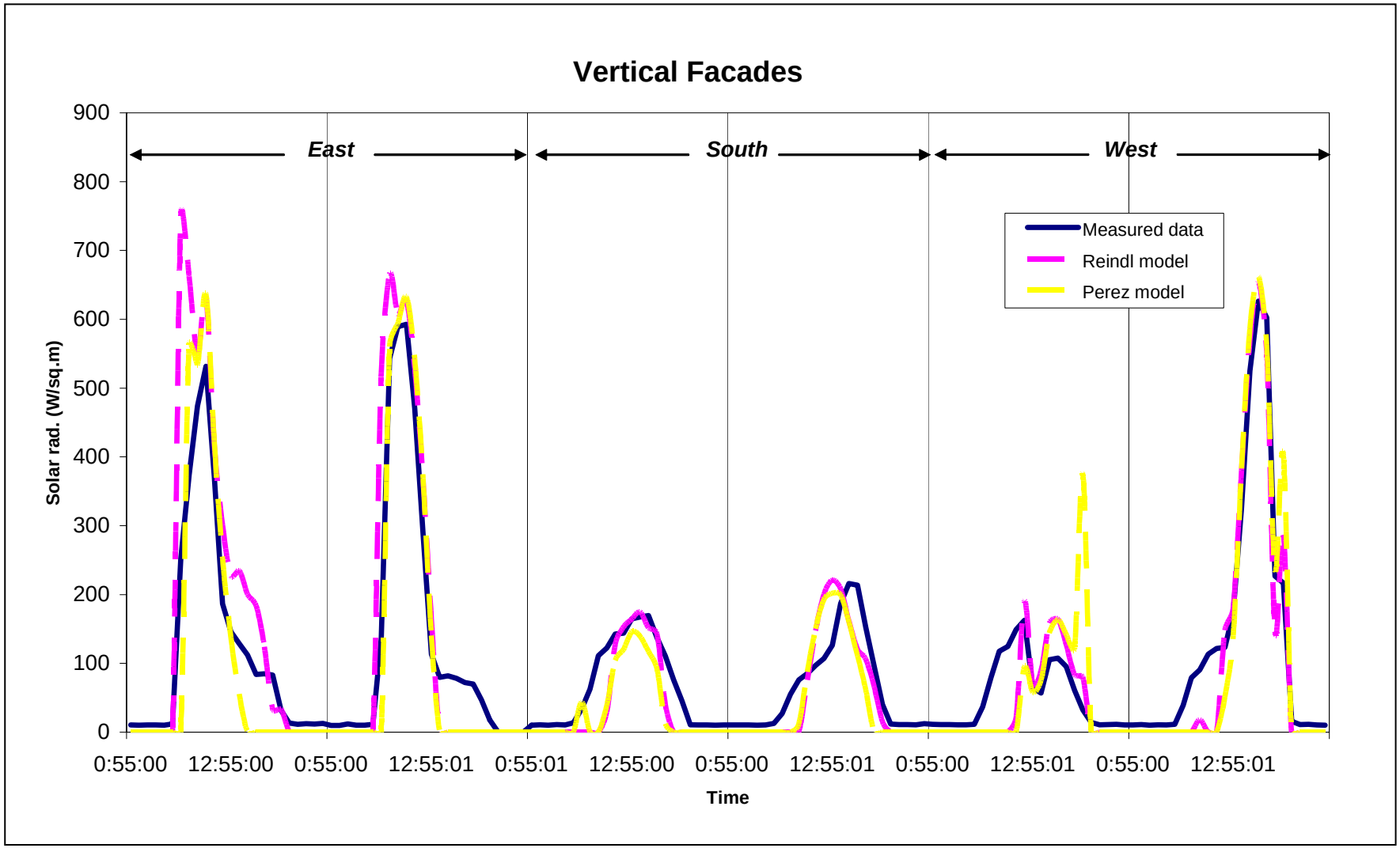

Figure 4.10 Comparisons on the results from the Reindls's and Perez's models with the measured data of vertical facades

4.4.3 Selection of radiation model for inclined surface

According to the comparison results, both the Reindl and the Perez models perform well on tilted surfaces. A number of comparison studies of different models have been conducted by various researchers such as Skiba et al. (1996), Vartiainen (2000), Li (2000) and Lu (2004). According to the comparison between the models and the on-site measurement carried out by the above researchers, the model by Perez was found to be the most accurate among the other models in general. However, the Reindl model performs the best in some studies and orientations (Skiba et al, 1996 and Vartiainen, 2000). For example, Vartiainen (2000) found that the Perez model results in the least error in all positions in general, and, according to Skiba et al. (1996), the Reindl model has the smallest mean bias error at vertical surface. In addition, according to the comparison in the current study, the Reindl model performs better for the local conditions.

From the perspective of model execution, the Perez model involves a large number of coefficients (forty-eight) in the calculation. In contrast, the execution of the Reindl model is much more straight-forward compared with the Perez model. Under the consideration of complexity and accuracy, the Reindl model was used in the development of the SPVHG model.

4.5 SUMMARY

This chapter has described the method for estimating the solar radiation on inclined surfaces. Four widely used radiation models for inclined surface are compared and analyzed. The annual solar radiation for different orientations and inclinations is estimated by using the radiation models. For vertical surfaces, the best orientation is southeast. The best tilted angle is around 20° to the horizontal when the surface is oriented to the south. On-site measurements were also carried out. The results of the measurement indicate that the Reindl and the Perez models are highly reliable.

The solar radiation model for inclined surface described in this chapter is used in the development of the SPVHG model to evaluate the solar irradiance on inclined semi-transparent BIPV modules, and thereby determining the solar heat gain through the modules. The solar radiation model forms a vital part of the SPVHG model.

The results presented in this chapter can act as a reference for the design of solar applications involving solar collecting surface such as BIPV systems and solar hot water systems. Designers can directly refer to the graphs shown in this chapter to assess the annual solar energy received on different orientations and inclinations. The results of this chapter can facilitate the design of solar energy systems.

CHAPTER 5

DEVELOPMENT OF THE SPVHG MODEL

Although the semi-transparent BIPV modules have become popular in building façade applications, there is no detailed study of their thermal performance. The thermal performance is important because it will consequently affect the electricity consumption of the air-conditioning systems. This chapter develops the Semi-transparent PhotoVoltaic Heat Gain (SPVHG) model for simulating the heat gain through this kind of PV module. The model is established by equating the energy balance for each discrete node across different layers of the module. In addition to the conduction heat transfer, solar heat gain is considered in the energy balance equations. Solar radiation that is transmitted, absorbed and reflected at each element of the module is considered from the optical and thermal perspectives. Convective and radiative heat exchange between the module and the ambient environment are also treated in the equations. The equations are then solved by numerical methods.

By using the SPVHG model, the amount of heat gain through the semi-transparent BIPV modules of different solar cell areas and glass thickness can be evaluated. A package of computer program using Visual C++ is written to facilitate the calculating procedure of the SPVHG model.

5.1 INTRODUCTION

Glazing is a common feature in modern commercial buildings as it allows natural light into the building and provides visual communication for occupants with outdoors. Since the mid 70's in the last century, enormous effort has been paid to provide the building façades with an extensive glazed area to fulfill the visual needs of people who view from both inside and outside of the building. Although the large glazed facades can be visually appealing, they increase the cooling demand and energy consumption of the air-conditioning systems in the building. A balance between the building aesthetic and the energy efficiency is needed.

In order to reduce energy consumption, it is necessary to introduce energy efficiency devices or systems in buildings. For building facades, attractive appearance and energy efficiency can be balanced by integrating innovative solar cells in glass sheets. In this way, the façade element can become a power generator as well as providing transparent area for the facade. The glass sheet that is integrated with solar cells is called semi-transparent BIPV modules.

In order to investigate the thermal performance of the semi-transparent BIPV modules, it is first necessary to understand their structure. A semi-transparent BIPV module comprises three layers: (i) A series of opaque solar cells that are placed between two highly transparent glass sheets, (ii) transparent resin encapsulation that occupies the spaces between each solar cell. Figure 5.1 shows a simple sketch of the cross-section of the semi-transparent BIPV module. In this way, the semi-transparent BIPV modules have multiple layers instead of a single sheet. Owing to the structure of this kind of module, the heat transfer process in it is different from ordinary glass

due to the presence of the opaque solar cells. Although the semi-transparent BIPV modules have become a popular option in modern architectures, there have been few studies which focus on their heat transfer performance in detail. A method for simulating the heat transfer of this kind of BIPV module is required. In the following section, the development of the SPVHG model is presented. By using the SPVHG model, the temperature distribution within the layers of the module can be determined. Subsequently, the heat gain through the module can be evaluated

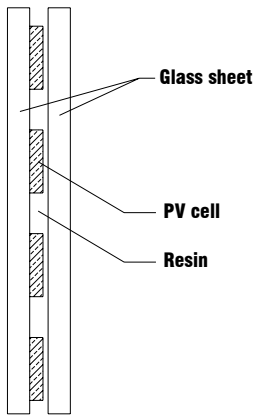

Figure 5.1 A typical structure of a semi-transparent PV glazing (not to scale)

5.2 THE SIMULATION MODEL

5.2.1 Heat transfer mechanism of the module

With regard to the structure of the semi-transparent BIPV modules, part of the module area is covered with opaque solar cells (mono- or poly- crystalline silicon) while the rest is wholly transparent. The analysis of heat transfer through the glazing

can be divided into two parts according to this structural characteristic. In the area covered by solar cells (henceforth referred to as the “solar cell part”), solar radiation is absorbed by the solar cell after passing through the laminated glass on the front. A certain amount of heat is also absorbed by the glass layers. The absorbed heat is then released gradually toward both the indoor and outdoor sides. In the area without solar cells (henceforth referred to as the “transparent part”), most of the solar radiation enters the interior environment directly through the glass, while a part of the solar radiation is absorbed by the glass and released gradually after a period of time. On both surfaces of the modules, absorbed heat is then exchanged with the ambient environment by means of convection and radiation.

When the modules are installed as a façade element, they are subjected to the ever changing environment such as the fluctuating air temperature and solar radiation level. These changes in the environment make the temperature distribution and the heat transfer of the modules unstable. In steady state conditions, it is assumed that the temperature distribution across the thickness of a solid remains unchanged. However, this assumption cannot be applied to the semi-transparent BIPV modules not only because of the changing ambient temperature and solar radiation, but also the presence of the non-homogeneous materials within the modules. Therefore, steady state method is not suitable in this case and unsteady state heat transfer analysis should be adopted to take the transient conditions and non-homogeneous elements into account.

The model described in this chapter allows radiation to be absorbed along the module thickness. Since the module is thin and large compared with its lateral dimensions, one direct of heat flow across the modules is assumed. To analyze the

unsteady state heat transfer problem, a one-dimensional transient energy model is established for each of the elements of the modules. The model development of the "solar cell part" and the "transparent part" will be discussed separately.

5.2.2 Solar cell part

The "solar cell part" of the module consists of three layers: the front-glass, the solar cells and the back-glass. The Front-glass denotes the layer of glass that contacts directly with the outdoor environment, while the back-glass denotes the glass that contacts directly with the indoors. Figure 5.2 illustrates the elements of the "solar cell part". As shown in the figure, the thickness of the module is represented by the distance measured from the interior surface of the back-glass, while the thickness of the back-glass is *L1* and that of the whole module is *L2*. The simulation model for each element is discussed separately in section 5.2.2.1 to 5.2.2.3.

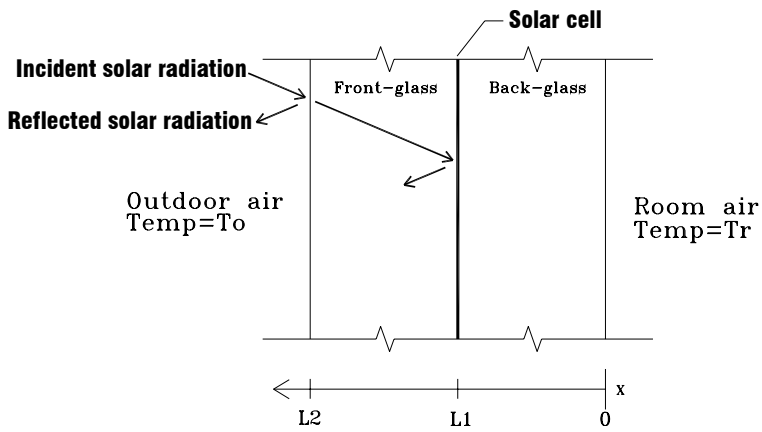

Figure 5.2 Elements of the "solar cell part"

5.2.2.1 The front-glass

The transient heat transfer problem of the front-glass can be analyzed by solving the heat conduction equation. As there is solar radiation passing through the glass, in addition to conduction, the radiation absorbed along the glass thickness should be included in the equation. The energy balance equation of the front-glass is,

$$\frac{\partial T_{fg}(x,t)}{\partial t} = \lambda_g \frac{\partial^2 T_{fg}(x,t)}{\partial x^2} + \frac{\lambda_g}{k_g} \cdot \frac{dS_{fg}}{dx} \tag{5.1a}$$

for $L2 < x < L1$. Here $T_{fg}(x,t)$ is the inside node temperature of the front-glass at distance x and time t; λ_g and k_g are the thermal diffusivity and thermal conductance of the glass respectively; the term dS_{fg}/dx corresponds to the heat generated in the glass due to the solar radiation, where S_{fg} is the solar intensity available at distance x, which can be rewritten based on the assumption that the absorbed radiation is proportional to the local intensity S in the glass and the distance X the radiation has traveled in the glass, i.e.,

$$dS = -(S \cdot K) \cdot dX \tag{5.1b}$$

where K is a proportionality constant, the extinction coefficient of the glass. Equation (5.1b) can be integrated to obtain S_{fg} at the point with distance x to the interior surface of the back-glass. By considering also the incident angle of the beam solar radiation and putting $X = (L2 - x)/\cos\vartheta_2$, S_{fg} can be written as,

$$S_{fg} = S_o \cdot \exp\left(\frac{-K(L2 - x)}{\cos\vartheta_2}\right) \tag{5.1c}$$

where S_o is the total solar irradiance just before entering the glass and θ_2 is the refraction angle of the beam solar radiation. S_o depends on the date, time, the sun's

position and horizontal solar irradiation etc. The procedure described in section 4.2 is used for determining S_o.

5.2.2.2 The solar cell

As solar energy reaches the solar cells, part of the energy will be converted into electricity, and the rest will be lost as heat. Therefore, the actual amount of heat dissipation from the solar cell depends on the amount of thermal energy being absorbed and the electricity conversion efficiency, η_{el}, of the solar cells. Also, the thickness of a mono- or poly-crystalline solar cell is in the order of 300 μm to 800 μm, which is negligible compared with the thickness of the glass layer (6mm to 12mm or above depending on the usage). Therefore, the heat balance equation can be established by only considering the absorbed thermal energy and the solar cell efficiency. The follow equation can be written for the energy entering and leaving the node at $x = L1$,

$$(S_o \cdot \tau_{fg} \cdot \alpha_{cell} - S_o \cdot \tau_{fg} \cdot \eta_{el}) = k_g \frac{\partial T_{bg}(x,t)}{\partial x} - k_g \frac{\partial T_{fg}(x,t)}{\partial x} \tag{5.2a}$$

The term $(S_o \cdot \tau_{fg} \cdot \alpha_{cell})$ is the total solar energy absorbed by the solar cells with absorptance α_{cell} after attenuation by the front-glass. The term $(S_o \cdot \tau_{fg} \cdot \eta_{el})$ is the amount of solar energy that is converted to electricity by the solar cells, where τ_{fg} is the transmittance of the front-glass, which is a function of the solar incident angles, and will be discussed in section 5.2.7. The difference between the above two terms is the heat dissipated by the solar cell (Brinkworth, 2000). The electricity conversion efficiency, η_{el}, of the solar cells depends on the conversion efficiency at standard test

conditions η_{STC} and solar cell temperature under operating condition T_{cell}. It is given by the following expression (Zondag et al., 2003; Sonnenenergie, 2005),

$$\eta_{el} = \eta_{STC} \cdot [1 - 0.0045(T_{cell} - 25)] \tag{5.2b}$$

Since T_{cell} is the temperature at the node $x = L1$ it can be obtained by solving equation (5.2a). The efficiency of the solar cell will be further discussed in Chapter 6, which focuses on the power generation of the BIPV modules.

5.2.2.3 The back-glass

A governing equation with the same principle as the front-glass can be set up for the heat transfer in the back-glass, but there is no solar radiation term because all solar radiation is blocked by the solar cell. The balancing equation can be written as,

$$\frac{\partial T_{bg}(x,t)}{\partial t} = \lambda_g \frac{\partial^2 T_{bg}(x,t)}{\partial x^2} \tag{5.3}$$

with $0 < x < L1$. Here $T_{bg}(x,t)$ is the inside node temperature of the back-glass at distance x and time t.

Having introduced the transfer equations of the “solar cell part”, the “transparent part” of the semi-transparent BIPV module is discussed in the next section.

5.2.3 Transparent part

The elements in the “transparent part” of the module are similar to those of the “solar cell part” but instead of the solar cells, a layer of transparent bonding material is situated in between the two glass layers. The layer of transparent bonding material is added during the encapsulation process, when the cell strings are embedded in the

material for fixing the positions of the solar cells as well as isolating electricity. For the semi-transparent BIPV modules, EVA and casting-resin encapsulation are usually adopted. The elements in the “transparent part” are shown in Figure 5.3.

Since the heat transfer process at the front-glass of the “transparent part” is the same as that of the “solar cell part”, the heat transfer equations for the front-glass of the “transparent part” are referred to section 5.2.2.1.

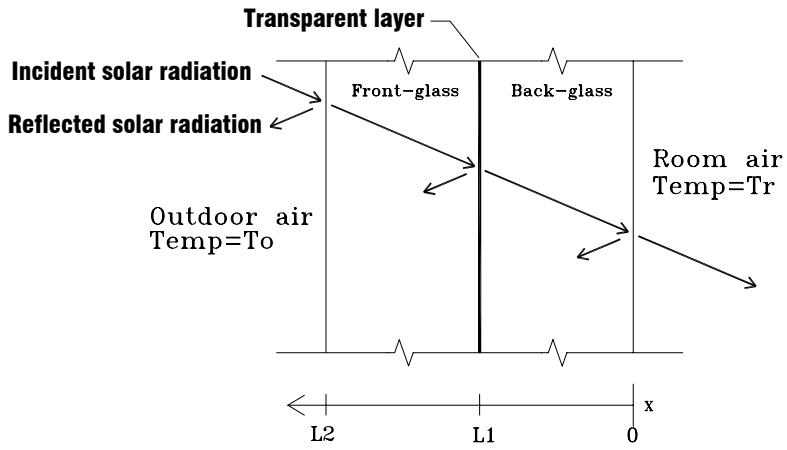

Figure 5.3 Elements of the “transparent part”

5.2.3.1 Transparent layer

The thickness of the transparent layer is the same as the solar cell, which is also negligible compared with the thickness of the glass layer. Therefore, balancing the heat transfer at the node at $x = L1$ yields,

$$S_o \cdot \tau_{fg} \cdot \alpha_r + k_g \frac{\partial T_{fg}(x,t)}{\partial x} = k_g \frac{\partial T_{bg}(x,t)}{\partial x} \tag{5.4}$$

where α_r is the absorptance of the transparent material layer, which characterizes the fraction of the energy absorbed by the material.

5.2.3.2 The back-glass

The governing equation of the back-glass of the "transparent part" is similar to that of the "solar cell part" as described in section 5.2.2.3. However, unlike the "solar cell part", the back-glass in the "transparent part" receives solar radiation. Therefore, by considering also the heat generation due to the solar radiation, the governing equation of heat transfer within the back-glass of the "transparent part" is,

$$\frac{\partial T_{bg}(x,t)}{\partial t} = \lambda_g \frac{\partial^2 T_{bg}(x,t)}{\partial x^2} + \frac{\lambda_g}{k_g} \cdot \frac{dS_{bg}}{dx} \tag{5.5a}$$

This equation is applied to $0 < x < L1$. The derivation of the solar intensity S_{bg} is similar to the approach for deriving S_{fg} as described in section 5.2.2.1, but the attenuation of solar energy by the front-glass and the transparent material layer has to be taken into account. This effect can be modeled by including the solar energy transmittance of the front-glass and the transparent material layer in the equation. Therefore, the solar intensity S_{bg} available at a distance equal $(L1 - x)/\cos\vartheta_2$ for $0 < x < L1$ can be expressed as follows,

$$S_{bg} = S_o \cdot \tau_{fg} \cdot \tau_r \cdot \exp\left(\frac{-K(L1 - m \cdot \Delta x)}{\cos\vartheta_2}\right) \tag{5.5b}$$

where τ_{fg} and τ_r are the transmittances of the front-glass and the transparent material layer respectively. τ_{fg} varies with the solar incident angle. The simulation of this effect will be discussed in section 5.2.7.

5.2.4 Boundary conditions

The aim of the analysis in sections 5.2.2 and 5.2.3 is to determine the internal

temperature and thus the heat transfer due to conduction in the semi-transparent BIPV modules. At the two surfaces of the modules, convective and radiative heat transfers with the ambient air are also included. Another set of equations have to be established to define the surface conditions of the modules. The principle of setting up the boundary conditions of the modules is to equate the inflow and outflow energy of the surface node.

The exterior surface of the semi-transparent BIPV modules will be exposed to outdoor air and will exchange heat with the surroundings by convection and radiation heat transfer. Therefore, the energy balance at the surface can be described by,

$$-k_g \frac{\partial T_{fg}(L2,t)}{\partial x} = h_o\left[T_{fg}(L2,t) - T_{sky}\right] + \sigma\xi_g\left\{\left[T_{fg}(L2,t)\right]^4 - \left(T_{sky}\right)^4\right\} \tag{5.6a}$$

where h_o is the convective heat transfer coefficient on the outside surface of the modules; ξ_g is the emittance of the glass; σ is the Boltzmann constant and T_{sky} is the surface temperature of the sky dome. However, surface temperature of the sky dome is not available, ambient air temperature (T_o) is usually used to replace the sky temperature as an approximation. Therefore, equation (5.6a) can be modified as follow:

$$-k_g \frac{\partial T_{fg}(L2,t)}{\partial x} = h_o\left[T_{fg}(L2,t) - T_o\right] + \sigma\xi_g\left\{\left[T_{fg}(L2,t)\right]^4 - \left(T_o\right)^4\right\} \tag{5.6b}$$

At the interior side of the modules, heat is exchanged between the module's surface and the indoor air. A similar energy balance equation as equation (5.6) can be set up at the interior module surface,

$$-k_g \frac{\partial T_{bg}(0,t)}{\partial x} = h_r\left[T_{bg}(0,t) - T_r\right] + \sigma\xi_g\left\{\left[T_{bg}(0,t)\right]^4 - \left(T_r\right)^4\right\} \tag{5.7}$$

where h_r is the convective heat transfer coefficient on the inside surface of the

modules; T_r is the inside ambient air temperature.

The boundary conditions described by equation (5.6) and (5.7) are applicable to the exterior (at $x = L2$) and interior (at $x = 0$) surface of the modules respectively. Up to this point, the energy equations at all nodes of the semi-transparent BIPV module have been established. The corresponding temperature can be evaluated by solving those equations using the method described in the following section.

5.2.5 Numerical solutions

The one-dimensional transient energy equations as shown in sections 5.2.2 to 5.2.4 can be solved in various ways, for instance, by using analytical methods such as Response Factor Method and Transfer Function Method. An alternative approach that is also widely used in modeling heat transfer in buildings is to solve the partial differential equations using numerical methods, such as finite difference method and the finite element method. The analytical methods are appropriate for the solution of systems of linear different equations that having time invariant parameters. On the other hand, the numerical methods can be used to solve time varying and non-linear equation systems (Clarke, 2001). In order to investigate the influence of the solar cells within the semi-transparent BIPV modules under the conditions which are time depending, numerical methods are more suitable for this study. Also, the numerical methods allow the determination of the temperatures within the elements, which is one of the major outputs of the current study. When comparing the finite difference method and the finite element method, the former is simpler to formulate a building heat transfer model. Therefore, the finite difference method is adopted in the current

study to solve the heat transfer equations.

The explicit finite difference approach is used because it has higher stability when applied in multi-layered construction. For the heat balance equation of the front-glass, i.e. equation (5.1a), by expressing the partial derivative in the equation in discrete form, the temperature at the *m*th node in the module with distance *Δx* between two nodes, i.e. at $x = (L2 - m \cdot \Delta x)/\cos\vartheta_2$, is,

$$\begin{aligned}(T_{fg})_m^{P+1} &= F_o\left[(T_{fg})_{m+1}^P + (T_{fg})_{m+1}^P\right] + (1-2F_o)(T_{fg})_m^P \\ &+ \left(\frac{\lambda_g \Delta t}{k_g}\right)\left[S_o \cdot K \cdot \exp\left(\frac{-K(L2 - m\cdot\Delta x)}{\cos\vartheta_2}\right)\right]\end{aligned} \tag{5.8}$$

where *P* denotes the time dependence of the glass temperature and the temperature at the next time step, *P*+1, is calculated using that of the current time *P*; *Δt* is the time interval for iteration; F_o is the Fourier number which can be expressed as $F_o = \lambda_g \cdot \Delta t / \Delta x^2$. F_o should be less than 0.5 for convergent iteration.

For the back-glass, similar expression can be obtained by the use of explicit finite different method. The energy equations for the "solar cell part" (equation (5.3)) and the "transparent part" (equation (5.5a)) can be solved separately. The solutions of the temperatures in the back-glass at those two parts can be written as follows,

<u>Solar cell part:</u>

$$(T_{bg})_m^{P+1} = F_o\left[(T_{bg})_{m+1}^P + (T_{bg})_{m+1}^P\right] + (1-2F_o)(T_{bg})_m^P \tag{5.9a}$$

<u>Transparent part:</u>

$$\begin{aligned}(T_{bg})_m^{P+1} &= F_o\left[(T_{bg})_{m+1}^P + (T_{bg})_{m+1}^P\right] + (1-2F_o)(T_{bg})_m^P \\ &+ \left(\frac{\lambda_g \Delta t}{k_g}\right)\left[S_o \cdot \tau_{fg} \cdot \tau_r \cdot K \cdot \exp\left(\frac{-K(L1 - m\cdot\Delta x)}{\cos\vartheta_2}\right)\right]\end{aligned} \tag{5.9b}$$

Since the thicknesses of the layer of the solar cell and the transparent material are

neglected, the temperatures at $x = L1$ with respect to the front-glass, the back-glass, the solar cell and the transparent material layer are the same, i.e.,

$$T_{bg}(L1,t) = T_{fg}(L1,t) = T_{cell}(L1,t) = T_r(L1,t) \tag{5.10}$$

where $T_{cell}(L1,t)$ and $T_r(L1,t)$ are the temperatures of the solar cell and the transparent material at $x = L1$ respectively. With equation (5.10), $T_{cell}(L1,t)$ and $T_r(L1,t)$ can be expressed by expanding equation (5.2a) and (5.4) respectively as follows,

$$\left(T_{cell}\right)_{L1}^{P+1} = \frac{1}{2}\left[\frac{\Delta x}{k_g}\cdot S_o \cdot \tau_{fg} \cdot (\alpha_{pv} - \eta_{pv}) + \left(T_{bg}\right)_{L1-1}^{P+1} + \left(T_{fg}\right)_{L1+1}^{P+1}\right] \tag{5.11a}$$

$$\left(T_r\right)_{L1}^{P+1} = \frac{1}{2}\left[\frac{\Delta x}{k_g}\cdot S_o \cdot \tau_{fg} \cdot \alpha_r + \left(T_{bg}\right)_{L1-1}^{P+1} + \left(T_{fg}\right)_{L1+1}^{P+1}\right] \tag{5.11b}$$

It is noted from equation (5.11a) and (5.11b) that the temperatures at the solar cell and the transparent material are obtained from the temperatures of the front-glass and the back-glass at the current time step (P+1) instead of the preceding time step (P). Therefore, prior to applying equation (5.11a) and (5.11b), the temperatures of the discrete nodes in the front-glass and the back-glass should be determined by equation (5.8), (5.9a) and (5.9b).

The boundary conditions can also be solved by the explicit approach. In order to determine the thermal conditions near the surface more accurately and allow the surface temperature to be evaluated directly, the surface node is assigned a thickness that is one-half of the interior nodes. The energy balance equations at the surface nodes are established where the sum of energy flows into the node and the energy generation in the node is equal to the increase of the internal energy of the node. For the “transparent part” of the semi-transparent BIPV modules, the governing equations on exterior and interior surfaces are, respectively,

Exterior surface (at $x = L2$):

$$\rho C \frac{\left(T_{fg}\right)_{L2}^{P+1} - \left(T_{fg}\right)_{L2}^{P}}{\Delta t} \cdot \frac{\Delta x}{2} = \frac{k_g}{\Delta x}\left[\left(T_{fg}\right)_{L2-1}^{P} - \left(T_{fg}\right)_{L2}^{P}\right] - h_o\left[\left(T_{fg}\right)_{L2}^{P} - T_o\right] - \sigma\xi_g\left\{\left[\left(T_{fg}\right)_{L2}^{P}\right]^4 - \left[\left(T_o\right)^P\right]^4\right\} + \frac{\Delta x}{2} \cdot \frac{dS_{fg}}{dx} \tag{5.12a}$$

Interior surface at ($x = 0$):

$$\rho C \frac{\left(T_{bg}\right)_{0}^{P+1} - \left(T_{bg}\right)_{0}^{P}}{\Delta t} \cdot \frac{\Delta x}{2} = \frac{k_g}{\Delta x}\left[\left(T_{bg}\right)_{1}^{P} - \left(T_{bg}\right)_{0}^{P}\right] - h_r\left[\left(T_{bg}\right)_{0}^{P} - T_i\right] - \sigma\xi_g\left\{\left[\left(T_{bg}\right)_{0}^{P}\right]^4 - \left[\left(T_i\right)^P\right]^4\right\} + \frac{\Delta x}{2} \cdot \frac{dS_{bg}}{dx} \tag{5.12b}$$

The governing equation of the exterior surface of the “solar cell part” is the same as that of the “transparent part”, i.e. equation (5.12a). However, equation (5.12b) is only applicable to the “transparent part”. The back-glass of the “solar cell part” receives no solar radiation, so, the last term in equation (5.12b), which represents the solar radiation absorbed, is absent for the interior surface of the “solar cell part”.

By re-arranging equation (5.12a) and (5.12b), the surface temperatures of the two sides at the next time step can be expressed as follows,

Exterior surface (at $x = L2$):

$$\begin{aligned}\left(T_{fg}\right)_{L2}^{P+1} &= 2F_o\left(T_{fg}\right)_{L2-1}^{P} + (1-2F_o)\left(T_{fg}\right)_{L2}^{P} \\ &+ \left(\frac{2\lambda_g \Delta t}{k_g \Delta x}\right)\left\{-h_o\left[\left(T_{fg}\right)_{L2}^{P} - \left(T_o\right)^p\right] - \sigma\xi_g\left[\left(\left(T_{fg}\right)_{L2}^{P}\right)^4 - \left(\left(T_o\right)^P\right)^4\right]\right\} \\ &+ \left(\frac{\lambda_g \Delta t}{k_g}\right)\left[S_o \cdot K \cdot \exp\left(\frac{-K(L2 - m \cdot \Delta x)}{\cos\theta_2}\right)\right]\end{aligned} \tag{5.12c}$$

Interior surface (at $x = 0$):

$$\begin{aligned}\left(T_{bg}\right)_0^{P+1} &= 2F_o\left(T_{bg}\right)_1^P + (1-2F_o)\left(T_{bg}\right)_0^P \\ &+ \left(\frac{2\lambda_g \Delta t}{k_g \Delta x}\right)\left\{-h_r\left[\left(T_{bg}\right)_0^P - \left(T_r\right)^P\right] - \sigma\xi_g\left[\left(\left(T_{bg}\right)_0^P\right)^4 - \left(\left(T_r\right)^P\right)^4\right]\right\} \\ &+ \left(\frac{\lambda_g \Delta t}{k_g}\right)\left[S_o \cdot \tau_{fg} \cdot \tau_r \cdot K \cdot \exp\left(\frac{-K(L1 - m \cdot \Delta x)}{\cos\theta_2}\right)\right]\end{aligned} \tag{5.12d}$$

Again, equation (5.12c) applies to both the "solar cell part" and the "transparent part". The last term in equation (5.12d) is excluded for the temperature at the interior surface node in the "solar cell part" because of the absence of solar radiation at the node.

The exterior and interior convective heat transfer coefficients h_o and h_r in equation (5.12a) to (5.12d) can be evaluated according to the values suggested by various guidelines such as those published by American Society of Heating, Refrigerating and Air-Conditioning Engineers (ASHRAE) and Chartered Institution of Building Services Engineers (CIBSE). In practical situations, these two coefficients are affected by the ambient environment such as airflow velocity (wind speed), surface temperature and room air temperature.

The value of h_o is dependent on the outdoor air velocity and the direction of wind relative to the surface. Loveday and Taki (1996) established the empirical relationship by conducting on-site experimental studies. Their suggested co-relations are as follows,

$$h_o = 2 \cdot v + 8.91 \quad \text{for windward condition} \tag{5.13a}$$

$$h_o = 1.77 \cdot v + 4.93 \quad \text{for leeward condition} \tag{5.13b}$$

where v is the wind speed in *m/s*. These co-relations are suitable for applications to

smooth-textured surfaces such as the BIPV modules in the current research. h_o can be estimated by the above expressions if the wind speed and direction are known. However, in certain applications, such as peak heat transfer estimations, the wind speed is not available and a constant value of h_o is used.

The interior convective heat transfer coefficient, h_r, can also be found from various handbooks (e.g. ASHRAE, 2001). a modification of the ASHRAE's equation was carried out by Curcija and Goss, 1995. They compiled and modified several studies on convective heat transfer coefficient of interior window surface. The relationship suggested by them is,

$$h_r = 1.46\left(\frac{\Delta T}{l}\right)^{0.25} \tag{5.14}$$

where ΔT is the temperature difference between the interior module surface and room air, and l is the module height.

Using the expressions of the convective heat transfer coefficients together with the equations of the boundary conditions, the exterior and interior surface temperatures of the module can be determined.

5.2.6 Initial conditions

As illustrated in section 5.2.5, the current temperature is necessary for calculating the temperature in the next time step, and iteration is required in order to determine the temperature after more time steps. A linear temperature distribution across the thickness of each element of the PV modules between the interior and exterior temperatures is assumed firstly. The linear temperature distribution are calculated as follows,

$$T(x,0) = \left(\frac{T_o - T_i}{L2} \right) x + T_i \tag{5.15}$$

where *T(x,0)* is the temperature at all *x* and when *t* = 0. However, the linear distribution is not true in the real situation. Therefore, the linear distribution is first input to the SPVHG model and iterated for three days to obtain the realistic initial conditions. The realistic initial conditions are then input to the first time step of the SPVHG model again to complete the simulation.

5.2.7 Optical properties of the glass layers

A number of studies have been carried out to prove the dependence of incident angle of solar radiation on the transmittance and reflectance of glass (Furler, 1991; Gueymard, 1989; Rubin et al., 1998). Since the incident angle of the solar radiation varies with time throughout a day, the optical properties also keep changing. As these optical properties will consequently affect the solar energy transmission, it is necessary to take into account the angular dependence of the optical properties of glass in the solar heat gain simulation.

When solar radiation is incident on a sheet of glass, part of the radiation is reflected from the exterior and interior surface, while part of it is absorbed by the glass material. After successive reflection, absorption and transmission, the quantity of radiation transmitted through the glass layer is given by the sum of infinite series. Let *r* be the fraction of each component reflected, and *a* be the fraction of each component available after absorption. The total transmissivity can be written as follows,

$$\tau(\theta_1) = \frac{(1-r^2)a}{1-r^2a^2} \tag{5.16}$$

By Fresnel relations, the refracted fraction, *r*, can be expressed as,

$$r = \frac{1}{2}\left[\frac{\sin^2(\theta_1-\theta_2)}{\sin^2(\theta_1+\theta_2)} + \frac{\tan^2(\theta_1-\theta_2)}{\tan^2(\theta_1+\theta_2)}\right] \tag{5.17}$$

where θ_1 and θ_2 are the incident and refraction angle as shown in Figure 5.4. θ_2 can be evaluated by Snell's law,

$$\theta_2 = \sin^{-1}\left(\frac{\sin\theta_1}{n_g}\right) \tag{5.18}$$

where n_g is the refractive index of the glass. The fraction after attenuation, *a*, in equation (5.14) is given by,

$$a = \exp\left(\frac{-K \cdot L2}{\cos\theta_2}\right) \tag{5.19}$$

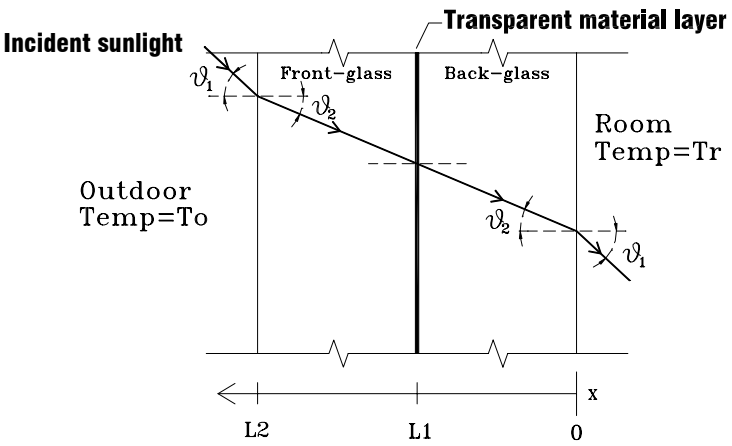

Figure 5.4 Angles of incident and refraction

The above analysis applies only to beam solar radiation. For the sky diffuse and ground reflected components of the solar radiation which are not directionally specific,

two effective incident angles, $\theta_{e,s}$ and $\theta_{e,g}$ were derived to represent the equivalent incident angle of the corresponding component respectively. Brandemuehl and Beckman (1980) have shown that the two effective incident angles are related to inclination β of the solar panel by the following equations,

$$\theta_{e,s} = 59.68 - 0.1388\beta + 0.001497\beta^2 \tag{5.20a}$$

$$\theta_{e,g} = 90 - 0.5788\beta + 0.002693\beta^2 \tag{5.20b}$$

With equations (5.16) to (5.20), the optical characteristics of the glass layers in terms of the incident angle of the solar radiation can be evaluated. Those characteristics can then be used with the energy equations as described in sections 5.2.2 to 5.2.5 for determining the temperature distribution across the BIPV module. Thus the amount of heat gain can be evaluated by using the temperatures.

5.2.8 Heat gain

Heat gain through the semi-transparent BIPV glazing can be evaluated by investigating the heat exchange between the interior surface of the module and the internal environment of the room. The heat transfer that takes place at the interior surface (the surface facing indoors) of the module includes the convective heat exchange between the surface and the indoor air, the radiant heat exchanges of the surface with other enclosing surfaces of the room, and the radiant heat transfer due to the solar radiation transmitted through the transparent part of the module. The formulations of the equations of each of the heat exchange process are described separately in sections 5.2.8.1 to 5.2.8.4.

5.2.8.1 Convective heat gain

The rate of convective heat transfer depends on the temperature difference between the surface and the ambient air, and the air flow rate along the surface. The rate of airflow along a building element is normally a combination of natural and forced convection. The rate of convective heat transfer on the interior surface of the semi-transparent module can be calculated by the following equation,

$$Q_{conv} = h_r \cdot \left[T_{bg}(0,t) - T_r \right] \qquad (\mathrm{W/m^2}) \tag{5.21}$$

where $T_{bg}(0,t)$ and T_r are the temperatures of the interior surface of the module and the indoor air respectively. $T_{bg}(0,t)$ can be obtained from equations of the interior boundary conditions as described in sections 5.2.4 and 5.2.5 for both the "solar cell part" and the "transparent part". The indoor air is assumed to be perfectly mixed so that the air in the room can be represented by a single air state. Therefore, it is assumed that T_r is constant and equal to the design indoor temperature of the air-conditioning system. h_r is the convective heat transfer coefficient on the interior surface of the module which can be obtained by equation (5.14).

5.2.8.2 Radiative heat exchange among room surfaces

Radiation heat exchange among room surfaces can be modeled by using the conventional radiation heat transfer network analysis method. However, this method results in a substantial burden to the simulation calculations. Several simiplified methods for calculating the radiation heat exchange among interior surfaces have been analyzed by Liesen and Pedersen (1997). They found that the mean radiant temperature (MRT) with balance method performs the best in terms of accuracy and

simplicity. In the MRT method, each surface is assumed to radiate heat only to a fictitious surface. The area ($A_{MRT,i}$), emissivity ($\varepsilon_{MRT,,i}$) and temperature ($T_{MRT,i}$) of the fictitious surface are obtained as weighted averages of all surfaces as follows,

$$A_{MRT,i} = \sum_{j=1}^{N} A_j \qquad \text{for } j \neq i \tag{5.22a}$$

$$\varepsilon_{MRT,i} = \sum_{j=1}^{N} \frac{A_j \varepsilon_j}{A_{MRT,i}} \qquad \text{for } j \neq i \tag{5.22b}$$

$$T_{MRT,i} = \sum_{j=1}^{N} \frac{A_j \varepsilon_j T_j}{A_{MRT,i} \varepsilon_{MRT,i}} \qquad \text{for } j \neq i \tag{5.22c}$$

The subscript i in the above three equations refers to the surface that is concerned (surface i), which is the interior surface of the semi-transparent BIPV module in the current study. The subscript j refers to the other surfaces other than surface i. In addition to the surface i, any surfaces facing the same direction as surface i are excluded from the calculation of the area, emissivity and temperature of the fictitious surface.

The view factor $F_{MRT,i}$ between the surface i and the fictitious surface can be formulated as follows,

$$F_{MRT,i} = \frac{1}{\dfrac{1-\varepsilon_i}{\varepsilon_i} + 1 + \dfrac{A_i\left(1-\varepsilon_{MRT,i}\right)}{A_{MRT,i}\varepsilon_{MRT,i}}} \tag{5.23}$$

The net heat gain per unit area of the module due to radiant heat exchange ($Q_{MRT,i}$) with other interior surfaces of the room can be evaluated by,

$$Q_{MRT,i} = \sigma F_{MRT,i}\left(T_i^{\,4} - T_{MRT,i}^{\,4}\right) \qquad (\text{W/m}^2) \tag{5.24}$$

The above MRT method will lead to net imbalance in the total radiant energy because of the approximation made in the calculation of view factors and mean

radiant temperature. The problem can be resolved by distributing the net imbalance equally on all surfaces to maintain the conservation of energy. The net imbalance can be evaluated by,

$$q_{Bal} = \frac{\sum_{i=1}^{N} \sigma A_i F_{MRT,i} \left[T_{MRT,i}{}^4 - T_{bg}(0,t)^4 \right]}{\sum_{i=1}^{N} A_i} \qquad (\mathrm{W/m^2}) \qquad (5.25)$$

With this correction included, $Q_{MRT,i}$ in equation (5.22) can be rewritten as,

$$Q_{MRT,I} = \sigma F_{MRT,i} \left[T_{bg}(0,t)^4 - T_{MRT,i}{}^4 \right] - q_{Bal} \qquad (\mathrm{W/m^2}) \qquad (5.26)$$

As the above equation involves fourth power terms, a further simplification can be used to linearize the calculation by the following approximation,

$$4T_{ave,i}{}^3 \left(T_i - T_{MRT,i} \right) \approx T_i{}^4 - T_{MRT,i}{}^4 \qquad (5.27)$$

where

$$T_{ave,i} = \frac{T_i + T_{MRT,i}}{2} \qquad (5.28)$$

As a result, the net heat gain per unit area of the module due to radiant heat exchange with other interior surfaces in the room is given by,

$$Q_{MRT,i} = 4\sigma F_{MRT,i} T_{ave,i}{}^3 \left(T_i - T_{MRT,i} \right) - q_{Bal} \qquad (\mathrm{W/m^2}) \qquad (5.29)$$

5.2.8.3 Solar heat gain

The heat gain term due to the instantaneous incident solar radiation appears only in the “transparent part” of the semi-transparent BIPV module. Since the solar radiation is attenuated by the glass and transparent material layers, the heat gain term can be determined by multiplying the solar irradiance on the module surface to the

transmittances of the glass and the transparent material layers as follows,

$$Q_{solar} = S_o \tau_{fg} \tau_{bg} \tau_r \qquad (\mathrm{W/m^2}) \tag{5.30}$$

5.2.8.4 Total heat gain

The procedure given in section 5.2.8.1 to 5.2.8.3 gives the heat gain amount per unit area of the semi-transparent BIPV module. By using the corresponding temperatures of the "solar cell part" and the "transparent part" of the BIPV module and the solar cell area ratio of the module, the heat gain from these two parts can be calculated separately by the above procedure. In order to distinguish the heat gain from the "solar cell part" and the "transparent part", the subscripts "*cell*" and "*trans*" are used. Let *R* be the portion of solar cell area per unit area of the module, the heat gains of the "solar cell part" due to convective and radiative heat exchange with the indoor air are,

$$(Q_{conv})_{cell} = Q_{conv} \cdot R \tag{5.31a}$$

$$(Q_{MRT})_{cell} = Q_{MRT} \cdot R \tag{5.31b}$$

The total heat gain at the "solar cell part" is the sum of equation (5.29a) and (5.29b),

$$(Q_{total})_{cell} = (Q_{conv})_{cell} + (Q_{MRT})_{cell} \tag{5.31c}$$

Similarly, the heat gains of the "transparent part" are,

$$(Q_{conv})_{trans} = Q_{conv} \cdot (1 - R) \tag{5.32a}$$

$$(Q_{MRT})_{trans} = Q_{MRT} \cdot (1 - R) \tag{5.32b}$$

$$(Q_{solar})_{trans} = Q_{solar} \cdot (1 - R) \tag{5.32c}$$

$$(Q_{total})_{trans} = (Q_{conv})_{trans} + (Q_{MRT})_{trans} + (Q_{solar})_{trans} \tag{5.32d}$$

As a result, the total heat gain of the semi-transparent BIPV module per unit area

can be evaluated by combining equation (5.31c) and (5.32d),

$$Q_{total} = (Q_{total})_{cell} + (Q_{total})_{trans} \tag{5.33}$$

Using the above modeling method, the heat gain through the semi-transparent BIPV module can be evaluated. A Visual C++ computer program has been developed to facilitate the calculations. The program first incorporates equation (5.13) to determine the initial temperature of each node in the module. The temperature of the next time step can then be iterated according to equation (5.8) to (5.12d) by considering also the glass optical properties as stated in equation (5.16) to (5.20b). The heat flux to the indoor air can then be evaluated using the interior surface temperature of the module. A separate sub-routine for calculating the solar radiation on a tilted surface of any orientation using the approach described in Chapter 4 is included in the program. Therefore, the program is applicable to PV modules of any inclination and orientation.

5.3 SUMMARY

The SPVHG model has been developed in this chapter to calculate the amount of heat gain through the semi-transparent BIPV modules under the unsteady ambient conditions. One-dimensional transient energy equations have been established for each layer of the “solar cell part” and the “transparent part” of the module. The initial and boundary conditions have been set up for applications in buildings. The variation of the optical properties of the glass layers due to the solar incident angle has been

taken into account in the model.

A numerical method has been used to solve the energy equations. The explicit finite difference method has been adopted to solve the transient equations. The temperature distribution across the module can then be determined after solving those equations. Subsequently, the heat flux through the “solar cell part” and the “transparent part” of the module are calculated separately by using the corresponding interior surface temperature of the individual part. A Visual C++ program has been written for the model.

The SPVHG model developed in this chapter is a useful tool for assessing the thermal performance of the semi-transparent BIPV modules. The heat transfer behavior of the PV modules with different thicknesses and solar cell area ratios can be understood by using the model. Simulation results according to the SPVHG model are presented in Chapter 9 to illustrate the applications of the model and the energy performance of different kinds of semi-transparent BIPV modules.

CHAPTER 6

POWER GENERATION MODEL OF PV MODULES AND ON-SITE MEASUREMENT

One of the benefits of the BIPV systems is their power generation. Modeling the amount of power produced by the systems is a vital part of the energy performance assessment of the systems. In this chapter, the power generation models of both opaque type and semi-transparent type PV modules are described. As these two types of PV modules have different usage and structure, the power generation models of them are described separately. The fundamental voltage and current characteristics of solar cells are described firstly as the basis of the power generation models. A simplified model for opaque PV modules is then derived based on an existing power generation model. The model takes many parameters into account, such as the level of solar radiation, solar cell's temperature and electrical parameters of the PV modules. The model was validated by measured data from an operating BIPV system in Hong Kong. Another power generation model for semi-transparent PV modules is also introduced. The two power generation models will be combined with the SPVHG model to evaluate the energy benefit of a PV façade.

6.1 BACKGROUND

In the design of a photovoltaic system, it is necessary to predict the potential power output of solar cells or PV modules under various conditions. The power output of solar cells or PV modules can be evaluated by plotting the current-voltage (I-V) characteristics curve under their actual operating conditions. This I-V curve can be plotted by using relevant simulation models and electrical specifications of the modules at standard test conditions (STC). A number of power output models have been developed in the last two decades (e.g. Overstraeten and Mertens, 1986; Lasnier and Ang, 1990; Hamdy, 1994; Akbaba and Alattawi, 1995). Some of the models simulate the power output starting from the basic principle while some models aim at inputting the minimum information but maintaining acceptable accuracy.

Overstraeten and Mertens (1986) first represented the power generating principle of a solar cell by an equivalent diode model, which formed the basis of further studies. Simplified models have also been developed by various researchers such as Evans (1981), Meyer and Dyk (2000), Jones and Underwood (2002), Ahmad et al. (2003) and Lu (2004). The simplified models require only the input of solar irradiation, ambient temperature and the limited electrical parameters of the PV module. This information is readily available, the simplified models are therefore convenient to use and are usually adopted for practical applications.

In this chapter, a simplified power generation model for the opaque PV modules is described. On-site measurements were also carried out to verify the accuracy of the model. The model was then modified by incorporating the results of the on-site measurements so that the model is applicable to the Hong Kong situation.

The existing power generation models for opaque PV modules require the input of electrical parameter of the module. In practical applications, the semi-transparent BIPV modules are usually tailor made for each particular project. The size and the number of solar cells used in the semi-transparent module are different from case to case. Thus, the electrical characteristics are not standardized and not available in most of the cases. Therefore, the existing power generation models are not suitable for semi-transparent BIPV modules. In addition to the simplified power generation model for the opaque PV modules, another approach for estimating the power produced by the semi-transparent BIPV modules is also introduced in this chapter.

6.2 POWER GENERATION OF OPAQUE PV MODULES

6.2.1 Diode model

Solar cells can be represented by a well-known diode model. In the model, the solar cell is modeled as a current source, connected in parallel with two diodes, a parallel cell resistance and another series resistance. Figure 6.1 illustrates the equivalent circuit of the diode model. The current-voltage characteristic of the model can be written as,

$$I = I_L - I_0\left[\exp\left(\frac{V + R_s I}{V_t}\right) - 1\right] - I_{0m}\left[\exp\left(\frac{V + R_s I}{mV_t}\right) - 1\right] - \frac{V + R_s I}{R_p} \tag{6.1}$$

where I is the current generated by the solar cell; I_L is the light-generated current; I_0 is

the reverse saturation current of the ideal diode; V is the voltage generated by the solar cell; R_s is the series resistance of the solar cell; V_t is the thermal voltage depending on the cell temperature T_{cell}, defined as $V_t = kT_{cell} / q$; I_{0m} is the reverse saturation current of the non-ideal diode and R_p is the shunt resistance.

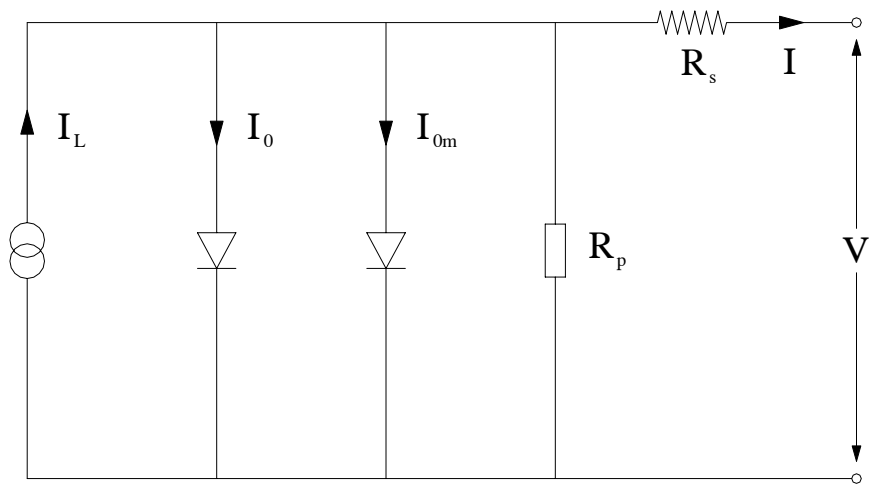

Figure 6.1 Equivalent circuit of a solar cell

For an ideal case, i.e. I_{0m} = 0, R_s = 0 and R_p = ∞ (Qverstraeten and Mertens, 1986), equation (6.1) can be simplified as,

$$I = I_L - I_0 \left[\exp\left(\frac{V + R_s I}{V_t} \right) - 1 \right] \tag{6.2}$$

In addition, the light-generated current is proportional to the solar irradiance on the cell surface (Lasnier and Ang, 1990),

$$I_L = K \cdot S \tag{6.3}$$

where K is a constant and S is the solar irradiance in W/m^2. According to Lasnier and Ang (1990), the reverse saturated current of the diode can be expressd as a function of the cell temperature,

$$I_0 = C_0 T_{cell}^3 \exp\left(-\frac{E_G}{n_{ideality} k_B T_{cell}}\right) \tag{6.4}$$

where C_0 is the saturation current temperature coefficient; E_G is the energy gap in eV; $n_{ideality}$ is the ideality factor and k_B is the Bolzmann's constant in eV/K. For a silicon device, according to Hovel (1975), the saturation current density (i.e. $I_0 / \text{cell area}$) is 10^{-12} A/cm^2.

6.2.2 Short circuit current and open circuit voltage

Figure 6.2 illustrates a typical current (I)-voltage (V) curve of a solar cell. The curve shows the relationships between the current and voltage generated by a solar cell. The important parameters of a solar cell, such as short circuit current (I_{sc}), open circuit voltage (V_{oc}) and maximum power point (P_{max}) are also indicated in the curve.

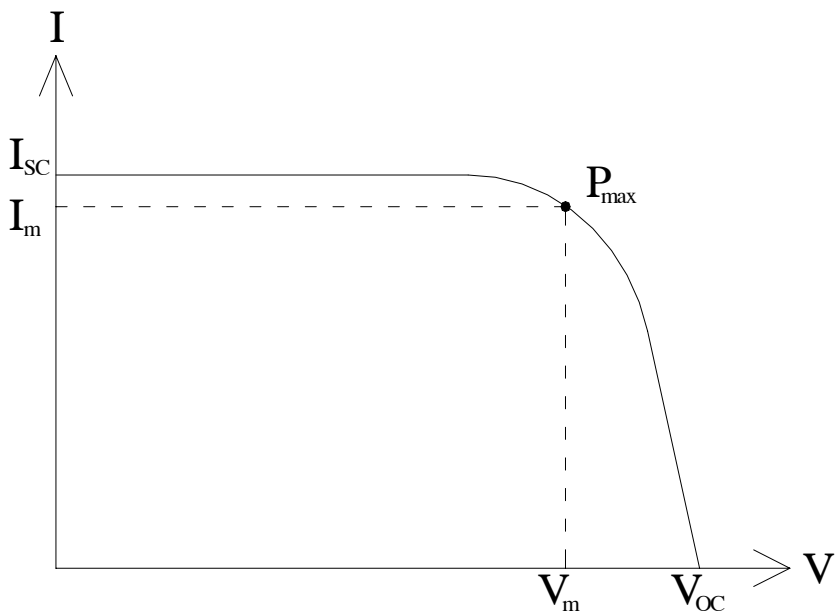

Figure 6.2 I-V curve of a solar cell

In normal situations, the series resistance R_s can be neglected in the short-circuit condition. Then, the short circuit current I_{sc} is equal to the light-generated current I_L, which is proportional to the solar irradiance on the cell surface. Therefore I_{sc} is also proportional to the irradiance, i.e. $I_{sc} \propto S$.

The dependence of temperature of solar cell current is much smaller than that of solar cell voltage (Markvart, 2000). Therefore, for the purpose of module modeling, a constant short circuit current can be assumed with change in module temperature. At an average irradiance level, the diode current and the resistance terms are negligible. The relationship of open circuit voltage and the solar irradiance can be written as follows,

$$V_{oc} \propto \ln\left(\frac{K \cdot S}{I_0}\right) \tag{6.5}$$

As the saturated current increases exponentially with the cell temperature as shown equation (6.4), the open circuit voltage will decrease linearly with increasing cell temperature (Lasnier and Ang, 1990),

$$V_{oc} \propto \frac{1}{T_{cell}} \tag{6.6}$$

6.2.3 Power generation of PV modules

The maximum power point in the I-V curve of a PV module is the point at which the product of I and V is the maximum. The current and voltage that lead to the maximum power point are denoted as I_m and V_m respectively as shown in Figure 6.2. The maximum power can also be determined by the short circuit current and open

circuit voltage by defining a term called fill factor (*FF*). Fill factor is defined as the ratio of the actual maximum power to the theoretical maximum power that results as the product of short circuit current and open circuit voltage. It can be expressed as follows,

$$FF = \frac{I_m \times V_m}{I_{sc} \times V_{oc}} = \frac{P_{\max}}{I_{sc} \times V_{oc}} \tag{6.7}$$

By re-arranging equation (6.7), the maximum power can be given by,

$$P_{\max} = FF \times I_{sc} \times V_{oc} \tag{6.8}$$

According to Jones and Underwood (2002), by using the relationship of I_{sc} and V_{oc} with irradiance and module temperature and equation (6.8), the maximum power generation of PV array is given by,

$$P_{sim} = \left[FF \cdot \left(I_{sc0} \cdot \frac{S}{S_0} \right) \cdot \left(V_{oc0} \cdot \frac{\ln(k_1 \cdot S)}{\ln(k_1 \cdot S_0)} \cdot \frac{T_0}{T_{cell}} \right) \cdot N_m \right] \tag{6.9}$$

where I_{sc0}, V_{oc0}, S_0, and T_0 are the short circuit current, open circuit voltage, irradiance and module temperature under standard test condition respectively;

k_1 is a constant, $k_1 = \frac{K}{I_0}$ and K = 0.005 A/W/m^2 (Jones and Underwood, 2002) and I_0 = cell area x 10^{-12} A/cm^2; N_m is the number of module in the array. This model has been verified for UK conditions by Jones and Underwood (2002). When it is used for Hong Kong conditions, modification is required. A comparison of the simulated power outputs (results of equation (6.9)) and the measured data taken in Hong Kong was carried out by first-order linear regression fits of the scatter plot of simulated against measured data. A linear relationship between the two sets of data has been found. According to the relationship found, the simulated power outputs can be

corrected according to the follow equation to obtain the actual values. $P_{max,\,corr}$ is the corrected power outputs.

$$P_{sim,corr} = \left\{ \left[FF \cdot \left(I_{sc0} \cdot \frac{S}{S_0} \right) \cdot \left(V_{oc0} \cdot \frac{\ln(k_1 \cdot S)}{\ln(k_1 \cdot S_0)} \cdot \frac{T_0}{T_{cell}} \right) \cdot N_m \right] + A \right\} \times B \qquad (6.10)$$

The details for evaluating the two coefficients A and B will be described in section 6.3. Equation (6.10) can be used to estimate the DC power generated from opaque PV modules. AC power yielded can also be determined by simply multiply the inverter efficiency to the equation. This model takes the assumption that the fill factor remains unchanged over all operational values of solar irradiance and temperature. Although the solar cell temperature, T_{cell}, is usually not readily available in practical applications, it can be evaluated from ambient air temperature, T_a by the following correlation (Markvart, 2000),

$$T_{cell} = \frac{NOCT - 20}{0.8} \cdot S + T_a \qquad (6.11)$$

where *NOCT* is the Normal Operating Cell Temperature and is defined as the cell temperature when the PV module is operating under a specific condition, which is usually specified in manufacturer's data, 47 ºC in this study.

By using the model described above, the power generation of an opaque PV module can be easily determined by the knowledge of solar irradiance and ambient air temperature. These two parameters can be easily obtained from the meteorological records of the local observatory.

6.3 VERIFICATION OF POWER GENERATION MODEL

The previous section outlines the principles of the power generation model. In order to examine the accuracy of the simulation model, on-site measurements were carried out to obtain real performance data from a BIPV system. The BIPV system for these measurements is located at The Hong Kong Polytechnic University. A comparison is made between the measured data and the simulated data. It was found that modification to the simulation model is required. The coefficients of modification on the model are derived from this experimental study. A case study is also presented to demonstrate the application of the model in a real system.

6.3.1 Test set-up

The experimental data was collected from the BIPV system located on the roof of the Shaw amenities building at the Hong Kong Polytechnic University. The BIPV system comprises 98 mono-crystalline PV modules. 20 of these modules face east, 22 modules face south, 18 modules face west and 38 modules are mounted on the roof at a 23° inclination toward the south. The total rated power of the system is 7.8 kW, with DC output voltage between 75 V and 105 V, while AC output voltage of the system is 220 V. The photos of the system are shown in Figures 6.3 and 6.4. Figure 6.5 shows the electrical schematic diagram of the BIPV system.

The voltage and current generated by the BIPV system were recorded. Therefore, the DC power from the system can be calculated by the product of the voltage and current. A number of T-type thermocouples were attached on the surface of the PV

modules at each orientation to obtain the modules' operating temperatures. Ambient air temperature was also measured by another T-type thermocouple mounted next to the PV modules. All the thermocouple probes were covered by an aluminium foil to eliminate the influence of radiation absorption from the solar radiation. Global solar irradiance was measured by a Kipp & Zonen CM11 pyranometer. All the data were logged at five-minute intervals between mid June and mid July of 2003. Sunny and overcast sky conditions were also included during this period.

Figure 6.3 Exterior view of the BIPV system at the Hong Kong Polytechnic University

Figure 6.4 The control equipment of the BIPV system in the Hong Kong Polytechnic University

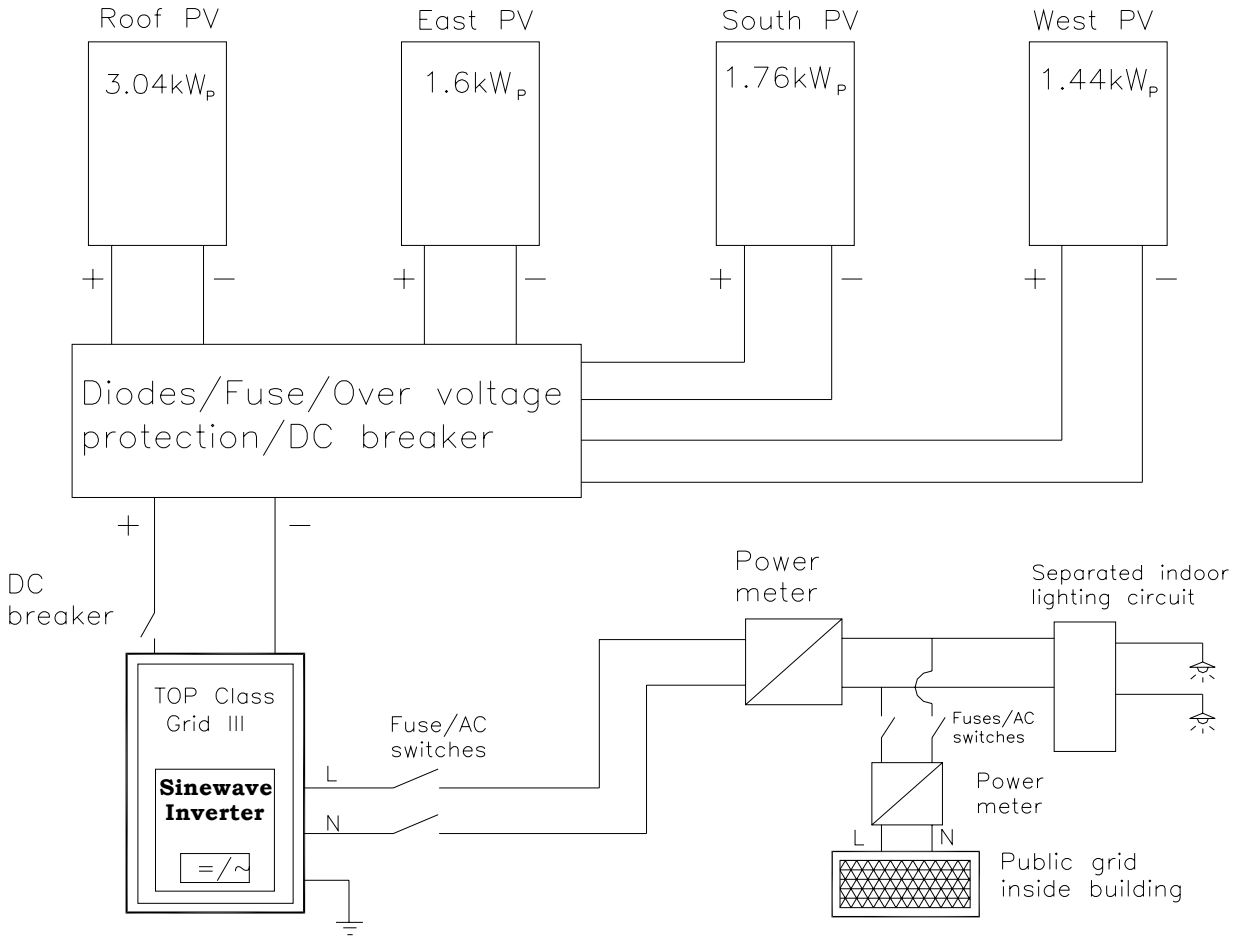

Figure 6.5 Schematic diagram of the BIPV system

The PV modules used in experiment are manufactured by BP Solar. The rated peak power of each module is $80W_p$. The detailed specifications of this PV module are shown in Table 6.1.

Table 6.1 Specification of the PV module used in the experiment

Solar cell type:	Mono-crystalline
Model no.:	BP 280F
Maximum power (P_{max}):	$80W_p$
Peak power voltage (V_m):	17V
Peak power current (I_m):	4.7A
Open circuit voltage (V_{oc0}):	21.8V
Short circuit current (I_{sc0}):	5A
Fill factor (FF):	0.734

6.3.2 Results of validation

By substituting the above electrical parameters, also the solar irradiation measured at each orientation as well as the solar cell temperature into equation (6.9), the power output of the BIPV system is resulted, which are denoted as P_{sim}. In the verification of the power generation model, the inverter efficiency term was omitted, and therefore DC power output was compared. For generalization, both measured and simulated power were reduced to unit area value for comparison.

The results calculated from equation (6.9) (P_{sim}) were plotted against the power output measured from the experiment, which are denoted as P_{mea}. The simulation results and the measured values obtained from the three orientations (south, west and

roof) were plotted in Figure 6.6. The results from the east façade were excluded because the PV modules on this direction are shaded by a nearby tall building in the morning, whose outputs are not reliable.

A clustered band of linear relationship can be clearly identified in the figures. A first-order linear regression equation was fit to the scatter plot of each orientation. The measured power should be equal to the simulated power after it had been corrected. Therefore, by substituting P_{sim} and P_{mea} into equation (6.10), the equation can be written as,

$$P_{mea} = (P_{sim} + A) \times B \tag{6.12a}$$

Re-arranging the equation can yield,

$$P_{sim} = \left(\frac{1}{B}\right) \times P_{mea} - A \tag{6.12b}$$

In the scatter plots as shown in Figure 6.6 to 6.9, the measured power P_{mea} is the x-axis and the simulated power P_{sim} is the y-axis. Therefore, the constant A and B can be evaluated by comparing equation (6.12b) with the regression equations of the scatter plots for each orientation. The values of A and B for each orientation are summarized in Table 6.2.

Table 6.2 Values of the correction coefficients of the power generation model

	A	**B**
Value	0.9	0.684

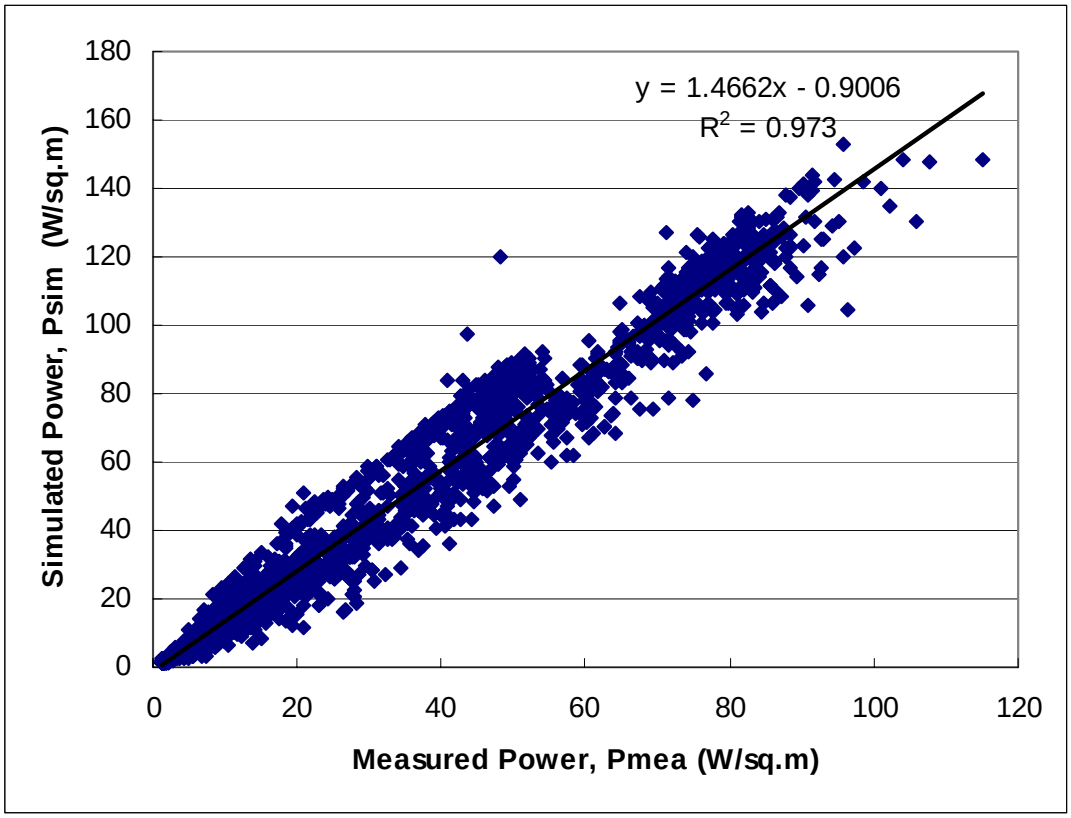

Figure 6.6 Correlation of simulated and measured power output

As shown in Figure 6.6, the simulated values obtained from Jones and Underwood's model (equation 6.9) have a clear linear relationship with the measured values, and only a minor modification on model is required according to the linear regression equation shown in Figure 6.6. The modified PV power generation model is applicable to local cases because it is established by incorporating the local measured data. Building designer can predict the power output of BIPV systems with different inclination, orientation and power capacity of the system by using the model. The input of the model is readily available and the calculation procedure is relatively strict forward. Therefore, the model is easy to use for general design applications. This is one of a significant contribution of this thesis.

6.4 POWER GENERATION OF SEMI-TRANSPARENT PV MODULES

In practical applications, the size and the number of solar cells in the opaque type BIPV modules are standardized by the module's manufacturers. However, the manufacturers only provide a limited range of module sizes. In contrast, much more flexibility can be allowed in semi-transparent BIPV modules. Since semi-transparent modules are usually integrated into building façades and atriums to replace traditional glazing, the size of each module and the solar cell packing are custom-made to satisfy the architectural requirements of individual buildings. The designs of the modules are different in each case, so that the electrical parameters of the semi-transparent modules are not specified by the manufacturer. We are not able to evaluate the power output of this kind of PV module by using the electrical parameters of the solar cells. The power generation model that was described in section 6.2 is not applicable to the semi-transparent BIPV modules. A more generic approach is required. This generic approach is outlined in this section which starts with the solar radiation reaching the solar cells.

Solar energy absorbed by the solar cells will be converted to heat and electricity by the cells. The amount of electricity produced by the cells depends on their power conversion efficiency. In addition, the amount of solar energy that reaches the cells' surface and the amount of energy absorbed by the solar cells are also the critical factors that affect the power generation of the solar cell. The concept of estimating the electricity output by considering the solar energy absorbed by the solar cell surface has been applied in PV/thermal collectors for two decades (Cox and Raghuraman,

1985; Zondag et al., 2003). Application of this concept in semi-transparent BIPV modules has also been introduced in recent years. Miyazaki et al. (2005) used this method to calculate the electricity output from the “see-through” type amorphous silicon PV modules. This method has been widely used in non-standard type PV modules. It is also applicable to the semi-transparent BIPV modules in the current study.

The power output from the semi-transparent BIPV module per unit module area can be calculated from the following parameters: solar cell efficiency under standard test condition η_{STC}, cover glass layer transmittance τ_{fg}, solar cell absorptance α_{cell}, solar cell area ratio R, and cell temperature T_{cell} and the solar irradiation on the module surface E. In mathematical form, the electricity output, P_{semi}, can be expressed as,

$$P_{semi} = S \cdot \eta_{STC} \cdot \tau_{fg} \cdot \alpha_{cell} \cdot R \tag{6.13}$$

The solar cell efficiency, η_{STC}, depends on the solar cell material. The efficiency of mono-crystalline silicon solar cells is around 14% to 18%, while that of poly-crystalline silicon is 13% to 16%. (Sonnenenergie, 2005). τ_{fg} is angular dependent. The details on evaluation of these two values are discussed in Chapter 5. The solar cell absorptance depends on the absorptivity characteristics of the solar cell material. For silicon, around 77% of solar irradiance photons are of the proper energy range to be absorbed by the solar cell (Merrigan, 1975).

In fact, equation (6.13) does not represent the real operating situation. This is because the solar cell efficiency is a function of cell temperature. Under operating conditions, the efficiency deviates from the value at standard test condition and falls

with increasing temperature. Therefore, crystalline silicon solar cells have greater efficiency at lower temperatures. Since the efficiency changes linearly with temperature, a temperature coefficient, β, is defined to describe the relationship. The value of the temperature coefficient is approximately -0.45% per $^{\circ}$C, and the solar cell efficiency can be corrected by the following equation (Zondag et al., 2003; Sonnenenergie, 2005),

$$\eta = \eta_{STC} \cdot [1 - 0.0045(T_{cell} - 25)] \tag{6.14}$$

where T_{cell} is the solar cell temperature under operating condition which can be determined by equation (6.11).

Equation (6.13) can be further modified by considering the consecutive reflection of sunlight within the cover-glass of the module. According to Duffie and Beckman (1980), the incident solar energy that is ultimately absorbed by the absorbing surface underneath the cover glass is approximately equal to 1.01 times the product of the transmittance of the glass and the absorptance of the surface. Hence, by incorporating equation (6.14), equation (6.13) can be modified into,

$$P_{semi} = 1.01 \cdot S \cdot \eta_{STC} \cdot [1 - 0.0045(T_{cell} - 25)] \cdot \tau_{fg} \cdot \alpha_{cell} \cdot R \tag{6.15}$$

By using equation (6.15), electricity output from a semi-transparent BIPV module can be evaluated if the relevant characteristics of the solar cells and the cover glass are known.

6.5 SUMMARY

In this chapter, the power generation model of the opaque type BIPV modules has been described. The simplified model developed by Jones and Underwood (2002) was adopted in this study. The model has been validated by experimental data, which shows that it is able to simulate the power output accurately, with only minor modifications needed to suit the local conditions.

As the number of solar cell in semi-transparent BIPV modules is not standardized, the electrical parameters of the modules are generally not available. Therefore, a simplified power generation model for the semi-transparent BIPV modules has to be adopted. The model is based on the relationship between the solar energy absorbed by the solar cells, the electricity conversion efficiency of the solar cells and the optical characteristics of the module cover glass. The model has been adopted and proven to be reliable by various researchers in different applications such as PV-thermal collectors and semi-transparent BIPV modules.

The amount of power output from the BIPV modules is a crucial part of their energy benefits. By using the power generation models described in this chapter, the power output from different applications and layouts of BIPV modules can be estimated. By using the power generation models in conjunction with the SPVHG model, the resultant energy benefit of the BIPV modules can be determined.

CHAPTER 7

INDOOR DAYLIGHT ILLUMINANCE MODELING

The use of semi-transparent BIPV modules to replace traditional glazing can reduce the amount of solar heat entering the building as well as generate electricity for the building. However, the indoor daylight level is also reduced at the same time due to the presence of opaque solar cells within the modules. As a result, the energy consumption of artificial lighting will be increased. In order to assess the resultant energy performance of the semi-transparent BIPV modules, a method for evaluating the effects on the indoor daylight level and energy consumption of artificial lightings due to the modules is necessary. This chapter develops a method for estimating the average indoor daylight illuminance for different transparent areas of the BIPV glazing. This method is intended for manual calculations or for implementation in a computer spreadsheet. Although the method is for manual calculations, it is detailed enough to take all sky conditions into account including overcast sky, partly cloudy sky and clear sky. In addition, the light reflected from the ground and opposite facades are also considered in the method.

7.1 REVIEW OF COMMON METHODS FOR INDOOR DAYLIGHT CALCULATIONS

Methods of modeling the indoor daylight level have been investigated for a number of decades. A common approach to make daylight calculations is to use a lumen method which is simple enough to allow manual calculations. In the lumen method for sidelighting, the interior horizontal illuminance E_i is calculated from the exterior vertical illuminance E_{xv}, the net transmittance of the window τ_w and a coefficient of utilization *CU*. The coefficient of utilization *CU* is the ratio of interior to exterior horizontal illuminances. It gives the interior illuminance at five predetermined points and is determined from a table of coefficients for different room geometries and sky conditions (IESNA, 2000). The interior horizontal illuminace E_i can be written as:

$$E_i = E_{xv} \tau_w CU \tag{7.1}$$

Although the lumen method is straight forward and easy to use, the major drawback of this method is that it assumes a simplified room geometry where the window extends along the entire window wall from the working plane to the ceiling cavity (Saraiji and Mistrick, 1993). The tabulated *CU* values are based on measured average illuminances. Also, the lumen method does not consider the direct sunlight entering the room space (Vartiainen, 2000).

Another simple daylight calculation method is the daylight factor method. This method determines the interior daylight illuminance by using a daylight factor *DF*, which is the ratio of the indoor daylight illuminance E_i to the simultaneous outdoor horizontal illuminance E_o under an unobstructed overcast sky. This method is

generally used with uniform or CIE (Commission Internationale de'lEclairage, or International Commission on Illumination in English) overcast skies (IESNA, 2000). The daylight factor *DF* is defined as:

$$DF = \frac{E_i}{E_o} \times 100\% \tag{7.2}$$

Although the daylight factor method is able to determine the illuminance at any point in an interior space produced by a sky with a known luminance distribution, the precision of the method is low (IESNA, 2000). Another limitation of the daylight factor method is that the CIE overcast sky underestimates the actual horizontal illuminances, leading to 100% discrepancies between the simulated and measured values (Reinhart and Herkel, 2000). Also, same as the lumen method, the daylight factor method excludes the direct sunlight.

For detailed daylight calculations, there are also a number of simulation tools which can handle more complex room geometries and sky conditions than the simple daylight factor and lumen methods. Two of the most sophisticated simulation models are Superlite and Radiance (Vartiainen, 2000). Although, with these simulation tools, it is possible to model very complex room geometries and also to visualize the interior illuminance distribution, these models involve great deal of computing time. The simulation of all hours in one year would take several days with these complex models (Vartiainen, 2000). However, the simpler and less time-consuming models are only applicable to limited sky conditions and do not give sufficiently accurate results. Therefore, a relatively simple and sufficiently accurate approach to interior daylight calculations is needed.

7.2 INDOOR DAYLIGHT ILLUMINANCE MODEL

The objective of this thesis is not to develop a new indoor daylight illuminance model. The principle of daylight modeling will not be investigated in detail. However, an indoor daylight illuminance model is required as a part of the evaluation of the energy performance of the semi-transparent BIPV modules. An indoor daylight illuminance model has been developed for the current study. This model is simple enough to allow manual calculations or for implementation in a computer spreadsheet. Despite its simplicity, this model takes different sky conditions into account and therefore has more flexibility of daylight modeling compared with the simple lumen and daylight factor methods. Also, the computing time of this method is much less than the complex simulation tools as mentioned in the previous section.

The calculations of interior daylight illuminance involve several steps. First of all, the exterior horizontal illuminances have to be evaluated by determining the sky conditions and sun's position. The illuminances on vertical facades can then be evaluated by the horizontal illuminances for an unobstructed sky. Since the light reflected from the ground and opposite building facades are important sources of interior lighting, the light originating from these two sources is also calculated. Lastly, the average interior illuminance on the working plane can be determined by combining all the components. The detailed procedure is described in sections 7.2.1 to 7.2.3.

7.2.1 Daylight availability

The amount of light from the sun and the sky for a specific time, date and sky condition at a specific location is referred to as "daylight availability", which varies with time according to the position of the sun. The position of the sun can be specified by a series of angles, namely solar declination δ, solar altitude α_s and solar azimuth γ_s. The solar declination has been mentioned in section 4.2.1. The solar altitude refers to the angle between the sun's ray and the horizontal plane. The solar altitude can be given by,

$$\sin\alpha_s = \cos\phi\cos\delta\cos\omega + \sin\phi\sin\delta \tag{7.3}$$

where ϕ is the local latitude and ω is the hour angle. These two angles have also been defined in section 4.2.1. The solar azimuth is the angular displacement from south of the projection of beam radiation on the horizontal plane. It can be calculated as follows (Diasty, 1998),

$$\gamma_s = \arcsin\left(\frac{\cos\delta\sin\omega}{\cos\alpha_s}\right) \tag{7.4}$$

During a longer day in a year (N.B. daytime is longer than 12 hours), the solar azimuth is expected to exceed $\pm 90^\circ$. In such a case, the following criterion needs to be satisfied in order to ensure that the azimuth angle is less than 90°,

$$\cos\omega > \frac{\tan\delta}{\tan\phi} \tag{7.5}$$

If the above criterion is not satisfied, the solar azimuth becomes,

$$\gamma_s = 180 - \arcsin\left(\frac{\cos\delta\sin\omega}{\cos\alpha_s}\right) \tag{7.6}$$

After determining the position of the sun, the illuminance of the direct sunlight can be quantified. Prior to calculating the illuminance of direct sunlight reaching the horizontal ground, the extraterrestrial solar illuminance E_{xt} has to be determined. The extraterrestrial solar illuminance is the illuminance on the surface perpendicular to the direction of propagation of the sunlight outside the atmosphere (Duffie and Beckman, 1980). In the calculation of the extraterrestrial solar illuminance, variation of the earth-sun distance should be taken into account because it may lead to variation of extraterrestrial radiation flux in the range of ±3% (Duffie and Beckman, 1980). The corrected extraterrestrial solar illuminance on the *n*th day of the year is,

$$E_{xt} = E_{sc}\left(1 + 0.033\cos\frac{360n}{365}\right) \tag{7.7}$$

where E_{sc} is the extraterrestrial solar illuminance measured at the earth's mean distance from the sun.

The direct normal illuminance at sea level E_{dn}, corrected for the attenuating effects of the atmosphere, can be estimated from the extraterrestrial solar illuminance, the optical atmospheric extinction coefficient c and the relative optical air mass m. E_{dn} can be expressed as,

$$E_{dn} = E_{xt}[\exp(-cm)] \tag{7.8}$$

The optical atmospheric extinction coefficient c depends on the sky conditions. The values of c under different sky conditions are presented in Table 7.1. The relative optical air mass m describes the ratio of the mass of atmosphere through which beam radiation passes to the mass if the sun were at the zenith (i.e. directly overhead). m can be approximated by,

$$m = \frac{1}{\cos \vartheta_z} \tag{7.9}$$

where θ_z is the zenith angle of the sun as defined in section 4.2.1.

The illuminance on a horizontal plane from the direct sun E_{dh} can then be estimated from the direct normal illuminance as follows,

$$E_{dh} = E_{dn} \sin \alpha_s \tag{7.10}$$

In addition to direct sunlight, diffuse light from the sky is another vital component of the total horizontal illuminance. The level of sky diffuse light depends on the sky conditions. In order to classify the sky conditions, the sky cover method is used to estimate the amount of cloud cover from totally no cloud (0.0) to completely overcast (1.0). The cloud cover values of different sky conditions are shown in Table 7.1.

The total horizontal illuminance due to diffuse skylight E_{kh} can be expressed as a function of the solar altitude as follows (IESNA, 2000),

$$E_{kh} = A + B \sin^C \alpha_s \tag{7.11}$$

where A, B and C are three constants that depend on different sky conditions. They are also shown in Table 7.1.

Table 7.1 Constants for calculating daylight availability

Cloud cover	**Sky conditions**	**c [used in eqt. (6.8)]**	**A (lux)**	**B (lux)**	**C [used in eqt. (6.11)]**
0 to 0.3	Clear	0.21	800	15500	0.5
0.4 to 0.7	Partly cloudy	0.8	300	45000	1
0.8 to 1	Cloudy	N/A	300	21000	1

This section has described the procedure for determining the daylight availability under an unobstructed sky. In reality, especially in a densely populated city like Hong Kong, light reflected from the opposite facades and the ground can be important sources of interior lighting. The following section will discuss the method for evaluating the daylight components under an obstructed sky.

7.2.2 Daylight of the obstructed sky

7.2.2.1 Sun and sky illuminance on the ground

The light that reflected from the ground eventually contributes to the illuminances of the room surfaces and the working planes. This section focuses on the daylight received on the ground. A horizontal ground can receive both direct sunlight and diffuse skylight if there is no obstacle. However, surrounding buildings may shade the ground from direct sunlight and partly obscure the view of the diffuse sky. Under an obstructed sky, one can determine whether the ground receives direct sunlight by the following equation. The ground is partly sunlit when,

$$h\frac{\cos|\gamma-\gamma_s|}{\tan\alpha_s}<w \tag{7.12}$$

where h is the height of the opposite building, w is the width of the street between the two buildings, and γ is the surface azimuth angle. The fraction of the ground that is sunlit, ρ_{sg}, can be calculated by another equation as follows,

$$\rho_{sg}=1-h\frac{\cos|\gamma-\gamma_s|}{w\tan\alpha_s} \tag{7.13}$$

An estimation of the mean ground illuminance E_g can be expressed in terms of the

horizontal illuminance due to the sky and the direct radiation as,

$$E_g = E_{kh} + \rho_{sg} E_{dh} \tag{7.14}$$

E_{dh} and E_{kh} can be obtained from equation (7.10) and (7.11) respectively.

The level of light that due to the reflection from the ground can be evaluated by equation (7.14). Although this light source is not the major part of the indoor illuminance, it is important especially when the ground can receive direct sunlight.

7.2.2.2 Sun and sky illuminance on vertical window surface

Having discussed the illuminance on the ground, this section concentrates on the illuminance on vertical window surface. The daylight that is received by the vertical facades composes of the direct sunlight and the diffuse skylight. The light from the direct sun is the dominant component of the interior daylight illuminance if a window surface can receive direct sunlight. According to Tregenz (1995), the sun will be visible at the window when the following criterion is satisfied,

$$\tan \alpha_s \geq \tan \omega \cos(\gamma - \gamma_s) \tag{7.15}$$

where ω is the elevation angle of the highest point of the opposite building from the window as shown in Figure 7.1.

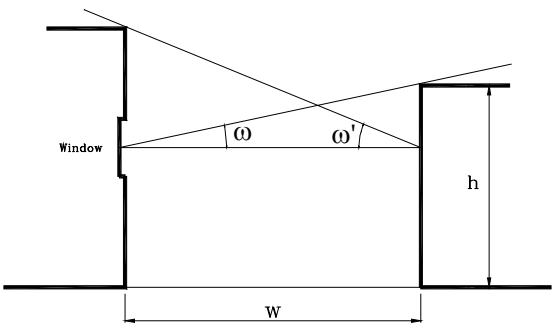

Figure 7.1 Elevation angles

If the criterion as stated in equation (7.15) is satisfied, the window will receive direct sunlight. The daylight illuminance at the vertical window due to direct sunlight (E_{vs}) can be calculated by,

$$E_{vs} = E_{dn} \cos \vartheta \tag{7.16}$$

where ϑ is the angle of incidence of beam sunlight.

The light from the diffuse sky may be blocked partly by the obstructing buildings. The portion of the sky that obscured by the buildings can be represented by a factor that is related to the size and shape of the obstacles. The illuminance on vertical façade due the diffuse skylight can be expressed in terms of the diffuse sky illuminance on a horizontal surface and the factor as follows,

$$E_{vk} = E_{kh}\left(\frac{1}{2} - cf_{\omega}\right) \tag{7.17}$$

where cf_{ω} is called the configuration factor which depends on the size and shape of the obstruction. With a horizontal skyline parallel to the window plane, cf_{ω} can be written in terms of the elevation angle ω,

$$cf_{\omega} = \frac{\sin \omega}{2} \tag{7.18}$$

As a result, the total illuminance on the vertical window due to the diffuse sky and the direct sun $E_{w(sk)}$ can be evaluated by combining equation (7.16) and (7.17),

$$E_{w(sk)} = E_{kh}\left(\frac{1 - \sin \omega}{2}\right) + E_{dn} \cos \vartheta \tag{7.19}$$

In order to take into account the inter-reflection between opposite facades, it is necessary to calculate the illuminance on those façades due to the diffuse skylight and the direct sunlight. Similar to equation (7.19), the required illuminance $E'_{w(sk)}$ is,

$$E'_{w(sk)} = E_{kh}\left(\frac{1-\sin\omega'}{2}\right) + E_{dn}\cos\vartheta \tag{7.20}$$

where ω' is the elevation angle viewed from the opposite building as shown in Figure 7.1. If the criterion of equation (7.15) is not satisfied, i.e. no direct sun shines on the windows, the last term in equation (7.19) and (7.20) can be omitted. More details on the inter-reflection between opposite facades will be discussed in section 7.2.2.3.

7.2.2.3 Reflected illuminance on vertical facades

There are two sources that contribute to the reflected light received on a vertical façade: one is reflected from the ground and the other is reflected from the opposite facades. The principle of estimating the daylight reflected from the ground is the same as estimating the ground reflected solar radiation as discussed in section 4.2.1 (i.e. equation (4.8)), but with the solar radiation values replaced with the illuminance values. And the tilted angle β is 90° for vertical facades. Therefore the reflected illuminance from the ground can be written as a function of the mean ground illuminance E_g and the ground reflectance ρ as follows,

$$E_{w(g)} = \frac{1}{2}E_g\rho \tag{7.21}$$

The method developed by Tregenza (1995) also takes into account the inter-reflection between opposite buildings. A ratio R_w between the illuminance on the opposite façade and the reflected illuminance due to the opposite facade on the window (see Figure 7.1) was established; and R'_w is the reciprocal relationship. These two ratios can be expressed in terms of the respective configuration factors and reflectances as follows,

$$R_w = cf_w \rho'_w \tag{7.22}$$

$$R'_w = cf'_w \rho_w \tag{7.23}$$

By using the expressions above, the illuminance on the window from the light inter-reflected between facades $E_{w(o)}$ can be written as,

$$E_{w(o)} = \frac{(E_{w(sk)} + E_{w(g)})R_w R'_w + (E'_{w(sk)} + E_{w(g)})R'_w}{1 - R_w R'_w} \tag{7.24}$$

It is noticed that $E_{w(sk)}$ has been incorporated into equation (7.24), which means the light from the direct sun and the diffuse sky are also considered. Apart from that, the light reflected from the ground ($E_{w(g)}$) and from the facades inter-reflection (the second term in the numerator) are also taken into account.

7.2.3 Final mean illuminance on work plane

The three components of illuminance on the vertical window have been estimated, namely, illuminance due to the direct sunlight and the diffuse sky ($E_{w(sk)}$); illuminance due to the ground ($E_{w(g)}$) and illuminance due to the opposite obstructions ($E_{w(o)}$). By using these illuminances together with the transmittances of window, the mean interior illuminance can be determined.

According to Tregenza (1995), the incident direction of light can significantly affect the proportion of light passing through the windows. Therefore, it is not suitable to use a single value of luminous transmittance for a window system for all cases. Tregenza (1995) has developed a set of window transmittances due to different luminous sources and receivers. The luminous sources are the three illuminance components on the vertical windows. The receivers refer to the interior surfaces such

as ceiling, walls and working planes. The window transmittances in all scenarios are shown in Table 7.2 and their typical values have been given by Tregenza (1995). As a result, the mean direct illuminance on the room surfaces can be determined by,

$$E_{ci} = \frac{A_w}{A_c}\left(E_{w(sk)}t_{sc} + E_{w(o)}t_{oc} + E_{w(g)}t_{gc}\right) \qquad \text{(Ceiling)} \tag{7.25}$$

$$E_{vi} = \frac{A_w}{A_v}\left(E_{w(sk)}t_{sv} + E_{w(o)}t_{ov} + E_{w(g)}t_{gv}\right) \qquad \text{(Window wall)} \tag{7.26}$$

$$E_{pi} = \frac{A_w}{A_p}\left(E_{w(sk)}t_{sp} + E_{w(o)}t_{op} + E_{w(g)}t_{gp}\right) \qquad \text{(Working plane)} \tag{7.27}$$

where A_c, A_v and A_p are respectively the area of the ceiling, the walls above the working plane level (excluding the window wall) and the working plane itself. A_w is the transparent area of the glazing. In semi-transparent BIPV modules, A_w is the area of the whole module excluding the solar cell areas.

Table 7.2 Component of window transmittance

	Sunlight & Skylight	**Reflected light from obstructions**	**Reflected light from ground**
Ceiling	t_{sc}	t_{oc}	t_{gc}
Walls excluding window wall	t_{sv}	t_{ov}	t_{gv}
Working plane	t_{sp}	t_{op}	t_{gp}

Equations (7.25) to (7.27) are the direct interior illuminance on the individual surfaces, but the inter-reflection between surfaces is not considered in these equations. The inter-reflected component also contributes significantly to the interior lighting. The mean illuminance over all room surfaces from inter-reflected light E_r can be

written as a function of the reflectances of various interior surfaces,

$$E_r = \frac{E_{ci} A_c \rho_c + E_{vi} A_v \rho_v + E_{pi} A_p \rho_p}{A(1-\rho)} \tag{7.28}$$

ρ_c, ρ_v and ρ_p are respectively representing the reflectances of the ceiling, walls (excluding window wall) and working plane; A is the total enclosing surface area above the working plane including the ceiling; ρ is the average reflectance of all the surfaces. The final illuminance on various interior surfaces can be calculated by adding E_r to equations (7.25) to (7.27). The surface of greatest concern is the working plane. Therefore, if we take working plane as an example, the final illuminance on it is,

$$E_p = E_{pi} + E_r \tag{7.29}$$

As a result, the average illuminance on the working plane can be estimated by the procedure described in this section. After determining this illuminance, the additional power required and the power saved by the artificial lights due to the use of daylight can be calculated. The calculating procedure will be outlined in the next section.

7.3 POWER CONSUMPTION OF ARTIFICIAL LIGHTS

The procedure presented in section 7.2 results in the average illuminance level of daylight available on the working plane under different outdoor conditions. It is necessary to quantify the power consumption of the artificial lights after the

integration of daylight. The energy saving potential of utilizing daylight in buildings is great. It has been reported that about 40% of the lighting energy can be saved in a cellular office's perimeter area of a building by using daylight together with dimmable electronic ballasts under Hong Kong conditions (To et al., 2002). However, if semi-transparent BIPV modules are integrated in the buildings, the power consumption of artificial lights will be increased because part of the daylight is shaded by the solar cells in the BIPV modules. In order to calculate the power consumption of artificial lights, the mean interior illuminance on the working plane as described in the previous section is a necessary input. A simple method for determining the power consumption of artificial lights is described in the following paragraphs.

If the illuminance level of daylight available on the working plane is higher than required, no artificial light is needed. Conversely, if the illuminance level of daylight available is lower than required, additional artificial lighting has to be switched on to maintain a suitable level of light on the working plane. The standard illuminance that is required on the working plane E_{std} can be found in various lighting guidelines published by relevant organizations such as The Chartered Institution of Building Services Engineers (CIBSE) and Illuminating Engineering Society of North America (IESNA). The power required by the artificial lighting per unit floor area P_{lgt} is the power to produce the additional illuminance level after taking daylight into account. For an ideal continuous artificial light dimming system, the additional power can be determined by this equation,

$$P_{\lg t} = \frac{E_{std} - E_p}{K_{el} \cdot LLF \cdot UF} \qquad (\mathrm{W/m^2}) \qquad (7.30)$$

where K_{el} is the luminous efficacy of the artificial lighting in *lm/W*; *LLF* is called the light loss factor, which is used in lighting calculations as an allowance for lamps or luminaries operating at other than rated (initial) conditions and for the depreciation of the components of the lamp (IESNA, 1993); *UF* is the utilization factor which is the ratio of luminous flux from a luminaire received on the work plane level to the luminous flux emitted by the lamp (IESNA, 1993). For an on/off lighting control system (i.e. no dimming), if the daylight illuminance is less than the lighting requirement, then the additional power that needed to reach the lighting requirement is,

$$P_{\lg t} = \frac{E_{std}}{K_{el} \cdot LLF \cdot CU} \qquad (\mathrm{W/m^2}) \qquad (7.31)$$

In on/off lighting control systems, the lamp has to consume its full power if the daylight is not sufficient to satisfy the lighting requirement. The full power is indicated in equation (7.31). To calculate the energy consumption of the artificial lights over a specific time period, the P_{lgt} in equation (7.30) and (7.31) are multiplied to the duration of the specific time period.

7.4 SUMMARY

The approach to estimating the interior daylight illuminance has been developed in this chapter. This method is able to determine the average daylight illuminance on the working plane by taking into account the direct sunlight, the diffuse daylight and

the reflected light from outdoor obstructions. Although this method is not as powerful as the sophisticated daylight simulation programs, it enables researchers to implement a spreadsheet program to calculate the hourly indoor daylight illuminance, which is sufficient for the purposes of the present study.

Energy saving by utilization of daylight in buildings is substantial. The use of the semi-transparent BIPV modules allows daylight utilization and therefore reduces the power consumption of artificial light in buildings. The method of estimating the power saving of the artificial lighting due to the daylight utilization has been described in this chapter. The power saving is one of the vital components in assessing the energy performance of the semi-transparent BIPV modules. For different solar cell areas in the semi-transparent BIPV modules, the energy saving of the artificial lighting can be evaluated by the method presented in this chapter by varying the transparent area in the equations.

In addition to the heat gain model and the power generation model, the model described in this chapter is an essential part in assessing the energy performance of the semi-transparent BIPV modules. Simulation results and analysis are given in Chapter 9 to illustrate the impacts on the energy performance of different module areas and solar cell areas by using the models presented in this thesis.

CHAPTER 8

EXPERIMENTAL STUDY ON THE HEAT GAIN OF THE SEMI-TRANSPARENT BIPV MODULE

In order to examine the validity of the SPVHG model developed in Chapter 5, an experimental test on a semi-transparent BIPV module was performed. This chapter describes the details and results of the test.

The test was carried out in the Solar Simulator Laboratory of The Hong Kong Polytechnic University. A solar simulator and a specially designed calorimetric box were constructed in the laboratory and used in the test. In this chapter, the principle of the test according to related international standards is first outlined. The major equipment and the calibration method of the calorimetric box are then described. The thermal performance of the semi-transparent BIPV module was assessed according to the experimental results. A comparison between the experimental data and the simulation results are also presented.

As revealed in the comparison, the simulation results generated by the SPVHG model are reasonably close to the experimental data. Although slight discrepancies appear between the two sets of values, the accuracy of the model is acceptable in general. Details of the analysis are presented in this chapter.

8.1 BACKGROUND

The amount of heat transfer through a glass window greatly influences the energy consumption of the air-conditioning system of a building. Practical test methods for assessing the thermal performance of windows have been developed for more than two decades. Klems (1989) developed an outdoor test facility called the MoWiTT (Mobile Window Thermal Test) Facility. It is a test room facility which exposes window glass to real weather conditions. Klems (1989) used this test facility to determine the U-value and solar heat gain of windows with different frame materials such as wood and aluminium, He also compared the results with the prediction of the glazing simulation package, WINDOW. He found that the experimental results and the simulation results supported each other. The MoWiTT test could be applied in future studies. However, the difficulties with this test are the need for a outdoor environment and a specially designed facility.

Some international standard organizations have established related standards for regulating the test method of thermal characteristics of clear window glass. The most common standards are ASTM C1199 published by the American Society for Testing and Materials (ASTM) International, and BS 874 - 3.1 & 3.2 published by the British Standard (BS). In order to reduce the influences of outdoor weather, a number of solar-simulator-based experimental studies have been conducted by various researchers with reference to the aforesaid standards using indoor conditions. Harrison and Dubrous (1990) constructed a calorimetric test cell to determine the thermal characteristics such as shading coefficient and U-value of different fenestration systems ranging from single to triple glazing. The authors defined a term,

thermal efficiency, of the windows, which is defined as the net heat gain through the window divided by the solar radiation on its surface per unit area. By using the thermal efficiency, the shading coefficient and U-value of the fenestration systems can be found.

Similar indoor solar-simulator-based experimental study has also been conducted by Alvarez et al. (2000). They studied the thermal parameters of window glass with different thicknesses and surface coatings. Their results revealed that the reflective glass has a substantial reduction in radiant heat gain to the indoors compared with the clear glass.

The experimental works carried out by the previous researchers have illustrated some methods for determining the thermal characteristics of window glass. By referring to the appropriate standards and previous studies, an experimental test method has been developed to measure the heat gain of the semi-transparent BIPV module for the current research. The details of the measurements are outlined as follows.

8.2 THEORY OF THE EXPERIMENTAL TEST

Laboratory tests have been carried out to assess the heat gain through the semi-transparent BIPV modules. The test procedure is made with reference to the related standards, namely, the ASTM C1199, C1363, and BS 874 - 3.1 & 3.2, which specify the test requirements of window glass and building assemblies. Although there

is no existing standards that are directly related to the testing of heat transfer through the semi-transparent BIPV module, the methods and the requirements stated in the above standards can be referred to because the underlying theories are applicable to the current study.

The principle of the test method is the measurement of the net heat flow through the semi-transparent BIPV module and the corresponding temperature difference across the module at an equilibrium state. To determine the net heat gain through the module, the test module was mounted in a specially designed calorimetric box apparatus. The box was placed under the solar simulator with the module facing the simulator. A pyranometer was located at the level same as the PV module to measure the solar radiation intensity. Heat supplied by the solar simulator passed through the PV module and entered the calorimetric box. The net heat gain (Q_{net}) through the PV module was balanced by the energy extracted by the chilled water flowing inside the cooling coil at the rear of the test box. A heat exchanger and a compact chiller with temperature control were installed to maintain the supply chilled water temperature. Figure 8.1 shows the schematic diagram of the calorimetric box set-up.

The net heat gain, Q_{net} can be evaluated by considering the heat loss through the box walls (Q_{loss}) and the heat extracted by the chilled water in the cooling coil (Q_p). The energy balance of the whole system can be written as follows,

$$Q_{net} = Q_{loss} + Q_p \tag{8.1}$$

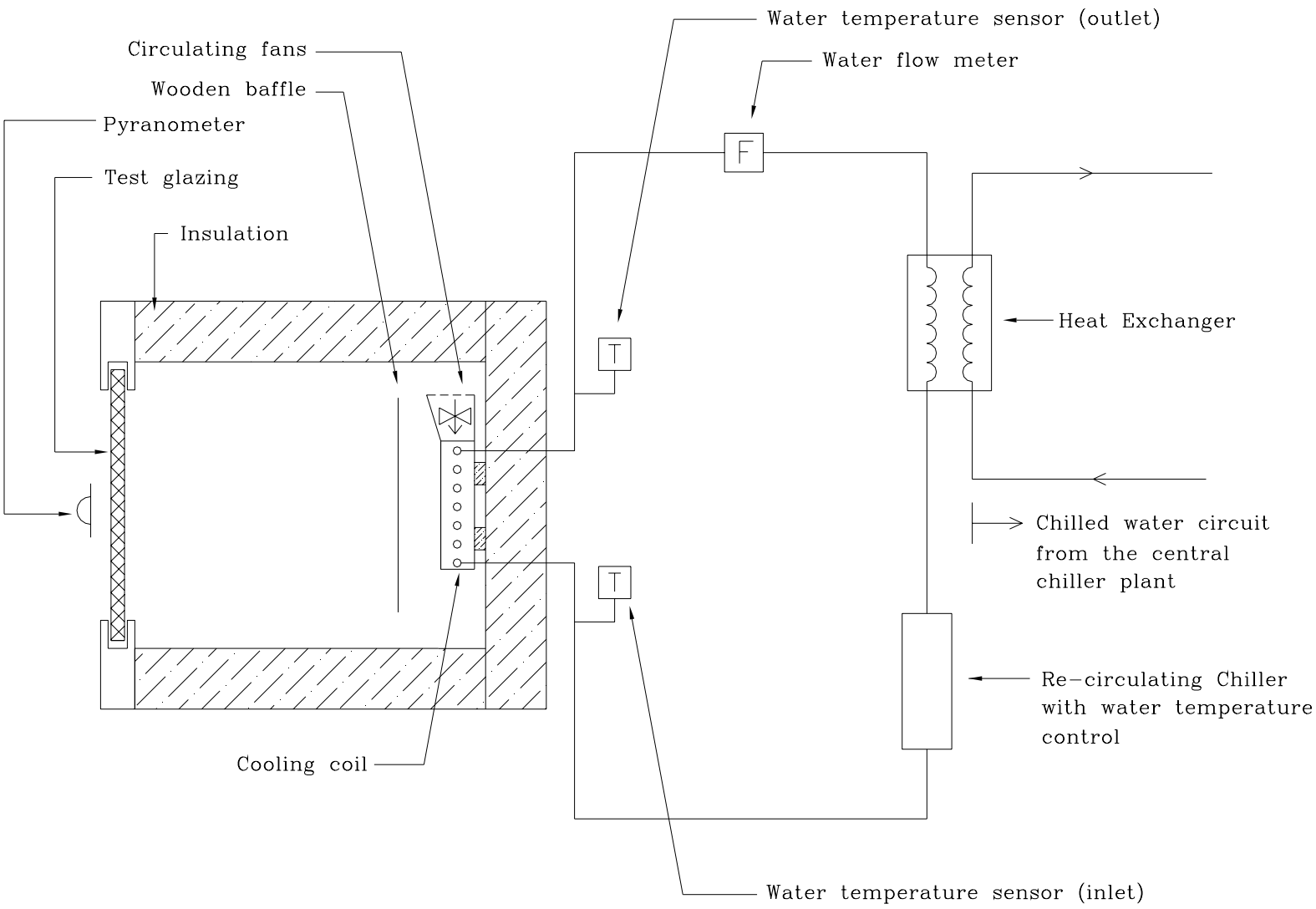

Figure 8.1 Schematic diagram of the calorimetric test box setup

Q_{loss} and Q_p can be determined separately. Q_{loss} can be calculated by the U-value of the box walls (U_{wall}), the temperature difference between the interior and ambient air. Q_p can be evaluated by the chilled water flow rate and the water temperature difference between the outlet and inlet of the cooling coil. Q_{loss} and Q_p can be expressed respectively as follows,

$$Q_{loss} = U_{wall} \times A_{wall} \times (T_i - T_o) \tag{8.2}$$

$$Q_p = \dot{m} \times C_p \times (T_{outlet} - T_{inlet}) \tag{8.3}$$

where A_{wall} is the average box wall area, T_i and T_o are the interior and ambient air temperature respectively, $\dot{m}$ is the chilled water mass flow rate, C_p is the specific heat capacity of the circulating water, T_{outlet} and T_{inlet} are the water temperatures at the coil outlet and inlet respectively. The U-value of the box walls (U_{wall}) has to be determined by a calibration procedure. The details of the calibration will be discussed in section 8.3.2.

Since a circulating fan was required to mix the air inside the box, by taking into account the power consumption of the circulating fan (Q_{fan}), equation (8.1) can be modified as,

$$Q_{net} + Q_{fan} = Q_{loss} + Q_p \tag{8.4}$$

As a result, the net heat gain through the PV module can be calculated by substituting equation (8.2) and (8.3) into equation (8.4).

The parameters of the experiment required in the above calculation of the net heat gain were measured by appropriate measuring devices. The experimental setup was also equipped with a data acquisition system to collect test data from different measuring devices throughout the test at a constant time interval. The details of

different equipment and measuring devices used in the experiment will be described in section 8.3 and 8.4.

8.3 MEASURING DEVICES AND EQUIPMENT CALIBRATION

A number of measuring devices and equipment were used in the experimental test of the current study. All of them have played an important role throughout the experiment. In order to obtain accurate and reliable results, all the devices should be calibrated. This section outlines the calibration procedure and results of different equipment and devices used in the experimental study.

8.3.1 Calibration of the thermocouples and thermistors

All the air temperatures and box wall surface temperatures were measured by Type-T (copper/copper-nickel) thermocouples, while two thermistors were used to measure the chilled water temperature at the inlet and outlet of the cooling coil. All of them were connected to the data logger for displaying and recording the data. Figure 8.2 is a picture of the data logger.

Figure 8.2 The data logger

The calibrations of the thermocouples and thermistors were performed by comparing the records from the data logger with the readings of a standard

mercury-in-glass thermometer, whose resolution is 0.1 °C. During the calibration, all the thermocouples or the thermistors were immersed together with the thermometer in a water bath. An automatic stirrer was prepared in the water bath to ensure that the water was mixed thoroughly. Since the measuring ranges required in the current experiment are different between the thermocouples and the thermistors, they were calibrated separately.

The measuring range of the thermocouples used in the experiment is approximately 0 °C to 100 °C. Therefore, the thermocouples were calibrated at freezing point, boiling point and several points in the range of 25 °C to 42 °C. Figure 8.3 shows the calibration results for the thermocouples. The actual temperature in the figure is that from the mercury thermometer. The readings from the data logger are expressed in °C. It can be seen from the figure that the readings from the thermocouples were virtually the same as those indicated by the mercury thermometer. The standard deviation from the actual temperature for the thermocouples is 0.02. This shows a high reliability of the thermocouples.

The two thermistors and the mercury thermometer were immersed together in the well mixed water bath for the calibration. Since the output of the thermistors was resistant values in kohm, the values should be calibrated in order to determine the corresponding temperature of the resistant outputs. Figure 8.4 and 8.5 show the calibration results. As shown in these figures, a linear relationship can be established between the resistant outputs and the temperatures. A linear equation can be obtained by linear regression on the data for each of the thermistors. Therefore, the data obtained in the experimental test can be converted to temperature by the two

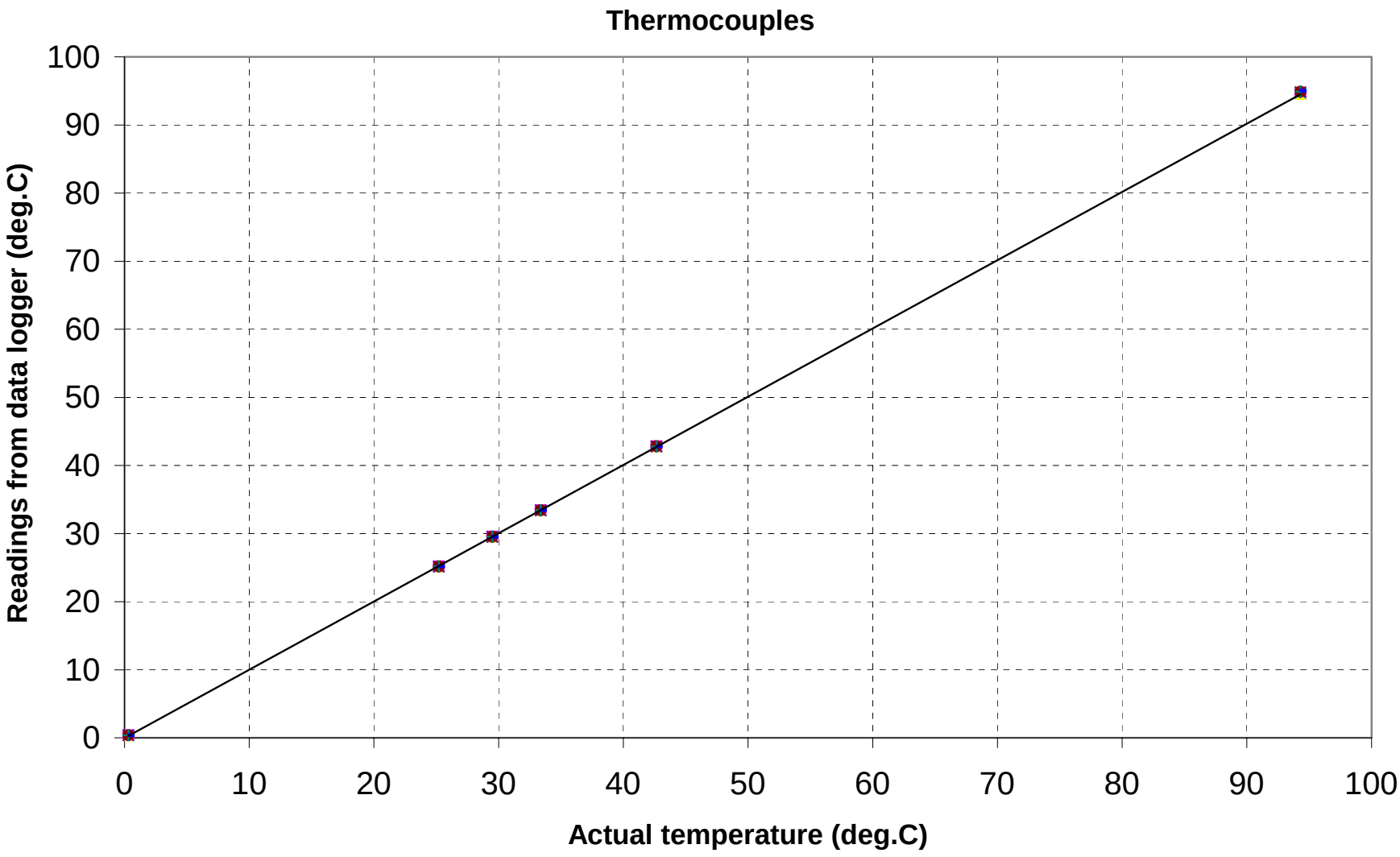

Figure 8.3 Calibration results of the thermocouples

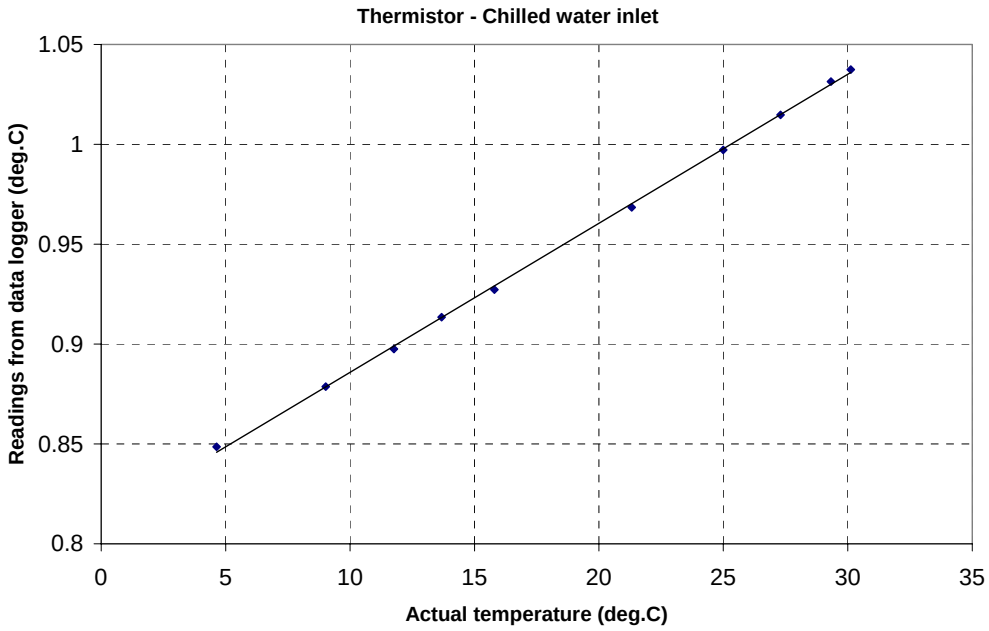

Figure 8.4 Calibration results of the thermistor for chilled water inlet

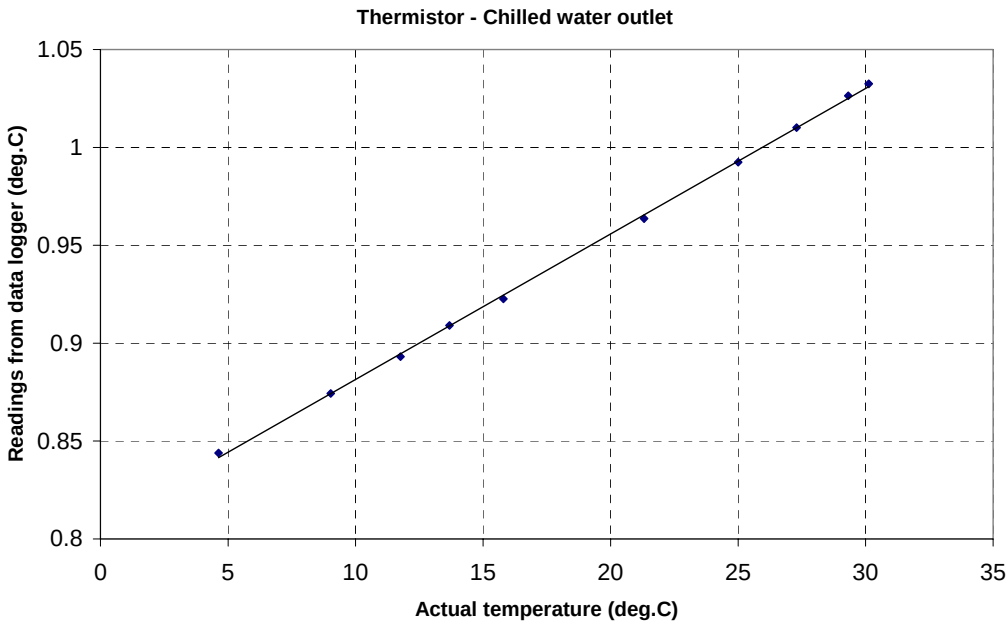

Figure 8.5 Calibration results of the thermistor for chilled water outlet

equations as follows,

$$y = 0.0075x + 0.8113 \quad \text{(inlet)} \tag{8.5}$$

$$y = 0.0074x + 0.807 \quad \text{(outlet)} \tag{8.6}$$

8.3.2 Calibration of the calorimetric box

8.3.2.1 Construction of the calorimetric box

To measure the heat flux through the semi-transparent BIPV module, a calorimetric box apparatus have been designed and constructed. The size of the calorimetric box was 1000mm(W) by 800mm(D) by 800mm(H). In order to minimize the heat loss through the box, the walls of the box were well insulated by a sandwich construction of two plywood skins with foam as insulating material between them. A mounting frame which was made of the same material as the box was used to mount the PV module at the front of the box. All perimeter contacts between each wall of the box were provided with compressible rubbers to prevent air flow between the box and the laboratory surroundings. The box was inclined during the test in order to take into account the effects incident angle of solar radiation.

As shown in Figure 8.1, a wooden baffle was installed in front of the cooling coil to assist in producing uniform air velocities and temperature distributions. All the inner surfaces of the box were coated with matt black finishing to prevent heat from radiating between surfaces.

Type T thermocouples were adopted to measure the air temperature and the box wall surface temperature. Ten thermocouples were evenly distributed through the interior space of the box. Another thirty-two thermocouples were embedded in the

interior and exterior of the top, bottom and side walls of the box to measure the temperature difference across the of the box walls. All the thermocouples were connected to the data logger for recording data at a constant timed interval. The interior view of the calorimetric box is shown in Figure 8.6.

Figure 8.6 Interior of the calorimetric box

8.3.2.2 Calorimetric box calibration

The calorimetric box was calibrated to determine the U-value of its walls, U_{wall}. An electric heater was placed at the back of the test box and was switched on at the beginning of the calibration. The power supplied to the heater can be adjusted. The ambient and inside temperatures of the box were recorded until a steady state was reached. Figure 8.7 illustrates the schematic diagram of the calibration. The U-value of the box walls was determined by averaging the measured interior and exterior temperatures and the energy supplied by the electrical heater at steady state. The following equations shows the expression of the U_{wall},

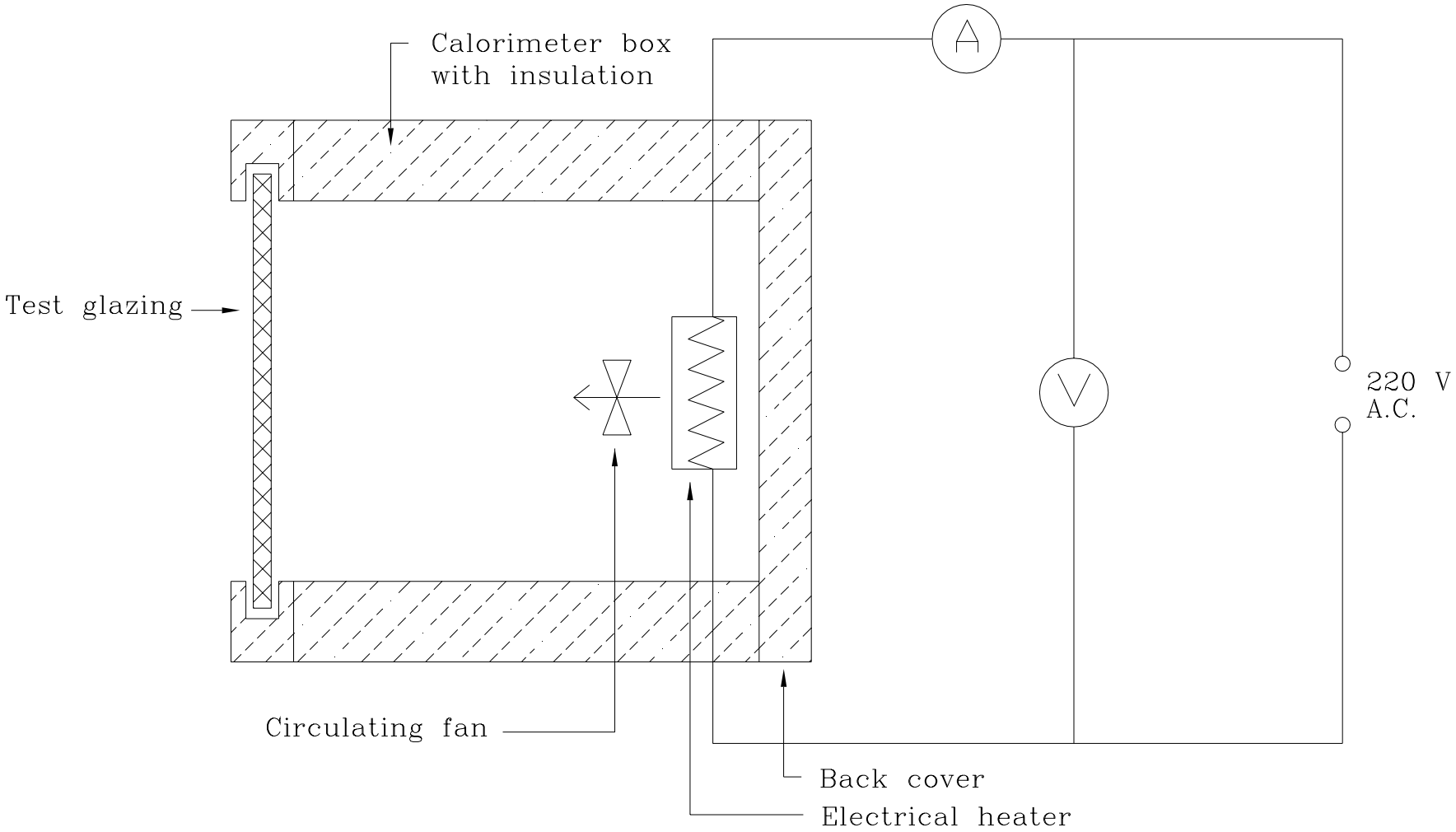

Figure 8.7 Schematic diagram of the calorimetric box calibration

$$U_{wall} = \frac{Q_{heater} + Q_{fan}}{A_{wall} \times (T_i - T_o)} \tag{8.7}$$

where Q_{heater} is the energy supplied by the electric heater; A_{wall}, Q_{fan}, T_i and T_o have been defined in section 8.2. Three trials of power supplies to the heater were conducted. In each trial, the heater was switched on for at least eight hours to ensure that the system has reached a steady state

The results of the calorimetric box calibration are shown in Table 8.1. The U-values obtained in each trial are very close to each other. Therefore the resultant U-value of the box walls can be determined by averaging the results of the three trials.

Table 8.1 Results of calorimetric box calibration

Heater power input (W)		**Average air temperature at steady state (°C)**		**U_{wall} (W/m^2°C)**
		Inside the box	Outside the box	
1.	190	42	21.1	2.03
2.	270	50.4	20.8	2.04
3.	368.2	59.5	20.1	2.1
			Ave. U_{wall}:	**2.06**

8.3.3 Water flow sensor

After calibrating the calorimeter box, the water flow sensor is another device to be calibrated. A pulse-type water flow sensor was adopted in the experimental study to measure the chilled water flow rate. It was also connected to the data logger for data recording. During the calibration of the flow sensor, water was pumped at a constant flow rate and flowed through the sensor in a specific period of time. The

water flow rate during the period of time was detected by the flow sensor and the data was recorded by the data logger. At the same time, the water flow rate was recorded manually by dividing the volume of water collected by the time elapsed when the water flowed into an open tank. This water flow rate was then compared with the one collected by the data logger. Different trials were tested by adjusting the flow rates of the water pump. Figure 8.8 shows the calibration results. This figure shows that the values measured by the flow rate sensor are directly proportional to the actual values. Their relationship can be obtained by linear regression on the plot in Figure 8.8 as follows,

$$\textit{Actual flow rate} = 1.04 \text{ x } (\textit{flow rate measured by the flow sensor}) \tag{8.8}$$

Therefore, according to equation (8.8), the values measured by the flow sensor should be multiplied by 1.04 to obtain the actual value.

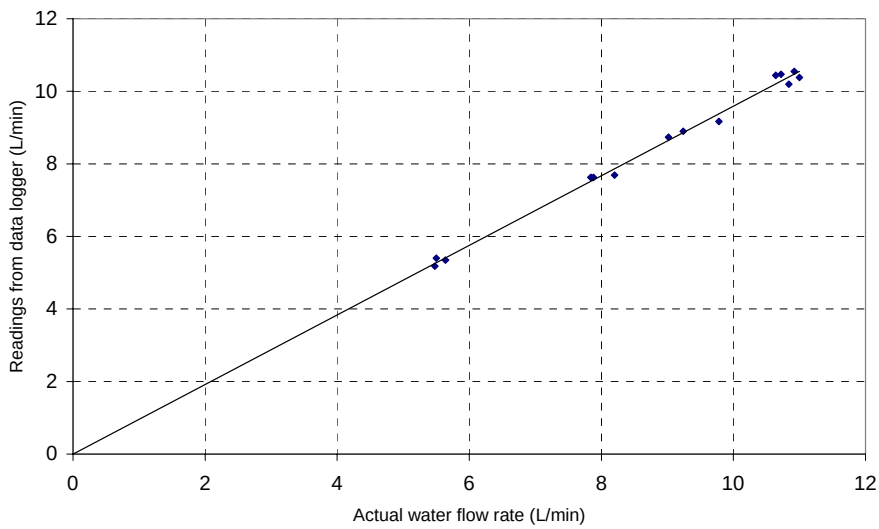

Figure 8.8 Calibration results of the water flow sensor

8.4 DESCRIPTIONS OF OTHER MAJOR EQUIPMENT

8.4.1 The solar simulator

The solar simulator used in the experiment is a steady-state type simulator. It comprises 363 dichroic tungsten halogen lamps of 75W each to provide a test area of 2m by 2m. The solar irradiance of the solar simulator is adjustable from zero to approximately 1600 W/m^2. Therefore, the solar simulator can provide opportunities to test equipment under various light levels. The solar simulator is mounted on a steel supporting frame and its height can be adjusted along the frame to satisfy different testing conditions. The performance of the solar simulator is able to meet the requirements of Class C specified in the International Standard IEC 904-9. Figure 8.9 shows the arrangement of the solar simulator and the calorimetric box during the experiment.

Figure 8.9 The calorimetric box under radiation of the solar simulator

8.4.2 The pyranometer

The solar energy flux incident on the tested BIPV module is the key data in the test. A pyranometer (MS-802, EKO) was used to measure the solar energy flux per unit area of the module during the test. The measured solar radiant energy is in W/m^2, which is the global irradiance including the direct, diffuse and reflected component. The spectral range of the pyranometer is 300 to 2800nm. Figure 8.10 is a picture of the pyranometer.

Figure 8.10 The pyranometer

8.4.3 The semi-transparent BIPV module sample

The semi-transparent BIPV module sample used in the test has a size of 1181mm (H) x 536mm (W) x 3mm (D). There are 6 x 11 poly-crystalline EFG silicon solar cells in the module, each of which is 100mm x 50mm. The solar cells were arranged in six rows and a clear gap exists between two rows. Excluding the area of the mounting frame, the solar cells covered 60% of the module area. The temperatures at the front and the back were monitored by eight thermocouples during the test (with four thermocouples on each side). Figure 8.11 shows a picture of the module mounted on the mounting frame.

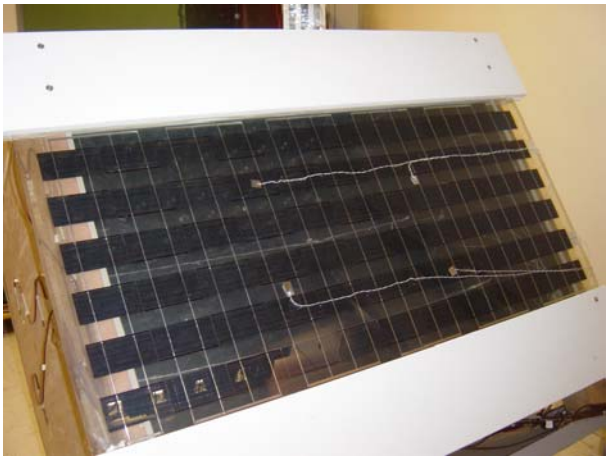

Figure 8.11 The semi-transparent PV module sample

8.4.4 Water temperature controller

A water circulating chiller was deployed to circulate cold water throughout the water circuit and to maintain a constant temperature of the water that was supplied to the cooling coil. The cooling capacity of the compact chiller is 300W at 20 °C, which is able to cool the water down to 10 °C or below depends on the ambient temperature. The temperature accuracy of the chiller is +/- 0.01 °C, which is highly precise. The picture of the chiller is shown in Figure 8.12.

Figure 8.12
The circulating chiller

After introducing the equipment used in the experiment, the next section will focus on the experimental results and then compares these results with the simulation results in order to examine the validity of the SPVHG model.

8.5 VALIDATION RESULTS AND DISCUSSIONS

The simulation results were compared against the experimental results to examine the accuracy of the simulation model. Different cases were performed by adjusting the solar radiation output of the solar simulator. The parameters used in the experiment were inputted to the SPVHG model to generate simulation results for comparisons. Both the module inner surface temperature and the net heat gain were compared. Three cases of different solar irradiances were considered in the comparison. The solar irradiances studied are namely 400W/m^2, 600W/m^2 and 800W/m^2, which are within the range of typical solar irradiance in Hong Kong.

8.5.1 Module's temperature

The average inner surface temperatures of the module obtained from the simulation model and the experiment for the three cases are shown in Figures 8.13 to 8.15. As shown in the graphs, the inner surface temperature of the module increased rapidly at the beginning. The increasing trend slows down thereafter and finally levels off when the system reaches steady state. When compared with the experimental results, the simulation model predicts the inner glazing surface temperature accurately, and follows the trend of the variation. The model predicts the inner surface temperature with a maximum error of more than 10%. This maximum error occurred at the beginning in the transient state. In the steady state, the error drops to less than 3% for all the three cases. This implies that the model simulates the module temperatures very well. The inner surface temperatures in different cases are summarized in Table 8.2.

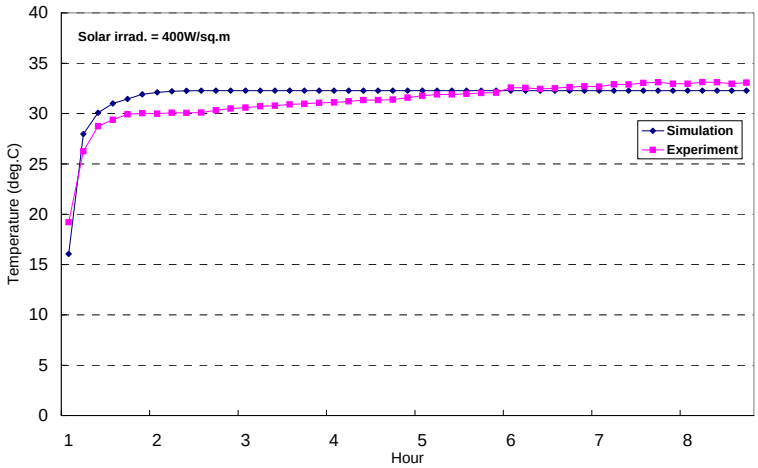

Figure 8.13 Comparisons between the experimental and simulation results of the inner surface temperature for case 1

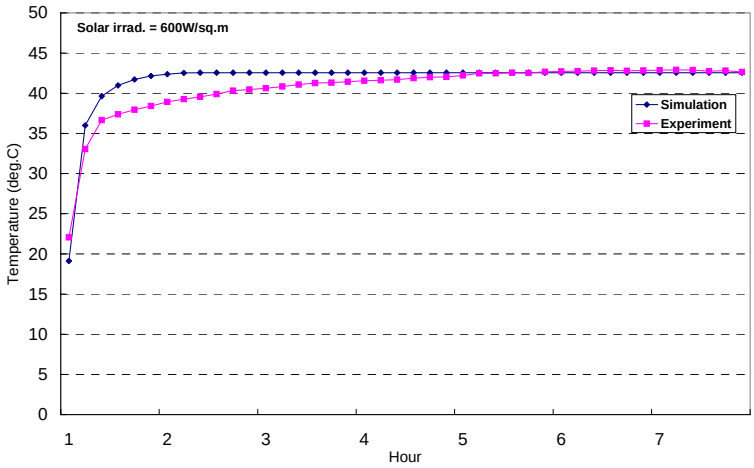

Figure 8.14 Comparisons between the experimental and simulation results of the inner surface temperature for case 2

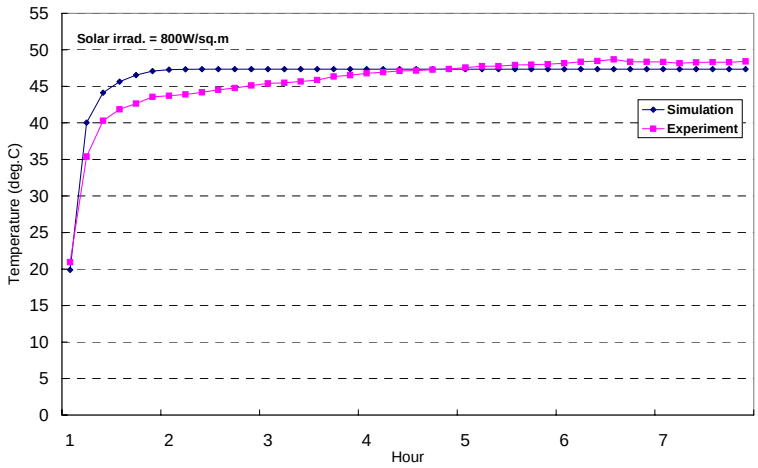

Figure 8.15 Comparisons between the experimental and simulation results of the inner surface temperature for case 3

Table 8.2 Comparisons of module inner surface temperature

	Solar irradiance (W/m^2)	Inner surface temperature at steady state (°C)		Error
		Experiment	Simulation	
Case 1	400	33.0	32.2	2.4%
Case 2	600	42.6	42.8	0.5%
Case 3	800	48.3	47.3	2.1%

8.5.2 Net heat gain

The heat gain through the semi-transparent BIPV module under the experimental conditions was evaluated according to the approach described in section 8.2. The values at steady state in the experiment were compared with the simulation results. Only the values at steady state were considered in the comparisons because the heat gains are only valid in steady state. Table 8.3 summarizes the results of the heat gain comparisons.

Table 8.3 Comparisons of net heat gain

	Solar irradiance (W/m^2)	Net heat gain (W/m^2)		Error
		Experiment	Simulation	
Case 1	400	180.3	217.8	20.8%
Case 2	600	282.5	331.7	17.4%
Case 3	800	402.1	418.7	4.1%

As shown in Table 8.3, comparatively large errors between the experimental and simulation results occurs in case one and two when the solar irradiance is comparatively small. In case three, when the solar irradiance is large, the SPVHG model simulates the situation well. These results indicate that the SPVHG model is able to simulate the heat gain accurately. The errors in case one and two are attributed to the test procedure and the uncertainties of the measuring devices.

The heat extracted by the chilled water in the cooling coil (Q_p) is considered as a major source of error. Since Q_p is a dominant term in the calculation of net heat gain, the errors caused by Q_p affect the results greatly. The uncertainty of Q_p is dependent on the water flow and the water temperature rise across the cooling coil. The uncertainty in Q_p can be reduced by lowering the chilled water flow rate, and thus increasing the temperature rise across the cooling coil. The effects of the uncertainty are much more obvious at low irradiance levels. Therefore, the errors in case one and two are larger than that of case three. Although the experimental method is designed to allow for a water temperature rise of approximately 5 $^{\circ}$C across the cooling coil by adjusting the flow rate, these optimal conditions may not always be achieved due to equipment limitations, such as flow rate control. Therefore, the error in case 3 is the least among the three cases because the water temperature difference across the cooling coil is the largest in case 3 (about 3.3 $^{\circ}$C at steady state), and thus the uncertainty in Q_p is not significant in this case. On the whole, the SPVHG model is able to simulate the heat gain through the semi-transparent BIPV module with reasonable accuracy.

8.6 SUMMARY

The experimental method for validating the SPVHG model has been described in this chapter. The theory of the validation and the equipment used in the test have also been presented. The results generated by the SPVHG model are compared with the experimental results to check their validity.

A calorimetric box was designed and constructed for testing the net heat gain through the semi-transparent BIPV module. A steady-state-type solar simulator was adopted in the test to provide uniform solar radiation on the surface of the BIPV module during the test. The heat transferred through the module is rejected to the chilled water circulating in the cooling coil in the box. All data is measured by a data logger until steady state is reached.

Generally speaking, the simulated values are reasonably close to the measured values. Regarding the inner surface temperature of the module, the error between the simulation and measurement is less than 3% in all cases. For net heat gain, although deviations are observed in some cases, the smallest error between the two results is 4.1%. The deviations are owing to experimental errors such as the uncertainties of the measuring devices, and equipment limitations. The experiment results can be more accurate if some of the parameters could be precisely controlled, such as the chilled water flow rate.

On the whole, the experimental results show that the SPVHG model is validated. Further study regarding the effects of the module's parameters on the heat gain can be carried out by using the model. The model can also be utilized to calculate the energy performance of the module in different scenarios. This facilitates the design of

building engineers when they are designing semi-transparent BIPV systems for optimizing the energy efficiency of their design. Detailed simulation study using the SPVHG model is presented in Chapter 9. The overall energy performance of this kind of BIPV module in different scenarios is also evaluated in the chapter.

CHAPTER 9

SIMULATION RESULTS

After proofing the validity of the SPVHG model by the experimental studies, the thermal performance of the semi-transparent BIPV modules under different scenarios can be simulated by applying the SPVHG model. This chapter presents the simulation results generated by the SPVHG model. The annual heat gains from the semi-transparent BIPV module are calculated. Different parameters of the module such as the solar cell area ratio, the efficiency of the solar cell, the module thickness and its orientation are studied for their impact on the annual heat gain.

In addition, a separate simulation study is given in this chapter to illustrate the energy performance of the semi-transparent BIPV module in building applications as a case study. A room in an office building which is integrated with both the semi-transparent BIPV modules and the opaque PV modules on the façade is investigated. The electricity benefits caused by the three elements, namely, the heat gain, the power generations by the PV modules and the daylight utilization are assessed using the models described in Chapter 5, 6 and 7 respectively. The resultant benefits are then evaluated.

9.1 BACKGROUND OF THE SIMULATION STUDY

9.1.1 General background

In the simulation study, one of the rooms inside a typical office building was selected. The building is assumed to be situated in Hong Kong and can receive solar radiation throughout the year without nearby obstruction. The façade of the selected room is assumed to have both the semi-transparent BIPV modules, which replace the clear glass of the windows (this form PV windows), and the opaque BIPV modules mounted on the opaque walls as a PV cladding. Figure 9.1 shows the dimensions of the room.

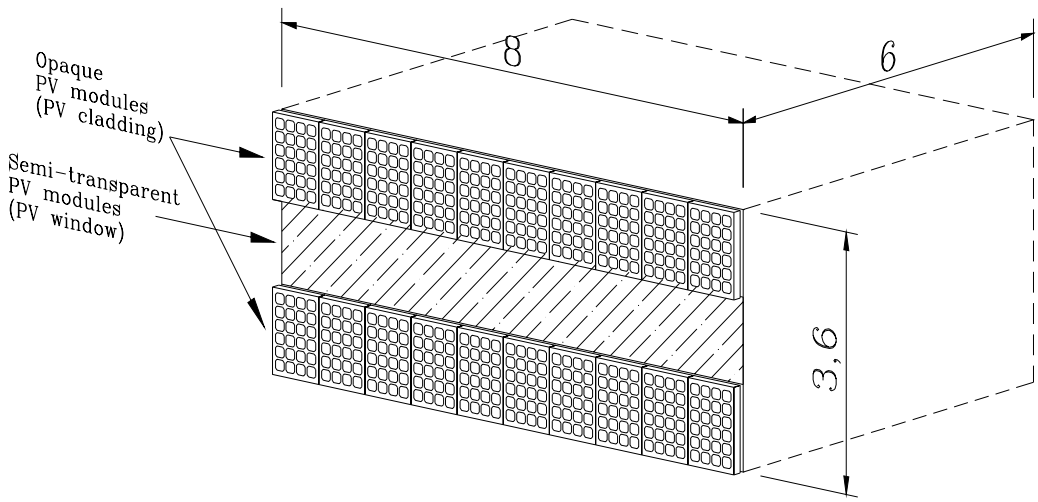

Figure 9.1 Dimensions of the room for the simulation study (all dimensions in meter, not to scale)

Based on this façade construction, the simulation study is divided into two major parts. The first part focuses on the semi-transparent BIPV modules, i.e. the PV windows. The heat gain variations due to different configurations of the

semi-transparent BIPV modules are described and analyzed. In this part, the SPVHG model is used solely to illustrate the impact of the different configurations of the modules on their thermal performance.

In the other part of the simulation study, the whole PV facade which includes both the PV glazing and PV cladding is considered. In addition to the thermal performance, the power generation from all BIPV modules on the PV facade and the energy saving due to daylight are also considered in the study. The combined effects resulted from the thermal performance, power generation and daylight utilization are evaluated in the study. Therefore, a more comprehensive conclusion on the total energy performance of a BIPV façade can be drawn.

In order to evaluate the thermal performance of the BIPV façade, the heat gain from the semi-transparent BIPV modules and the PV cladding of the façade should be determined separately. The heat gain from the semi-transparent BIPV modules can be calculated by the SPVHG model, while the heat gain from the PV cladding can be evaluated by a simplified method developed by Yang et al. (2000), which will be described in the following section.

9.1.2 Heat gain from the PV cladding

PV modules are mounted on the surface of building external walls to form PV cladding. There may be a need to design an air gap behind the PV modules for ventilation purpose to reduce the temperature of the PV modules to increase their efficiencies. The air gap affects the heat transfer process across the wall. The heat gain through the whole structure is reduced because part of the heat absorbed by the

external surface is removed by the natural ventilation in the air gap. Therefore, the cooling load is reduced compared with that of conventional massive walls.

A PV cladding can be regarded as a multi-layer wall. The heat gain through the whole structure can be determined by considering the heat transfer across each layer. The existence of the air gap makes the calculation complicated because of the uncertain air flow rate within the air gap. The convective heat transfer coefficient related to the air in the gap is therefore difficult to estimate. Yang et al. (2000) defined a new equivalent hourly average outdoor temperature for simplifying the calculation procedure of the cooling load due to the heat gain from the PV cladding. According to Yang et al., the equivalent hourly average outdoor temperature T_{ave} can be estimated by averaging the air temperature at the inlet and outlet of the air gap ($T_{gap,in}$ and $T_{gap,out}$ respectively), i.e.,

$$T_{ave} = \frac{T_{gap,in} + T_{gap,out}}{2} \tag{9.1}$$

By using the equivalent hourly average outdoor temperature T_{ave}, the calculation of the cooling load that contributed by the PV cladding can be simplified as that of a massive wall only as shown in Figure 9.2.

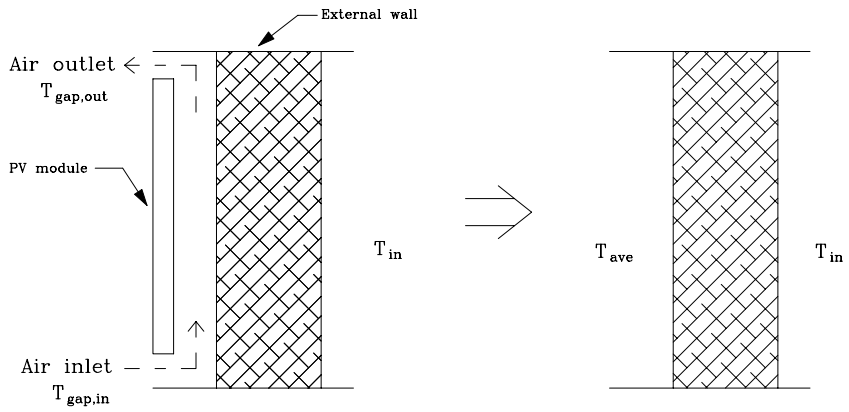

Figure 9.2 Diagram of the simplification (not to scale)

After simplifying the heat gain calculation of a PV cladding to a traditional massive wall, the heat gain through a massive wall can be evaluated by the transfer function method (TFM) as described by McQuiston and Spitler (1992). The method uses sol-air temperature to represent outdoor conditions. Also, it assumes a constant indoor air temperature throughout the calculation. Conduction transfer functions are used by the TFM to describe the heat flux at the inside of the wall as a function of previous values of the heat flux, inside and outside temperatures. Therefore, the heat gain through the wall $q_{wall,\theta}$ at time θ is given by,

$$q_{wall,\vartheta} = A\left[\sum_{n=0} b_n\left(t_{e,(\vartheta-nd)}\right) - \sum_{n=1} d_n\left(\frac{q_{wall,(\vartheta-nd)}}{A}\right) - t_r\sum_{n=0} c_n\right] \tag{9.2}$$

where:

$q_{wall,(\vartheta-nd)}$ = heat gain through the walls at time $(\vartheta - nd)$

A = indoor surface area of the walls

θ = time, in hour

d = time interval, in hour

n = summation index

$t_{e,(\vartheta-nd)}$ = sol-air temperature at time $(\vartheta - nd)$

t_r = indoor air temperature

b_n, c_n, d_n = conduction Transfer Function coefficients

The sol-air temperature in equation (9.2) is the temperature of outdoor air that in the absence of sunlight and long-wave radiation exchange, and will cause the same amount of conduction and convection heat flow through walls or fabric elements. The sol-air temperature can be expressed as (McQuiston and Spitler, 1992),

$$t_e = t_o + \frac{\alpha S_{tot}}{h_o} - \frac{\varepsilon dR}{h_o} \tag{9.3}$$

where t_o and h_o are the outdoor air temperature and convective heat transfer coefficient on the outdoor surface of the wall respectively; α and ε are the absorptance and emittance of the wall surface; R is the remainder term which covers the complicated long wavelength heat exchanges by radiation between the wall and nearby surfaces. The value of R is small, in general cases, and can be neglected (Jones, 2001).

In the case of PV cladding, T_{ave}, defined in equation (9.1), is used as the outdoor air temperature (t_o) as shown in equation (9.3). As a result, the heat gain through the PV cladding can be determined by combining equation (9.2) and (9.3).

In order to evaluate the impact of heat gain on the energy consumption of the building, it is necessary to determine the cooling load due to that amount of heat gain. The following section discusses the approach used to estimate the cooling load due to the heat gain, and the energy consumption of the building due to the cooling load.

9.1.3 Energy consumption due to the heat gain

After obtaining the heat gain values from both the semi-transparent BIPV modules and the PV cladding, the cooling load due to the heat gain can be calculated by a conversion method. Then the energy consumption of the air-conditioning systems can be determined according to the cooling load. The conversion of heat gain to cooling load can be carried out by using the room transfer function (McQuiston and Spitler, 1992). This method depends on the nature of the heat gain and on the heat

storage characteristics of the room space. The cooling load Q_ϑ at time ϑ can be determined by the corresponding heat gain q_ϑ at current time and the preceding values of the cooling load and heat gain. The relationship can be written as,

$$Q_\vartheta = \sum \left(v_o q_\vartheta + v_1 q_{\vartheta-d} + v_2 q_{\vartheta-2d} + ...\right) - \left(w_1 Q_{\vartheta-d} + w_2 Q_{\vartheta-2d} + ...\right) \tag{9.4}$$

where d is the time interval. The terms v_0, v_1,…, w_1, w_2,…are the coefficients of the room transfer function, which are related to the nature of heat gain (i.e. how much heat is transferred in the form of radiation and where it is absorbed) and on the heat storage capacity of the room space. Those coefficients can be obtained from ASHRAE Handbook according to the corresponding situations. Usually two preceding values of heat gain and cooling load are sufficient because the effects of the values more than two preceding intervals are negligible.

The heat gain through the semi-transparent BIPV modules can be calculated by using the SPVHG model developed in this thesis, while the heat gain through the opaque PV cladding can be estimated by the approach described in section 9.1.2. By using equation (9.4), the hourly cooling load caused by the heat gains from different façade elements can be calculated. As a result, the cooling load from a building envelop that incorporates both semi-transparent and opaque BIPV modules can be simulated.

The energy consumption of the air-conditioning system due to the cooling load should be evaluated in order to assess the energy performance of the PV façade. Since only one single room in a building is considered in the energy performance assessment, the equipment that consumes the major part of the total energy of the air-conditioning system is the chiller. To estimate the energy consumption of the

chiller plant, the *COP* of the chillers is required. *COP* is defined as the amount of energy removed divided by the required energy input to the chillers (ASHRAE, 2001). The definition of *COP* can be written as,

$$COP = \frac{\text{Amount of energy removed}}{\text{Net energy supplied}} \tag{9.5}$$

From the definition of *COP*, the net energy supplied to the chillers can be calculated from the amount of cooling load removed divided by the *COP* of the chillers. By assuming all cooling load can be ideally removed by the chillers, the energy supplied to the chillers can be expressed as follows,

$$\text{Net energy supplied} = \frac{\text{Amount of cooling load}}{COP} \tag{9.6}$$

As a result, the energy consumption due to the heat gain from the PV façade can be estimated by the above procedure. By incorporating also the yearly weather data, the annual energy consumption can be determined.

9.1.4 Weather data input

When running the SPVHG model and performing the energy performance calculations, a number of weather data such as the solar irradiance, and outdoor indoor air temperature are required. The weather data of the year 1989 which were recorded by the Hong Kong Observatory was adopted in the simulation. As mentioned in Chapter 4, the weather data in 1989 was used because the weather in that year has been found to be the most representative based on a statistical analysis of Hong Kong weather data (Wong and Ngan, 1993). Since only global horizontal solar irradiance values are available from the weather data records, the solar irradiance values that

were received on BIPV modules with the particular orientation were first obtained from the global horizontal values by the approach described in Chapter 4. As a result, the simulation is applicable to BIPV modules that were installed in any orientation. The simulation results will be presented in sections 9.2 and 9.3.

9.2 SIMULATION RESULTS OF HEAT GAIN

In this section, the simulation results obtained from the models described in this thesis are presented. Using the SPVHG model developed in Chapter 5, together with the 1989 hourly weather data file of Hong Kong, the annual heat gains of the semi-transparent BIPV modules can be determined. Since the main contribution of this thesis is the development of the SPVHG model for assessing the thermal performance of the semi-transparent BIPV modules, the results of the total heat gains for different module's parameters are described and analyzed separately in sections 9.2.1 and 9.2.2. Then the total energy performances which take into account the power generation and the daylight utilization in addition to the heat gains of the modules are analyzed in section 9.3.

9.2.1 Hourly heat gain variations

The current and the following sections (section 9.2.1 and 9.2.2), focus on the semi-transparent BIPV modules in the PV façade. This section outlines and discusses, for a fixed area of the semi-transparent BIPV modules on the façade, the variation of the heat gain of different solar cell areas in the module. A ratio *R* is used to represent the area portion of the solar cell within the module. The hourly heat gain profiles of different R values are plotted to illustrate their differences. The solar irradiance and the heat gain profile of a clear glass with the same thickness as the module are also shown in the plots for comparison. Table 9.1 lists the properties of the PV façade and the semi-transparent module used in the heat gain simulation in this section:

Table 9.1 Properties of the semi-transparent BIPV module

Properties	Values
Area of the semi-transparent BIPV module:	11.52 m^2 (40% of the façade area)
Thickness of the module:	6mm
Rated efficiency of the solar cells:	16%
Conductivity of module glass:	0.75 W/mK
Absorptance of the solar cell:	0.77
Emittance of the module glass:	0.86
Refractive index of the module glass:	1.5

The heat gain through the module varies continuously throughout the whole day. Figure 9.3 shows an example of such a variation for a south-facing module in a clear day in September. The heat gain is the lowest at night when the solar radiation is absent. As the available solar radiation starts to increase in the morning, the heat gain

increases also until it reaches the maximum at around 13:00. Then it starts decreasing until it reaches the minimum when the available solar radiation is zero again.

Figure 9.4 is another example of the hourly variations of the heat gain. Unlike the day shown in Figure 9.3, the solar radiation on this day is weak. The maximum solar irradiance on this day is just higher than 150 W/m^2. Negative heat gains are obtained in early morning and late afternoon on this day. Positive heat gains in the graphs imply net heat is gained by the indoor air due to the solar radiation and the higher outdoor air temperature than that of indoors. In contrast, negative heat gains represent heat lost from indoors to outdoors. This occurs when solar radiation is weak and outdoor temperature is low.

According to Figure 9.3 and 9.4, smaller *R* value yields larger heat gain. Also, clear glass has larger heat gain. A detailed study of the effects of different *R* values to the heat gain will be presented in section 9.2.2.2.

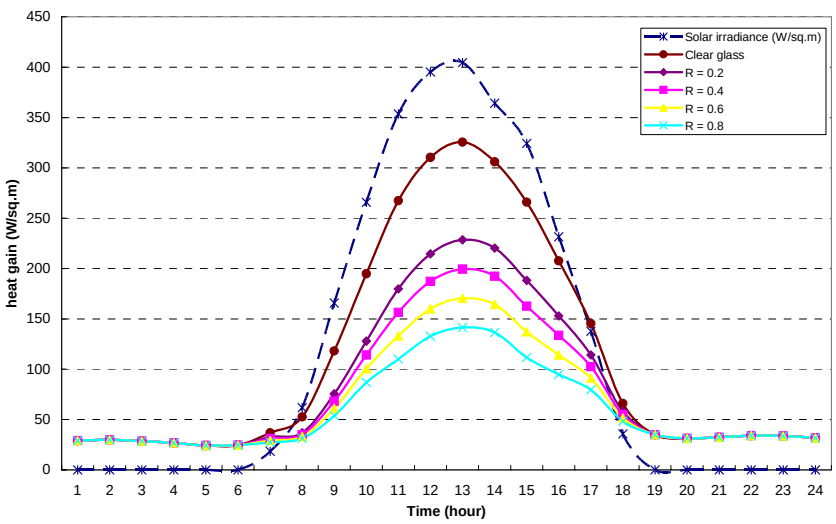

Figure 9.3 Heat gain of the semi-transparent BIPV module with different *R* in a day in September

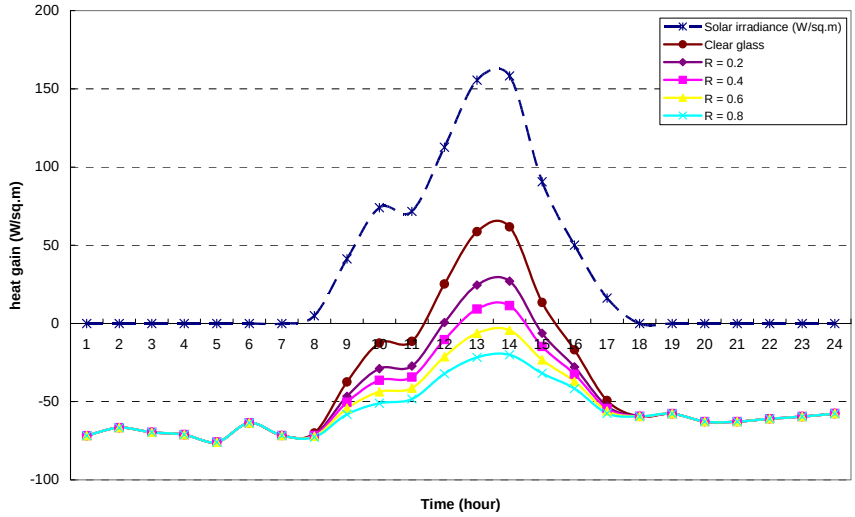

Figure 9.4 Heat gain of the semi-transparent BIPV module with different *R* in a day in January

9.2.2 Annual total heat gain

The annual total heat gain can be obtained by summing the hourly values. This section studies the effects of different parameters of the semi-transparent BIPV modules, which include the solar cell ratio (*R*), the orientations, the efficiency of the solar cells and the thickness of the modules. In the analysis, each of the parameters will be varied individually and the other three parameters will remain unchanged to investigate the sole effects of each parameter. The results are presented in the following four sections.

9.2.2.1 Effects of the orientation

Three typical orientations for solar energy utilization in buildings in Hong Kong are considered, namely east, south and west. North façade is not considered because the solar energy availability of this façade is low in Hong Kong according to the

studies described in Chapter 4.

Figure 9.5 shows the variation of the monthly heat gain for a 6mm thick semi-transparent BIPV module with solar cell efficiency of 16% and 60% solar cell area (R = 0.6). As illustrated in the figure, east-facing modules and west facing modules have the similar annual profiles of heat gain. The highest total heat gain of these two orientations occurs in summer while the lowest, which is negative, occurs in winter. Negative heat gain implies that the heat is lost from the indoors to outdoors. For the south-facing module, the largest total heat gain occurs in autumn and the lowest occurs in spring. No heat loss is obtained for this orientation. This indicates that the modules on this orientation have net heat gain throughout the year.

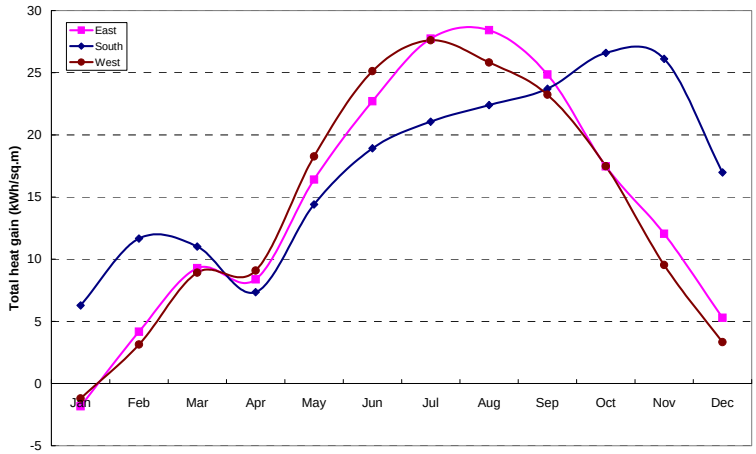

Figure 9.5 Monthly profile of the total heat gain of different orientations

Solar heat gain and conduction heat gain are the two components that contribute to the total heat gain of the BIPV module. These two components should be analyzed in order to explain the annual total heat gain patterns as shown in Figure 9.5. The conduction heat gain can be obtained by setting the solar radiation in the weather data file equal to zero when running the SPVHG model. The contribution of the solar heat

gain to the total heat gain is the difference between the latter and the conductive heat gain. Figure 9.6 and 9.7 show the monthly variation of the solar and conduction heat gain respectively. The conduction heat gain results are applicable to all orientations because they are obtained in the absence of solar radiation which is regardless of the orientation.

As shown in Figure 9.6, the highest solar heat gain occurs in summer for the east- and west-facing modules and that occurs in autumn for the south-facing module. Since the solar heat gain mainly depends on the solar radiation, these results imply that the east- and west-facing modules receive the most solar radiation in summer while the south-facing modules receive the most solar radiation in autumn. The patterns of the monthly solar heat gain for each orientation are similar to that of the corresponding total heat gain. This is because the solar heat gain takes up a significant portion in the total heat gain. According to the simulation results, more than 60% of the total heat gain is contributed by the solar heat gain for most of the months. In addition, net conduction heat loss is obtained in some months. As indicated in Figure 9.5, net heat loss is obtained from east- and west-facing module in January. This is due to the large conductive heat loss in January, which is illustrated in Figure 9.7. Although conductive heat loss also occurs in February, March and April, the loss is compensated by the solar heat gain and therefore a net heat gain is resulted in these three months.

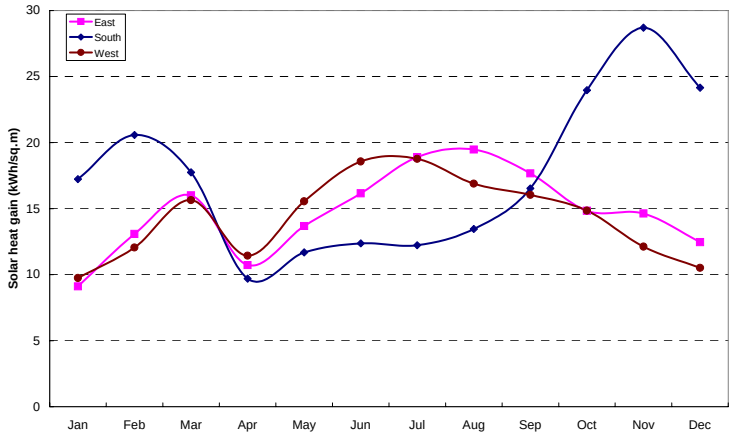

Figure 9.6 Monthly profile of the solar heat gain of different orientations

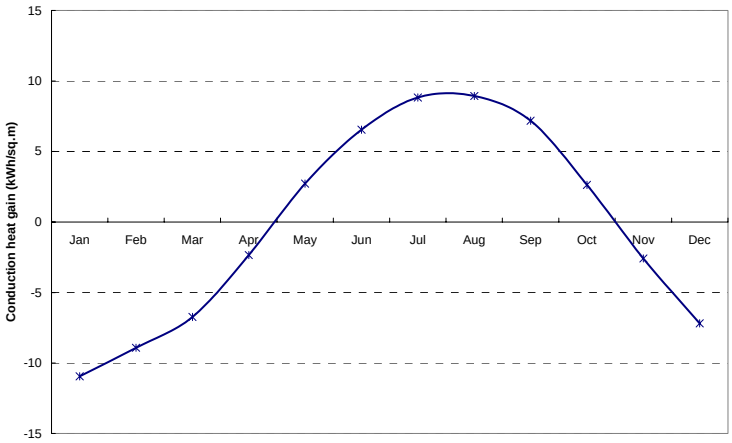

Figure 9.7 Monthly profile of the conduction heat gain

Other than the monthly profile of the heat gain, it is also important to investigate the annual total heat gain. The annual total heat gain is simply obtained by adding the monthly values. Figure 9.8 illustrates the annual total heat gain of the three orientations. The east- and west-facing modules have similar annual total heat gain, which are 174.9 kWh/m^2 and 170.3 kWh/m^2 respectively. The highest annual total heat gain occurs when the modules are oriented to the south, which is 206.5 kWh/m^2. These results are reasonable because the south surface receives the most solar

radiation among these three orientations according to the studies described in Chapter 4. The annual total heat gain of the east and west orientation is 15.3% and 17.5% less than that of the south orientation.

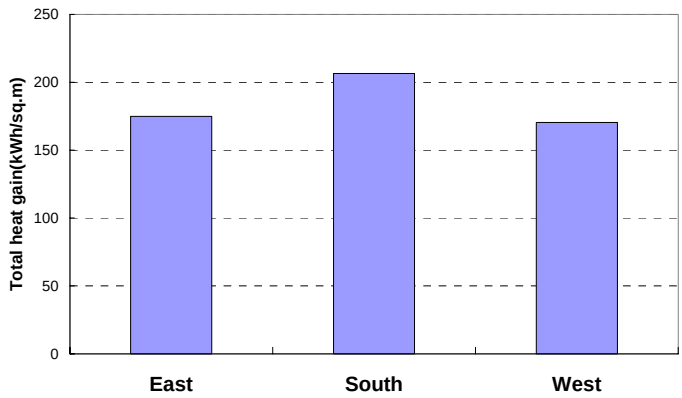

Figure 9.8 Annual total heat gain of different orientations

9.2.2.2 Effects of the solar cell area ratio, *R*

The solar cell area ratio has a significant impact on the total heat gain of the semi-transparent BIPV modules because it directly influences the amount of solar radiation that enters into indoor space and thus the solar heat gain is affected. This section investigates how the ratio affects the total heat gain.

Figure 9.9 to 9.11 show the profiles of the total heat gain through the modules when *R* equals to 0 (clear glass), 0.2, 0.4, 0.6 and 0.8 for each orientation. The ratio *R* does not affect the monthly total heat gain patterns much but the values. Since the total heat gain is dominated by the solar heat gain as mentioned in the last section, the increase in solar cell area will decrease the solar radiation from entering the indoors and therefore reduce the total heat gain.

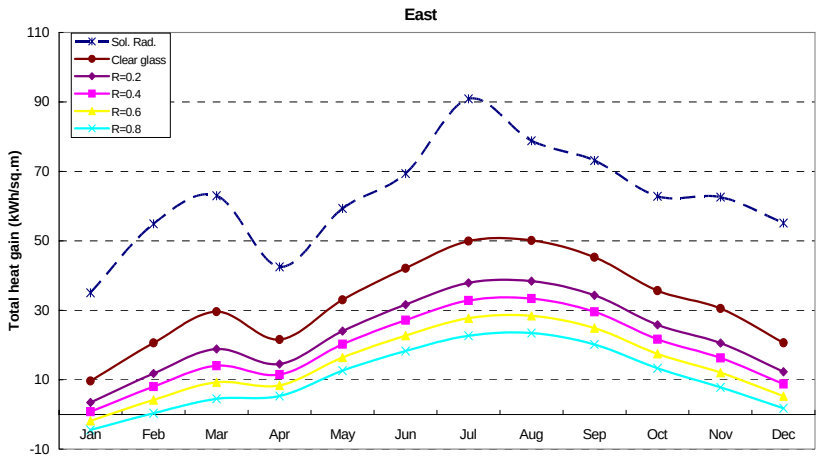

Figure 9.9 Monthly profile of the total heat gain of the BIPV module facing east with different *R*s

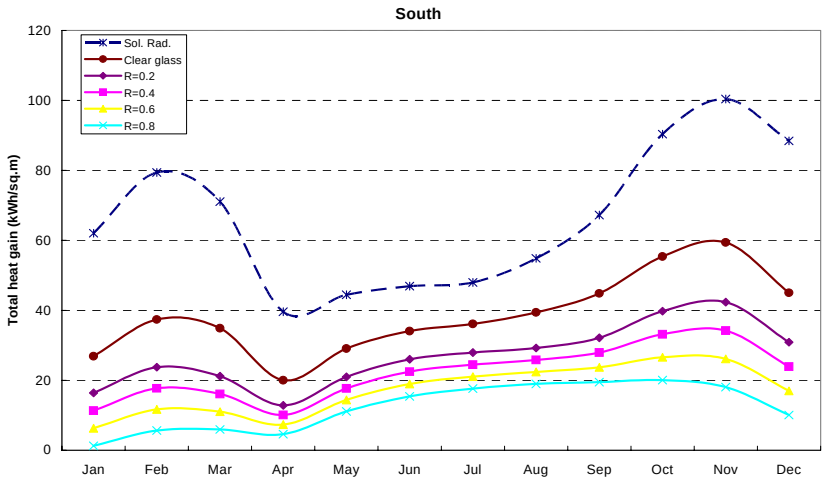

Figure 9.10 Monthly profile of the total heat gain of the BIPV module facing south with different *R*s

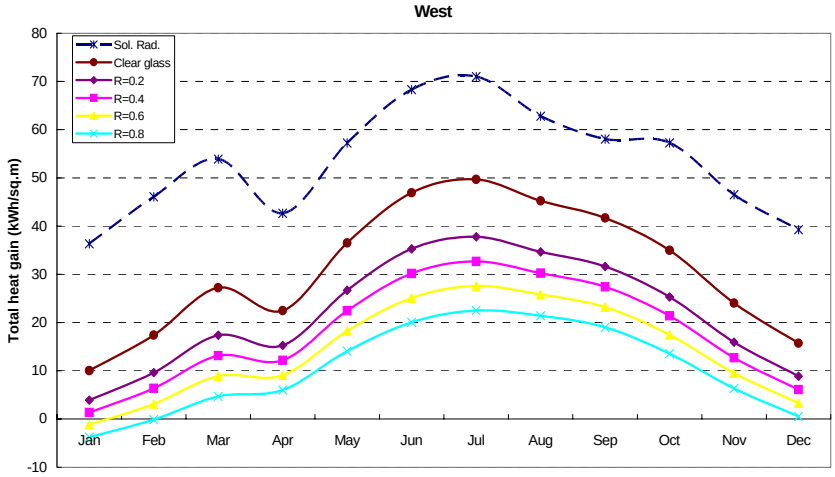

Figure 9.11 Monthly profile of the total heat gain of the BIPV module facing west with different *R*s

The annual total heat gain of the semi-transparent BIPV modules with different solar cell areas is also studied. Figure 9.12 shows the comparisons of annual total heat gain of the module with different *R*s on the three orientations. When compared with the clear glass, a significant reduction in the total heat gain is resulted by using the semi-transparent BIPV modules. The values and the percentage of reductions of the total heat gain of different *R*s compared with the clear glass are summarized in Table 9.2. The results show that a range of 30% to more than 60% of total heat gain can be reduced if a module of *R*=0.2 to 0.8 is used respectively.

The reasons for the significant reduction in heat gain by the solar cells are that larger solar cell area blocks more solar heat, and thus reduces the heat gain. In the heat transfer process, the heat absorbed by the solar cells, which have relatively small volume, is negligible. Therefore, solar heat dominates the heat gain through the PV modules, and thus the area of the solar cells directly influences the amount of heat gain.

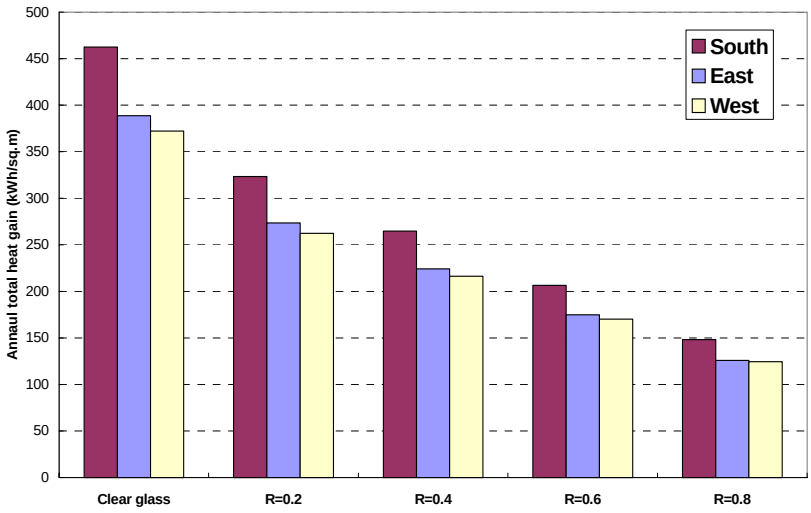

Figure 9.12 Annual total heat gain of different *R* and different orientations

Table 9.2 Summary of annual total heat gain and the corresponding percentage of reduction

		Clear glass	R = 0.2	R = 0.4	R = 0.6	R = 0.8
East	**Annual Total heat gain (kWh/m^2)**	388.7	273.5	224.1	174.9	125.7
	Percentage of reduction	-	29.6%	42.3%	55.0%	67.6%
South	**Annual Total heat gain (kWh/m^2)**	462.4	323.4	264.8	206.5	148.3
	Percentage of reduction	-	30.1%	42.7%	55.4%	67.9%
West	**Annual Total heat gain (kWh/m^2)**	372.1	262.4	216.3	170.3	124.5
	Percentage of reduction	-	29.5%	41.9%	54.2%	66.6%

9.2.2.3 Effects of the efficiency of the solar cells

The solar energy that is absorbed by a PV module is converted partly into thermal energy and partly into electrical energy which is removed from the solar cell

through an external electrical circuit. The amount of electrical energy that is converted by the solar cell depends on the electricity conversion efficiency, η_{el}, of the cell. Different kinds of solar cell material have different electricity conversion efficiencies. Take the three most commonly used solar cell materials as examples, the efficiencies of a mono-crystalline silicon cell, poly-crystalline silicon cell and amorphous silicon cell are respectively 18%, 16% and 10.5% (Sonnenenergie, 2005). Since different types of solar cell material will be used in semi-transparent BIPV systems in different applications, it is worth studying the influence of the efficiency on the heat gain through the module.

As the focus of this section is put on the solar cell's efficiency, the other three module's parameters (i.e. the solar cell area ratio *R*, the orientation and the module's thickness) are kept unchanged to facilitate a clear comparison. The cell efficiencies selected in the current study vary from 6% to 18%, which is the efficiency range of the PV modules that are commonly available in the market. The parameters used in the current study are listed in Table 9.3.

Table 9.3 Parameters used in the study of the effects of the solar cell efficiency

Parameters:	**Value**
Solar cell efficiencies:	6%, 8%, 10%, 12%, 14%, 16% and 18%
Solar cell area ratio (*R*):	0.6
Modules orientation:	South
Module's thickness:	6mm

The results of the heat gain variations due to different solar cell efficiencies are shown in Figure 9.13. It can be noticed from this figure that there is a linear

relationship between the cell efficiency and the annual total heat gain. As the cell efficiency decreases, the annual total heat gain decreases. However, the cell efficiency has only a limited effect on the annual total heat gain. As revealed by the simulation results, the annual total heat gain varies from 214.6 kWh/m^2 at 6% cell efficiency to 204.8 kWh/m^2 at 18% cell efficiency, which is only a change of 4.56%. The following linear relationship between the annual total heat gain and the cell efficiency can be written according to the results shown in Figure 9.13:

$$y = -0.8167x + 219.5 \tag{9.7}$$

where x and y represent the cell efficiency and the annual total heat gain respectively. Assuming the efficiency of the solar cell can reach 100%, the annual total heat gain resulted is 137.8 kWh/m^2 according to equation (9.7). This only corresponds to a 35.8% reduction of annual total heat gain when compared with the case of 6% cell efficiency. This result shows that the solar cell efficiency has a relatively insignificant effect on the heat gain of the module.

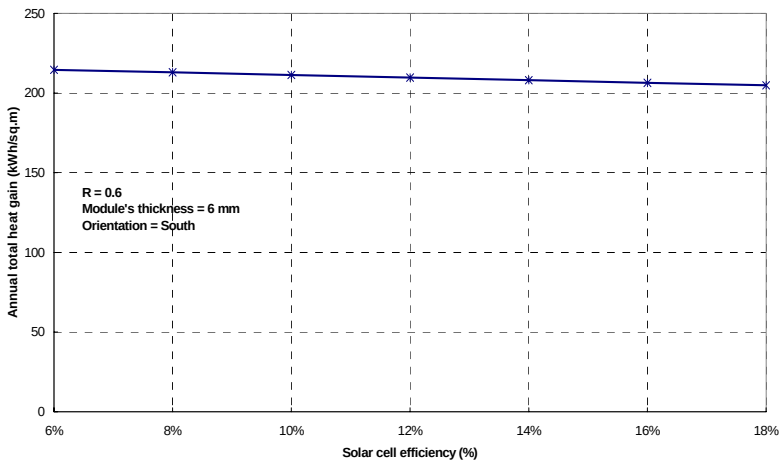

Figure 9.13 The variation of the annual total heat gain with different solar cell efficiecnies

The insignificant effect of the solar cell efficiency on the module heat gain can be attributed to the structure of the module. Since the volume of the solar cell in the module is negligibly small compared with that of the glass layers, the heat absorbed by the solar cell is also negligible. As a result, the parameters of the solar cell such as its efficiency do not affect the heat gain much.

After concentrating on the solar cell efficiency, now let's turn to the last module's parameter, the module thickness, for its effect on the heat gain.

9.2.2.4 Effects of the module thickness

As the semi-transparent BIPV modules can be integrated into a building as an external façade or a window glass, the thickness of the module used in various situations is different. For example, if the module is used on the outer façade, thicker or tempered glass that in the order of 20mm or more may be needed for bearing the loads in the external environment. However, thinner glass of about 6mm can be allowed if the module is used to replace window glass. The thickness of the module is also an important parameter which affects the heat gain.

As mentioned in section 5.1, the semi-transparent BIPV module comprises two glass layers and a solar cell layer. The thickness of the whole module depends on the thickness of the two glass layers because the thickness of the solar cell is negligibly small. Different thicknesses of the module are input to the SPVHG model to calculate the annual heat gain through the module. The thicknesses that have been studied are 6mm, 12mm, 18mm and 24mm. These thicknesses were selected because they are commonly used in practice. In order to perform a clear comparison on different module thicknesses, the other parameters of the module (i.e. the solar cell area ratio *R*,

the orientation and the solar cell efficiency) remain unchanged in the simulation. Table 9.4 shows the parameters used in the study of current section.

Table 9.4 Parameters used in the study of the effects of the module thickness

Parameters:	**Value**
Module's thickness:	6mm, 12mm, 18mm and 24mm
Solar cell area ratio (*R*):	0.6
Modules orientation:	South
Solar cell efficiencies:	16%

Figure 9.14 shows the simulation results of the effect of the module thickness on the annual total heat gain. As shown in the figure, the annual total heat gain drops as a thicker module is used. However, the reduction is not very significant. The annual total heat gain reduces from 206.4 kWh/m^2 to 175.3 kWh/m^2 when the module thickness increases from 6mm to 24mm, which correspond to a 15.11% reduction.

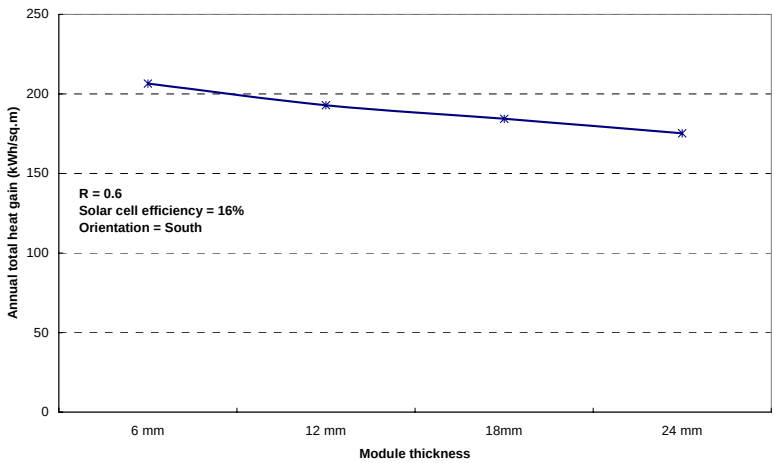

Figure 9.14 The variation of the annual total heat gain with different module thicknesses

As the module thickness increase, the thermal resistance also increases and thus the conduction heat gain is reduced. The annual variation of conduction heat gain of PV modules with different thicknesses is shown in Figure 9.15. According to the figure, the values of conduction heat gain of different module thicknesses are similar. Although thinner modules have higher conductive heat gain and heat loss, especially in the seasons when the indoor and outdoor air temperature difference is larger such as summer and winter, the differences between each thickness are not significant. Therefore, the change in total heat gain is not significant because the variation of conduction heat gain is small.

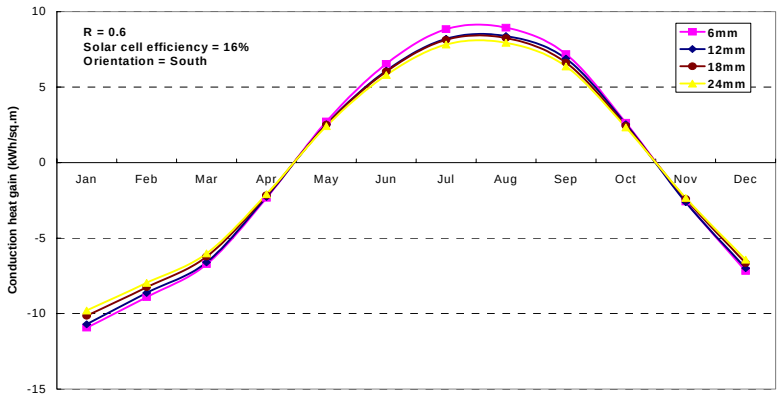

Figure 9.15 Monthly profile of the conduction heat gain for different module thicknesses

This section has analyzed the thermal performance of the semi-transparent BIPV module. The simulation results of the daily and annual variations of the heat gain through the module have been presented and discussed. The effects of different module's parameters have also been analyzed. However, the discussions in this section only focus on the thermal performance of the module. In order to obtain a comprehensive conclusion on the energy performance of the semi-transparent BIPV

module, a study which considers the power generated from the modules and daylight utilization of the whole façade of the simulated room are performed. The details of the study are presented in the next section.

9.3 SIMULATION RESULTS OF TOTAL ENERGY PERFORMANCE

In this section, the energy performance of the BIPV façade of the room that is shown in Figure 9.1 is studied. The façade of that room comprises both opaque and semi-transparent BIPV modules. In addition to the thermal performance as discussed in the last section, energy generation of the PV modules and the energy consumption due to the daylight through the semi-transparent BIPV module are considered. The net energy benefit of the whole façade is then evaluated in terms of electricity consumption.

The energy impact of the whole BIPV façade comprises the following components: (i) the electricity saving of the air-conditioning (A/C) system due to the heat gain reduction of using the semi-transparent BIPV modules, and (ii) the electricity generation of all the BIPV modules on the façade, and (iii) the electricity consumption increase of the artificial lighting after considering the daylight utilization. The net electricity benefit is the sum of the first two components and deducting the third component. The approaches for assessing these three components have been discussed in the previous sections or chapters. The first component involves both the

heat gain from the semi-transparent BIPV modules and the PV cladding. The heat gain from the semi-transparent BIPV modules can be evaluated by the SPVHG model while the heat gain from the PV cladding can be determined by the method described in section 9.1.2. Then the electricity consumption of the air-conditioning system due to the heat gains can be evaluated by the approach stated in section 9.1.3. The methods that have been described in Chapter 6 and 7 are used for assessing the components (ii) and (iii) respectively. The net electricity benefit is calculated by combining the electricity saving or contribution from the three components per unit façade area. The basic inputs described in section 9.3.1 are used in the simulation of energy benefit of the whole PV façade.

9.3.1 Basic inputs

9.3.1.1 General assumptions

In order to make the results more comprehensive, the façades of different window-to-wall (*WWR*) ratios are studied. The *WWR* ratio in the current study is referring to the ratio of the PV window area to the PV cladding area. Six cases of different *WWR* ratios ranging from 0.2 to 0.7 are simulated. In each case, different solar cell ratios *R* and orientations are compared. Since the effect of the module thickness and the solar cell efficiency is not significant according to the discussions in the previous sections, no comparison is made on these two parameters in this section and therefore they are kept unchanged in all cases. The thickness and the solar cell efficiency of the module selected in the simulation are 6mm and 16% respectively. Some other assumptions have been made in the calculations of each electricity benefit

components, which are discussed in the following three sections.

9.3.1.2 Energy consumption of the air-conditioning system

The method for calculating the energy consumption of the air-conditioning system due to the heat gain from the façade has been described in section 9.1.3. According to equation (9.6), the *COP* of the chiller is required for estimating the energy consumption of the air-conditioning system. The *COP* is related to the heat rejection method of the chiller. Based on the study conducted by Yik et al. (2001), the *COP* of the four common heat rejection methods are 2.8 for air-cooled systems, 4.7 for water-cooled systems with cooling towers and for indirect seawater-cooled systems, and 5.2 for direct seawater-cooled systems. The most common air-cooled system is assumed in the current study.

Since the room used in the simulation is situated in an office building, the operating schedule of the air-conditioning systems is based on the typical schedule of an office building which is listed in Table 9.5.

As the objective of the current simulation is to study the energy performance of the PV façade, only the façade heat gain is considered in the calculation of cooling load in the study. Other heat sources in the building such as the people, artificial lighting, miscellaneous equipment and infiltration air are excluded because they do not affect the façade heat gain. The assumptions made in the calculations of the energy consumption of the air-conditioning system are listed in Table 9.5.

Table 9.5 Assumptions in the A/C energy calculations

COP of the A/C system:	2.8
Wall surface absorptance:	0.9
Operating schedule of the A/C system:	
Weekdays	08:00 – 20:00
Saturday	08:00 – 13:00
Sunday and Public holidays	N/A

9.3.1.3 Power generation by the PV modules

Opaque PV modules are installed on the upper and lower part of the room façade as shown in Figure 9.1. Two types of mono-crystalline PV module with different dimensions and electrical characteristics are assumed to be fitted on the façade according to the wall area under different window-to-wall ratios. The specifications of these two kinds of PV module are summarized in Table 9.6. With these specifications, the power production of the opaque PV modules can be estimated according to equation (6.10).

Table 9.6 Specifications of the PV modules

Type 1:		**Type 2:**	
P_{max}:	175 W	**P_{max}:**	85 W
I_{sc}:	5.4 A	**I_{sc}:**	5.4 A
V_{oc}:	44 V	**V_{oc}:**	22 V
Height:	1593 mm	**Height:**	1210 mm
Width:	790 mm	**Width:**	537 mm

9.3.1.4 Energy consumption of artificial lighting

The PV windows are located in the middle of the façade as shown in Figure 9.1. Daylight enters the indoors through the transparent part of the PV window and reaches the working plane. The average illuminance on the working plane due to the daylight can be determined by the approaches described in Chapter 7. Assuming that an ideal continuous dimming system is adopted in the artificial light of the office room, if the illuminance provided by the daylight is not sufficient to reach the illuminance requirement, the remaining illuminance is provided by the artificial light. The illuminance requirement is assumed to be 500 *lux* for office (CIBSE, 1994; IESNA, 2000). Other parameters used in the calculation of the indoor daylight illuminance are summarized in Table 9.7.

Table 9.7 Parameters in the calculations of energy consumption of artificial lighting

Height of working plane above floor:	0.75 m
Illuminance requirement of working plane:	500 lux
Luminous efficacy of the artificial light:	100 lm/W
Light loss factor (LLF):	0.9
Coefficient of utilization (CU):	0.5
Reflectance of room surfaces:	
Ceiling	0.7
Wall	0.5
Ground	0.2
Working plane	0.1
Window wall reflectance:	0.4

9.3.2 Simulation results

Each of the three components of energy impact including the electricity production by the PV modules, electricity saving of A/C system and additional lighting power required is evaluated separately and the results are then combined to obtain the net electricity benefit. Prior to presenting the combined electricity benefits, the components of electricity benefit are shown for different solar cell area ratios and window-to-wall ratios. Figure 9.16 to 9.21 show the electricity impact breakdowns per façade area for a south facing façade with window-to-wall ratio equals 0.2 to 0.7. Since the patterns of the breakdown are similar for each orientation, only the results of south facing façade are shown. The results of the net electricity benefit of different facades are presented later. The highest part of the bars in Figures 9.16 to 9.21 represents the total electricity produced by the BIPV modules on the façade, including those of the PV cladding and PV window. The middle portion is the electricity saving of the air-conditioning system due to heat gain when using the PV window, compared with the ordinary clear glass window. The lowest part is the electricity consumption of the artificial lighting required to provide additional illuminance on the top of daylight when compared with the case of the ordinary clear glass window. This part is negative because it is electricity consumption instead of benefit.

According to Figure 9.16, when the window area is small, the power generated by the BIPV modules dominates the resultant electricity benefit. However, as the window area increases, such as the case shown in Figure 9.17, the electricity saving from the A/C system due to façade heat gain becomes significant on the resultant electricity benefit. The additional lighting power demand does not take a major

portion of the resultant electricity benefit, especially when the window area is large. As can be observed from the graphs, the power produced by the BIPV modules is able to cover the additional lighting power demands.

The nine different solar cell area ratios, *R*, from 0.1 to 1, are simulated for each *WWR*. The implication of *R* equals 1 is that the whole PV window area is filled with solar cells. This design is not practical because it cannot fulfill the functional requirement of the PV window to generate electricity and to provide transparent area. The simulation results when *R* equals 1 are for illustration propose only.

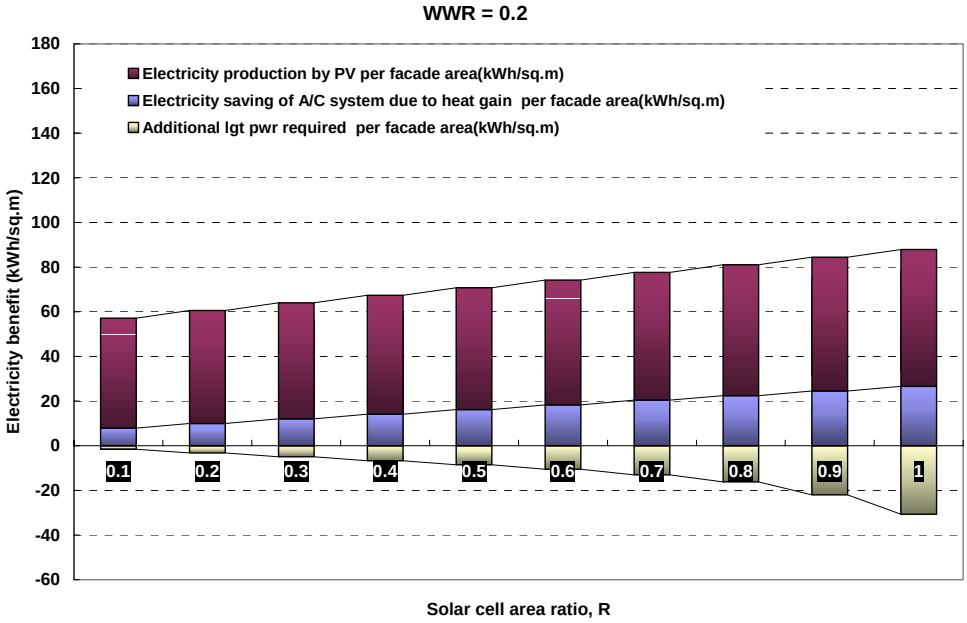

Figure 9.16 Electricity benefit breakdown of a south facing PV façade, *WWR* = 0.2

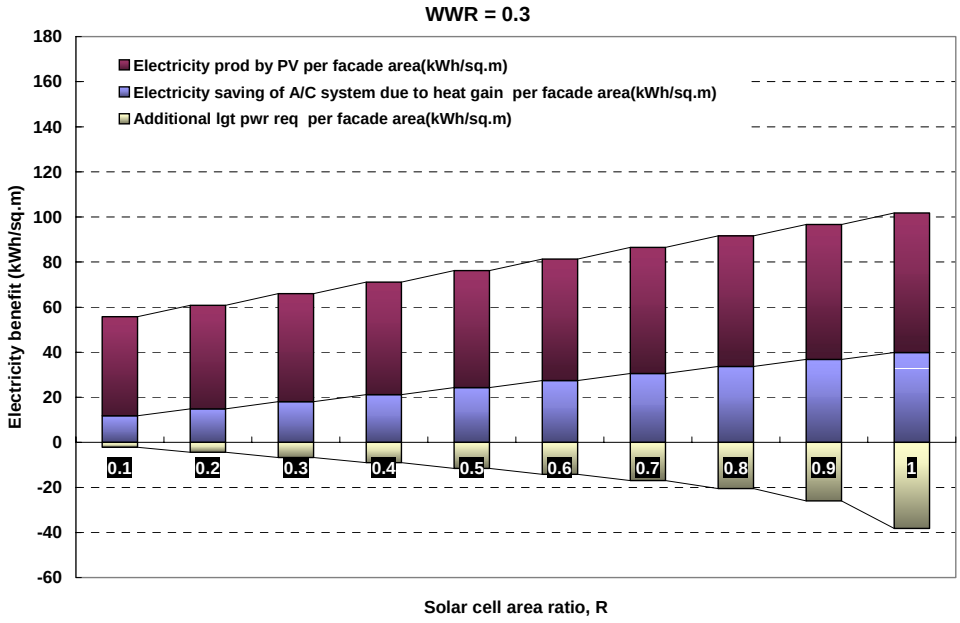

Figure 9.17 Electricity benefit breakdown of a south facing PV façade, *WWR* = 0.3

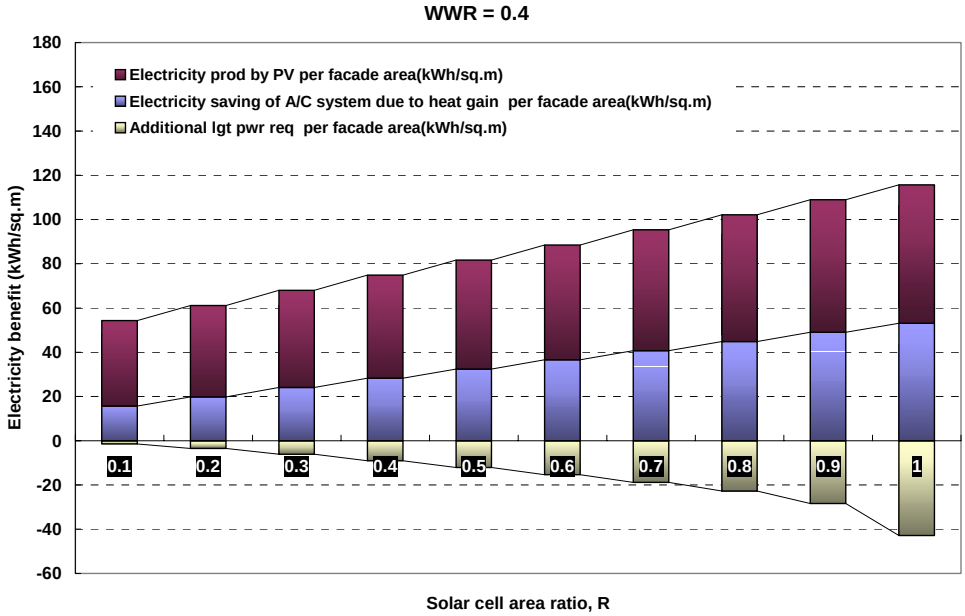

Figure 9.18 Electricity benefit breakdown of a south facing PV façade, *WWR* = 0.4

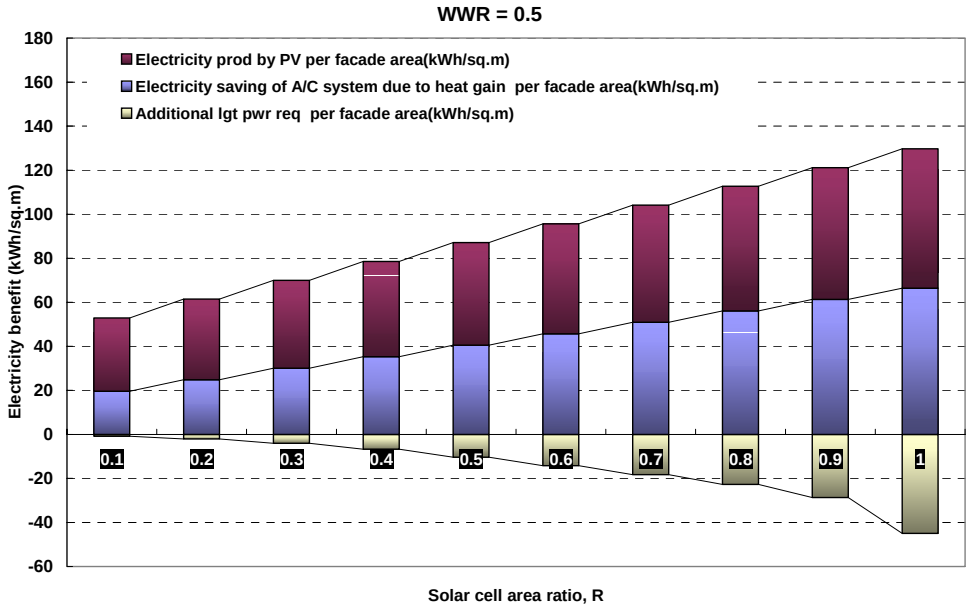

Figure 9.19 Electricity benefit breakdown of a south facing PV façade, *WWR* = 0.5

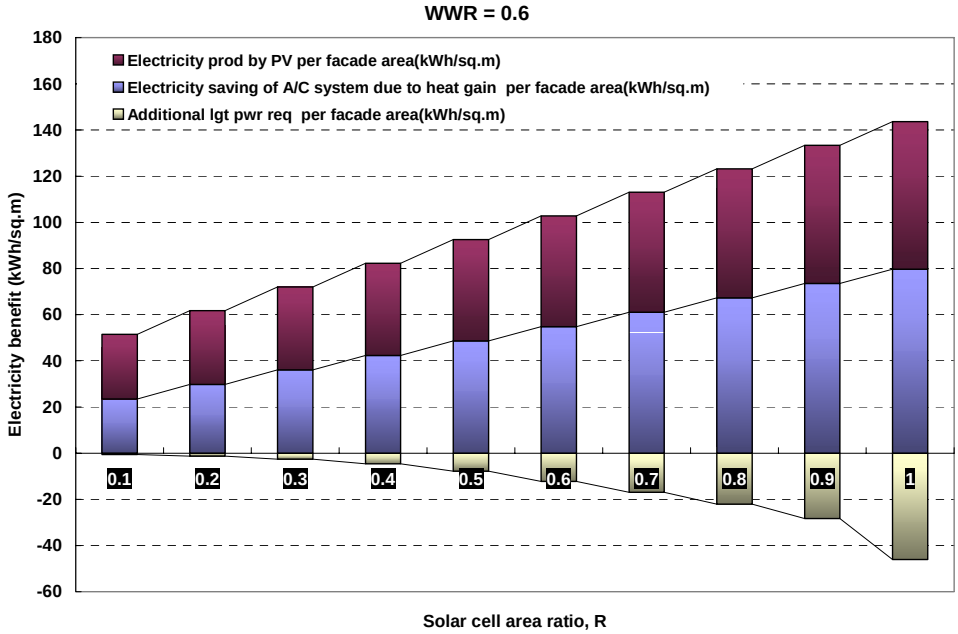

Figure 9.20 Electricity benefit breakdown of a south facing PV façade, *WWR* = 0.6

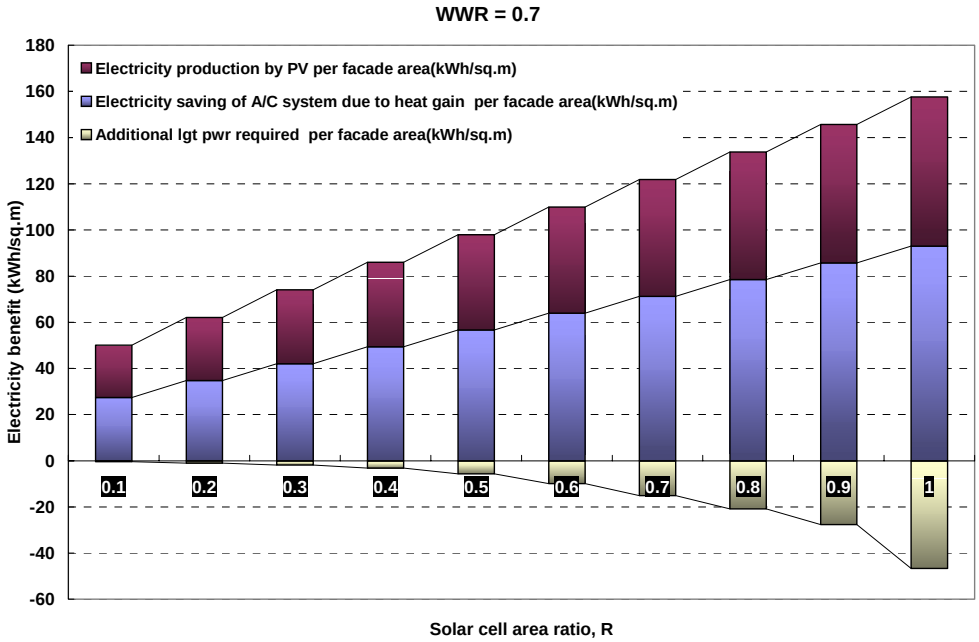

Figure 9.21 Electricity benefit breakdown of a south facing PV façade, *WWR* = 0.7

The net electricity benefit of the PV façade is also evaluated. It is determined by combining the three energy benefit components. The results of the net electricity benefit of the east, south and west facing façade are presented in Figure 9.22 to 9.24 respectively. It can be seen from the figures that the variation trend of all orientations are similar. The smallest net electricity benefit occurs when *R* is 0.1 for all *WWR*. As *R* increases, the net electricity benefit also increases and reaches a peak at *R* = 0.9 for large *WWR* equals 0.4 to 0.7. However, this is followed by a decline when *R* equals 1. For small *WWR* less than 0.4, the highest net electricity benefit occurs when *R* is 0.7 or 0.8 (depends on the *WWR*). These results indicate that a PV window with larger solar cell area (i.e. larger *R*) performs better in terms of energy efficiency. This is because the energy saving due to the reduction in heat gain and electricity generation by the solar cells is much more than the additional lighting demand. However, when *R* approaches 1, the net benefit drops because the lighting power increases sharply. According to the simulation results, the following optimum solar cell area ratio *R* can be concluded: a) When the *WWR* is smaller than 0.5, the optimum *R* is about 0.7; b) When the *WWR* is larger than or equal to 0.5, the optimum *R* is about 0.9.

As expected, the south facing façade has the largest net electricity benefit, east façade is the second largest and the least is the west façade. The highest net electricity benefit of the PV façade under the simulation conditions is near 120 kWh/m^2, which occurs in the south façade with *R*=0.9 and *WWR*=0.7.

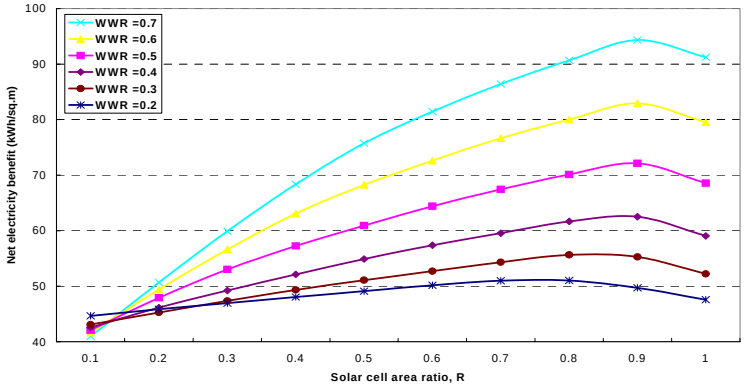

Figure 9.22 Net electricity benefit of a east facing PV facade

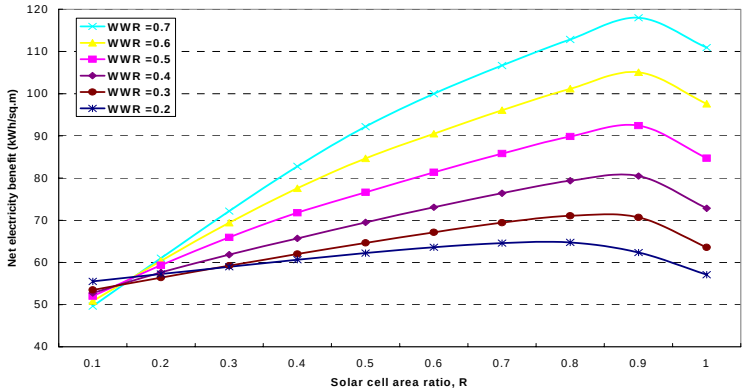

Figure 9.23 Net electricity benefit of a south facing PV facade

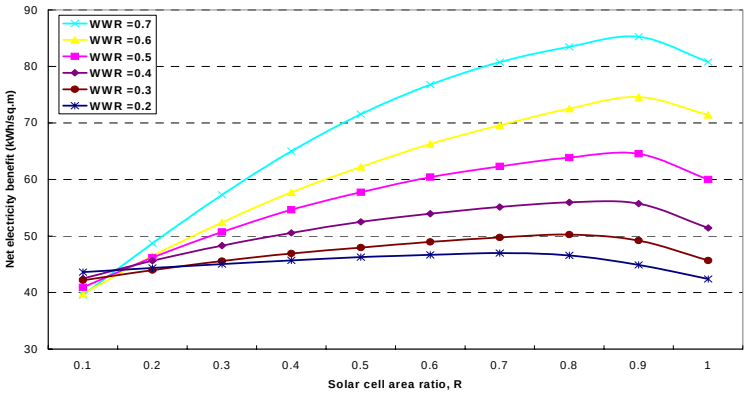

Figure 9.24 Net electricity benefit of a west facing PV facade

9.4 SUMMARY

In this chapter, the use of the SPVHG model developed in Chapter 5 has been demonstrated for evaluating the heat gain through semi-transparent BIPV modules. The effects of different module parameters on the heat gain have been investigated. A study on a PV façade in a building which includes both opaque and semi-transparent BIPV modules has been presented to illustrate the energy performance of the modules.

The simulation results indicate that solar heat gain takes up the significant portion of the total heat gain of the semi-transparent BIPV modules. The variation of the heat gain follows the pattern of the solar radiation change. Different orientations of the module yield different total heat gains because the solar radiation received on different orientations varies. The highest annual total heat gain is resulted when the module faces south. The annual total heat gains of the east and west orientated modules are 15.3% and 17.5% less than the south facing modules respectively.

The solar cell area, R, in the semi-transparent BIPV module has significant effects on the heat gain according to the simulation results. When compared with ordinary clear glass, the use of the semi-transparent BIPV modules in windows can reduce around 30% of total heat gain annually if the solar cells cover 20% of the total area of the module (R = 0.2). Also, more than 60% of total heat gain can be reduced in a year if R is 0.8. This shows the significance of heat gain reduction of the semi-transparent BIPV modules.

In contrast, as revealed by the simulation results, the changes in solar cell efficiency bring negligible effect on the heat gain of the semi-transparent BIPV

modules. Only a drop of 4.56% in total heat gain when the solar cell efficiency varies from 6% to 18% (which is the most common range of solar cell efficiency in practice). This is because the volume of the solar cell in the PV modules is too small to consider for their heat absorption.

The change in PV module thickness also has small influence on the heat gain of the semi-transparent BIPV modules. A reduction of 15.11% in total heat gain is obtained when the PV module thickness changes from 6mm to 24mm. The relatively small effect of the thickness on heat gain is due to the small variation in conduction heat gain through the PV modules.

The energy performance of the PV façade of a room in an office building is also studied. The power generation by the BIPV modules and the daylight utilization are also considered in the study. Different window-to-wall ratios and solar cell area ratios of the PV façade are compared for their electricity benefits. The results show that the optimum solar cell area ratio in the PV window ranges from 0.7 to 0.9, depending on the window-to-wall ratio. The largest net electricity benefit of the PV façade under the simulation conditions is near 120 kWh/m^2.

This chapter has illustrated the application of the SPVHG model developed in this thesis. Different applications of semi-transparent BIPV modules are simulated by the model. The results show a great energy saving potential of using the semi-transparent BIPV modules in buildings.

CHAPTER 10

CONCLUSIONS AND RECOMMENDATIONS FOR FUTURE RESEARCH

This chapter draws conclusions on the simulation and experimental studies of the energy performance of the semi-transparent BIPV module, and summarizes the energy performance of different arrangement of PV modules on a PV façade in typical Hong Kong buildings. Topics for further study are also suggested in this chapter.

Semi-transparent BIPV modules have been widely used in building façade in all over the world. This kind of PV module can also be found in a number of major buildings in Hong Kong. Producing electricity by the use of solar energy is the main advantage of this kind of PV modules. However, as the modules are used on the building facades, their characteristics of heat transfer and daylight utilization also have critical effect on the building energy consumption. Although the application of this kind of PV modules is becoming increasingly common, little research has been conducted on their thermal and energy performance. This thesis aims at developing a method to evaluate the heat gain through this kind of PV modules. Models for simulating the power generation of the PV modules and for calculating the indoor illuminance have been developed. In addition, the optimum inclination of solar collecting surfaces has been studied. As a result, the total energy performance of the PV modules can be evaluated by using the models.

The amount of solar energy that reaches the modules' surfaces is essential in the

assessment of the energy performance of the PV modules. Therefore, the different solar radiation models of solar radiation level on inclined surface have been investigated. The optimum orientation and inclination have been evaluated by comparing four well-known diffuse solar radiation models. It has been found from on-site measurement that the Reindl and the Perez models perform the best for predicting the solar radiation on inclined surfaces of different orientations. Regarding the vertical façades, southeast and south receive the most solar radiation in a year among all orientations. The optimum tilted angle for these two orientations are 19° and 20° respectively. The results indicate that the optimum inclination is not necessarily the same as the local latitude (22.3°). The possible reason is that more sunny days and stronger solar radiation are available in the summer than in the winter in Hong Kong. The optimum tilted angle should be such that it suits better the summer conditions in Hong Kong in order to maximize the solar radiation availability in a year.

By incorporating with the solar radiation model, a one-dimensional transient energy model, the SPVHG model, has been developed in this thesis for modeling the heat gain through the semi-transparent BIPV modules under unsteady state ambient conditions. Since the solar radiation models have been included in the SPVHG model, the SPVHG model is applicable to inclined surfaces of different orientations. By using the SPVHG model, the heat gain of the module throughout a year have been determined. Different parameters of the module such as orientation, solar cell area, solar cell efficiency and module thickness have been investigated for their impacts on the heat gains by using the SPVHG model.

Since the SPVHG model involve continuous iteration, a computer program has

been written by using Visual C++ for executing the SPVHG model. The annual heat gain of the semi-transparent BIPV module with different characteristics can therefore be evaluated and analyzed. The amount of heat gain is anticipated to be less if the solar cell area of the module increases. This hypothesis is supported by the simulation results. When compared with ordinary clear glass, around 30% and 60% of annual total heat gain can be reduced if the solar cells cover 20% and 80% of the total area of the PV modules respectively (R = 0.2 and 0.8). This shows the significant effect of the solar cell area of the module on heat gain. These results are important because they show the significance for using semi-transparent BIPV modules in heat gain reduction.

However, the changes in module thickness and solar cell efficiency do not significantly influence the heat gain of the PV modules. According to the simulation results, the amount of heat gain has a 15.11% drop when the module thickness is increased from 6mm to 24mm. The reduction of heat gain is mainly owing to the increase of conduction heat gain of the PV modules. However, the effect of thickness on the conduction heat gain is not significant. Therefore, the change in the amount of total heat gain is not substantial when the module thickness is changed. When the solar cell efficiency increases from 6% to 18%, a negligible drop of 4.56% in heat gain is obtained. These results indicate that both the PV module thickness and solar cell efficiency have insignificantly effects on the heat gain of the PV modules because these two parameters have only minor effect on the solar heat gain, which dominant the total heat gain.

The reduction in heat gain can save energy for the air-conditioning systems. Other than this energy saving feature, the semi-transparent BIPV module has another

energy benefit: producing electricity under solar radiation. However, the solar cells of the PV modules block the daylight at the same time. When considering the heat gain performance together with the electricity generation and daylight utilization of the semi-transparent BIPV module, it is recommended that more solar cells can be installed in the modules. This is because, with more solar cells in the PV modules, the electricity benefits due to the energy saving in air-conditioning systems and the electricity generation of the PV modules are higher than the energy consumption of the artificial lighting. The optimum solar cell area ratio in the module is 0.7 to 0.9 depending on the window-to-wall ratio. The largest net electricity benefit of the PV façade under the simulation conditions is near 120 kWh/m^2.

In addition to the theoretical aspect, experimental studies have been conducted to show the reliability of the theoretical model. The simulation results are reasonably close to the experimental results. The errors between the calculated and measured PV module surface temperatures are less than 3% for all solar irradiation in the experiments. However, discrepancies appear in some cases in the net heat gain comparisons. The disagreements between the calculated and measured heat gains are because of the uncertainties of the measuring devices and the equipment limitation. To achieve greater accuracy in the experiment, controlling the water flow rate in a more precise way to allow a larger water temperature difference across the cooling coil is suggested. On the whole, the errors of the heat gain test are less than 5% in the cases when the water temperature differences are large enough. Therefore, the experimental results generally validate the simulation model.

In conclusion, the SPVHG model developed in this study is a useful tool for assessing the heat gain of the semi-transparent BIPV modules as to date few studies

have considered the module's characteristics in detail for assessing their heat gain. The model helps engineers and designers to have better understanding of the thermal performance of the PV modules with different parameters, so that they can utilize the model to achieve an energy efficient design.

A possible development of the SPVHG model would be the inclusion of shading systems because the shading systems would reduce the amount of solar energy that reaches the BIPV modules. The power generation and the indoor daylight level would be influenced by the shading systems. In addition, the simplified estimation of the cooling load and energy required by the air-conditioning systems used in the current simulation could be further developed to allow more detailed overall PV façade optimization studies. For example, the thermal performance of window frames and double glazing could be included in the model. Finally, the SPVHG model could be incorporated into the existing building energy simulation software packages, so that the semi-transparent BIPV modules would be one of the options in the glass type of the simulation to make the software more comprehensive.

REFERENCES

Ahmad, G. E., Hussein, H. M. S., El-Ghetany, H. H., 2003. Theoretical analysis and experimental verification of PV moduels, *Renewable Energy*, Vol. 28, pp.1159-1168.

Akbaba, M, and Alattawi, M. A. A., 1995. A new model for I-V characteristic of solar cell generators and its applications, *Solar Energy Materials and Solar Cells*, Vol. 37, pp 123-132.

Alvarez, G., Flores, J.J., Estrada, C.A., 1998. The thermal response of laminated glass with solar control coating, *J. Phys. D: Appl. Phys.*, Vol. 31, pp. 3057-3065

Alvarez, G., Palacios, M. J. and Flores, J. J., 2000. A test method to evaluate the thermal performance of window glazings, *Applied Thermal Engineering*, Vol. 20, pp. 803-812.

Arasteh, D. K., Reily, M. S., Rubin, M. D., 1989. A versatile procedure for calculating heat transfer through window, *ASHRAE Transaction*, Vol. 95, pt. 2, pp. 755-765.

ASHRAE, 2001. *ASHRAE Handbook 2001 Fundamentals*, American Society of Heating, Refrigerating and Air-Conditioning Engineers, Inc., USA.

Asl-Soleimani, E., Farhangi, S., Zabihi, M. S., 2001. The Effect of Tilt Angle, Air Pollution on Performance of Photovoltaic Systems in Tehran. *Renewable Energy*, Vol. 24, pp.459-468.

ASTM C1199 – 2000, *Standard test method for measuring the steady-state thermal transmittance of fenestration systems using hot box methods*, American Society for Testing and Materials.

Athienitis, A. K. and Tzempelikos, A., 2002. A methodology for simulation of daylight room illuminance distribution and light dimming for a room with a controlled shading device, *Solar Energy*, Vol. 72, no. 4, pp. 271-281.

Bari, S., Optimum slope angle and orientation of solar collectors for different periods of possible utilization, 2000. *Energy Conversion & Management*, Vol. 41, pp. 855-860.

Bhargava, B., 2001. Overview of photovoltaic technologies in India, *Solar Energy Materials & Solar Cells*, Vol. 67, pp. 639-646.

Boer, B. J. de, Helden, W. G.. J. van, 2001. PV-MOBI – PV modules optimized for building integration, In *9th International Conference on Solar Energy in High Lattitudes, Northsun 2001*, Leiden, The Netherlands.

Boyle, G., (Eds.), 2004. *Renewable Energy: power for a sustainable future*, 2nd Eds, Oxford University Press, United Kingdom.

BP Solar, 2005. *Statistical Review of World Energy 2005*, [Online] Available at: http://www.bp.com/downloads.do?categoryId=9003093&contentId=7005944

Brandemuehl, M. J. and Beckman, W. A., 1980. Transmission of diffuse radiation through CPC and flat plate collector glazings, *Solar Energy*, Vol. 24, pp. 511-513.

Brinkworth, B. J. et al., 1997. Thermal regulation of photovoltaic cladding, *Solar Energy*, Vol. 61, no. 3, pp. 169-178.

Brinkworth, B.J., Marshall, R.H., Ibarahim, Z., 2000. A validated model of naturally ventilated PV cladding, *Solar Energy*, Vol. 69, no. 1, pp. 67-81.

BS 874-3.1: 1987, *Methods for determining thermal insulating properties – Part 3: Tests for thermal transmittance and conductance – Section 3.1 Guarded hot-box method*, British Standard.

BS 874-3.2: 1990, *Methods for determining thermal insulating properties – Part 3: Tests for thermal transmittance and conductance – Section 3.2 Calibrated hot-box method*, British Standard.

Burlon, R., Bivona, S., Leone, C., 1991. Instantaneous hourly and daily radiation on tilted surfaces, *Solar Energy*, Vol. 47, no. 2, pp. 83-89.

CIBSE, 1994., *Code for interior lighting*, The Chartered Institution of Building Services Engineers, London.

Clarke, J. A., 2001. *Energy simulation in building design*, second ed. Butterworth-Heinemann, Oxford.

Cox, C.H. and Raghuraman, P., 1985. Design considerations for flat-plate-photovoltaic/thermal collectors, *Solar Energy*, Vol. 35, no. 3, pp. 227-241.

Curcija, D. and Goss, W. P., 1994. Two-dimensional Finite-element model of heat transfer in complete fenestration systems, *ASHRAE Transaction*, Vol. 100, pt. 2, pp. 1207-1221.

Curcija, D., Goss, W.P., New correlations for convective heat transfer coefficient on indoor fenestration surfaces-compilation of more recent work, *Proceedings of Thermal Performance of the Exterior Envelopes of Buildings VI*, December 1995, Florida, USA, pp. 567-572.

Diasty, R. E., 1998. Variable positioning of the sun using time duration, *Renewable Energy*, Vol. 14, no. 1-4, pp. 185-191.

Dubrous, F. M. and Harrison, S. J., 1985. Effects of solar simulator lamp spectrum on solar collector test results, in: *Intersol 85 ISES Congress*, Montreal, Canada, pp. 1274-1278.

Duffle, J. A. and Beckman W. A., 1980. *Solar Engineering of Thermal Processes*. John Wiley & Sons, New York.

Electrical & Mechanical Services Department, HKSAR. 2002. *Study on the Potential Applications of Renewable Energy in Hong Kong: Stage 1 Study Report*, EMSD, The Government of the Hong Kong Special Administrative Region.

Electrical & Mechanical Services Department, HKSAR. 2005. G*overnment funded projects utilizing renewable energy resources*, [Online] Available at: http://www.emsd.gov.hk/emsd/eng/sgi/re.shtml

Evans, D. L., 1981. Simplified method for predicting photovoltaic array output, *Solar Energy*, Vol. 27, no. 6, pp. 555-560.

Furler, R.A., 1991. Angular dependence of optical properties of homogeneous glasses, *ASHRAE Transaction.*, Vol. 97, pt. 2, pp. 1129-1133.

Gueymard, C., 1989. A simplified model for the computation of radiation transmission through a series of semi-transparent plates, *Solar Energy*, Vol. 42, no. 6, pp. 433-440.

Hamdy, M. A., 1994. A new model for the current-voltage output characteristics of photovoltaic modules, *Journal of Power Sources*, Vol. 50, pp. 11-20.

Harrison, S. J. and Dubrous, F. M., 1990. Determination of window thermal characteristics using solar-simulator-based test method, *ASHRAE Transaction*, Vol. 96, pt. 1, pp. 912-919.

Harrison, S. J. and Dubrous, F. M., 1992. Uncertainties in the evaluation of window SHGC and U-values measured using an indoor solar simulator facility, *ASHRAE Transaction*, Vol. 98, pt. 2, pp. 638-644.

Harrison, S. J. and Wonderen, S. J., 1998. Evaluation of solar heat gain coefficient for solar-control glazings and shading devices, *ASHRAE Transaction*, Vol. 104, pt. 1b, pp. 1051-1061.

Hay, J. E. and Davies, J. A., 1979. Calculation of the solar radiation incident on an inclined surface, Proceeding of First Canadian Solar Radiation Data Workshop, Toronto, pp. 59-72.

Hovel, H. J., 1975. *Semiconductors and semimetals*, Vol. 11, Academic Press, New York.

IEA Photovoltaic Power Systems Programme, 2005. *International statistics Trends in photovoltaic applications in selected IEA countries*, [Online] Available at: http://www.oja-services.nl/iea-pvps/isr/index.htm

IEC 904-9: 1995(E), *Photovoltaic devices – Part 9: Solar simulator performance requirements*, International Standard.

IESNA, 2000. *The IESNA lighting handbook: reference & application*, 9th edition, Illuminating Engineering Society of North America, New York.

Infield, D. et al., 2004. Thermal performance estimation for ventilated PV facades, *Solar Energy*, Vol. 76, pp. 93-98.

Ismail, K.A.R. and Henriquez, J.R., 1998. U-values, optical and thermal coefficients of composite glass systems, *Solar Energy Materials & Solar Cells*, Vol. 52, pp. 155-182.

Ismail, K.A.R. and Henriquez, J.R., 2003. Modeling and simulation of a simple glass window, *Solar Energy Materials & Solar Cells*, Vol. 80, pp. 355-374.

Jones, A. D. and Underwood, C. P., 2001. A thermal model for photovoltaic systems, *Solar Energy*, Vol. 70, no. 4, pp. 349-359.

Jones, A. D. and Underwood, C. P., 2002. A modeling method for building-integrated photovoltaic power supply, *Building Services Engineering Research and Technology*, Vol. 23, no. 3, pp. 167-177.

Jones, W. P., 2001. *Air conditioning engineering*, 5th ed., Butterworth-Heinemann, Oxford.

Karlsson, J. and Roos, A., 2000. Modeling the angular behaviour of the total solar energy transmittance of windows, *Solar Energy*, Vol. 69, no. 4, pp. 321-329.

Klems, J. H., 1989. U-values, solar heat gain, and thermal performance: recent studies using the MoWiTT, *ASHRAE Transaction*, Vol. 95, pt. 1, pp. 609-617.

Klucher, T. M., 1979. Evaluation of models to predict insolation on tilted surfaces, *Solar Energy*, Vol. 23, pp. 111-114.

Krauter, S. and Hanitsch, R., 1996. Actual optical and thermal performance of PV-modules, *Solar Energy Materials and Solar Cells*, Vol. 41-42, pp. 557-574.

Lam, J. C. and Li, D. H. W., 1996. Correlation between global solar radiation and its direct and diffuse components, *Building and Environment*, Vol. 31, no. 6, pp. 527-535.

Lasnier, F. and Ang, T. G., 1990. *Photovoltaic engineering handbook*. Adam Hilger Ltd, Bristol, UK.

Li, D. H. W., and Lam, J. C., 2000. Evaluation of slope irradiance and illuminance models against measured Hong Kong data, *Building and Environment*, Vol. 35, pp. 501-509.

Li, D. H. W., Lam, J. C., Lau, C. C. S., 2002. A new approach for predicting vertical global solar irradiance, *Renewable Energy*, Vol. 25, pp. 591-606.

Liesen, R. J. and Pedersen, C. O., 1997. An evaluation of inside surface heat balance models for cooling load calculations, *ASHRAE Transactions*, Vol. 103, pp. 485-502.

Lo, Edward W. C., 2005. Overview of Building Integrated Photovoltaic (BIPV) Systems in Hong Kong, *Proceedings of International Conference on Alternative Energy*, Hong Kong, China, pp. 45-52.

Loveday, D.L., Taki, A.H., 1996. Convective heat transfer coefficients at a plane surface on a full-scale building façade, *Int. J. Heat Mass Transfer*, Vol. 39, no. 8, pp. 1729-1742.

Lu, L., 2004. *Investigation on characteristics and application of hybrid solar-wind power generation systems*, Doctoral Thesis, The Hong Kong Polytechnic University.

Mahmoud, M., and Nabhan, I., 1990. Determination of optimum tilt angle of single and multi rows of photovoltaic arrays for selected sites in Jordan, *Solar & Wind Technology*, Vol. 7, no. 6, pp. 739-745.

Markvart, T., (Eds.), 2000. *Solar electricity*, John Wiley & Sons.

McQuiston, F. C., Spitler, J. D., 1992. *Cooling and heating load calculation manual*, 2nd ed., American Society of Heating, Refrigerating and Air-Conditioning Engineers, New York.

Merrigan, J. A., 1975. *Sunlight to electricity: prospects for solar energy conversion by Photovoltaics*, The MIT Press, Cambridge.

Meyer, E. L. and Dyk, E. E. v., 2000. Development of energy model based on total daily irradiation and maximum ambient temperature, *Renewable Energy*, Vol. 21, pp. 37-47.

Miyazaki, T., et al., 2005. Energy saving of office buildings by the use of semi-transparent solar cells for windows, *Renewable Energy*, Vol. 30, issue 3, pp. 281-304.

Moshfegh, B. and Sandberg, M., 1998. Flow and heat transfer in the air gap behind photovoltaic panels, Renewable and Sustainable *Energy Reviews*, Vol. 2, pp. 287-301.

Muneer, T., 1990. Solar radiation model for Europe, *Building Services Engineering Research and Technology*, Vol. 11(4), pp. 153-163.

Overstraeten, R. J. Van and Mertens, R. P., 1986. *Physics, Technology and Use of Photovoltaic*, Adam Hilger Ltd, Bristol, UK.

Pearsall, N. M. and Wilshaw, A. R., 1996. Performance analysis of the Northumberland building photovoltaic façade, *Proceedings of 25th Photovoltaics Specialist Conference*, Washington, DC, USA, pp. 1247-1250.

Pedersen, C. O., Fisher, D. E., Liesen, R. J., 1997. Development of a heat balance procedure for calculating cooling loads, *ASHRAE Transactions*, Vol. 103, pp. 459-468.

Perez, R., Ineichen, P., Seals, R., 1990. Modeling daylight availability and irradiance components from direct and global irradiance, *Solar Energy*, Vol. 44, no. 5, pp. 271-289.

Perez, R., Seals, R., Ineichen, P., Stewart, R., Menicucci, D., 1987. A new simplified version of the Perez diffuse irradiance model for tilted surfaces, *Solar Energy*, vol. 39, no. 3, pp. 221-231.

Perez, R., Stewart, R., Arbogast, C., Seals, R., Scott, J., 1986. An anisotropic hourly diffuse radiation model for sloping surfaces: description, performance validation, site dependency evaluation, *Solar Energy*, Vol. 36, no. 6, pp. 481-497.

Price, B. A. and Smith, T. F., 1995. Thermal response of composite building envelopes accounting for thermal radiation, *Energy Conversion and Management*, Vol. 36, no. 1, pp. 23-33.

Reindl, D. T., Beckman, W. A., Duffie, J. A., 1990. Evaluation of hourly tilted surface radiation models. *Solar Energy*, Vol. 45, no. 1, pp. 9-17.

Reinhart, C. F. and Herkel, S., 2000. The simulation of annual daylight illuminance distributions – a state-of-art comparison of six RADIANCE-based methods, *Energy and Buildings*, Vol. 32, pp. 167-187.

Robinson, P. and Littler, J., 1993. Advanced glazing: outdoor test room measurements, performance prediction and building thermal simulation, *Building and Environment*, Vol. 28, no. 2, pp. 145-152.

Rubin, M, 1982. Calculating heat transfer through windows, *Energy Research*, Vol. 6, pp. 341-349.

Rubin, M., Rottkay, K., Powles, R., 1998. Window optics, *Solar Energy*, Vol. 62, no. 3, pp. 149-161.

Saraiji, R. M. N. and Mistrick, R. G., 1993. The Evaluation of determinant sky parameters for daylighting CUs, *Journal of the Illuminating Engineering Society*, Vol. 22, no. 1, pp. 131-137.

Schoen, T. J. N., 2001. Building-integrated PV installations in the Netherlands: examples and operational experiences, *Solar Energy*, Vol. 70, no. 6, pp. 467-477.

Shariah, A., Al-Akhras, M., Al-Omari, I.A., 2002. Optimizing the tilt angle of solar collectors. *Renewable Energy*, Vol. 26, pp. 587-598.

Skiba, M., Mohr, M., Unger, H., 1996. Comparative assessment and validation of models estimating diffuse irradiation on inclined planes, *1996 EuroSun Congress*, pp. 1568-1573.

Sonnenenergie, D. G., 2005**.** *Planning and installing photovoltaic systems: a guide for installers, architects, and engineers*, James & James/Earthscan, London.

Strong, S. J., 1996. World overview of building-integrated photovoltaics, *Proceedings of 25th Photovoltaics Specialist Conference*, Washington, DC, USA, pp. 1197-1202.

Temps, R. C. and Coulson, K. L., 1977. Solar radiation incident upon slopes of different orientations, *Solar Energy*, Vol. 19, pp. 179-184.

The Council for Sustainable Development, 2005. *The First Sustainable Development Strategy for Hong Kong of Sustainable Development*, [Online] Available at: http://www.susdev.org.hk/en/Strategy/index.html

Threlkeld, James L., 1970. *Thermal environmental engineering***,** Englewood Cliffs, N.J., Prentice-Hall.

Tiris, M., and Tiris C., 1997. Optimum collector slope and model evaluation: case study for Gebze, Turkey, *Energy Conversion and Management*, Vol. 39, no. 3-4, pp. 167-172.

To, D. W. T. et al., 2002. Potential energy saving for a side-lit room using daylight-linked fluorescent lamp installations, *Lighting Research and Technology*, Vol. 34, no. 2, pp. 121-133.

Tregenza, P. R., 1995. Mean daylight illuminance in rooms facing sunlit streets, *Building and Environment*, Vol. 30, no. 1, pp. 83-89.

Utrillas, M. P., Martinez-Lozano, J. A., Casanovas, A. J., 1991. Evaluation of models for estimating solar irradiation on vertical surfaces at Valencia, Spain, *Solar Energy*, Vol. 47, no. 3, pp. 223-229.

Vartiainen, E., 2000. *Daylight modeling and optimization of solar facades*, Doctoral Thesis, Helsinki University of Technology, Helsinki University of Technology Publications in Energy Engineering Physics.

Wong, W. L., Ngan, K. H., 1993. Selection of an "example weather year" for Hong Kong, *Energy and Buildings*, Vol. 19, pp. 313-316.

Wright, John L., and Sullivan, Harry F., 1995. A two-dimensional numerical model for glazing system thermal analysis, *ASHRAE Transactions*, Vol. 101, pt. 1, pp. 819-831.

Yakup, M., Malik, A.Q., 2001. Optimum tilt angle and orientation for solar collector in Brunei Darussalam, *Renewable Energy*, Vol. 24, pp. 223-234.

Yang, H and Fung, Y., 2005. Building-integrated photovoltaics: its' past, present and future applications in Hong Kong, *Proceedings of 15th International Photovoltaic Science and Engineering Conference*, Shanghai, China.

Yang, H. and Fung, Y., 2003. Building-integrated photovoltaic application – its practice in Hong Kong, *Proceedings of 3rd World Conference on Photovoltaic Energy Conversion*, Osaka, Japan.

Yang, H., Burnett, J. and Ji, J., 2000. Simple approach to cooling load component calculation through PV walls, *Energy and Buildings*, Vol. 31, pp. 285-290.

Yik, F. W. H., Burnett, J., and Prescott, I., 2001. Predicting air-conditioning energy consumption of a group of buildings using different heat rejection methods, *Energy and Buildings*, Vol. 33, pp. 151-166.

Yik, Francis W. H., Chung, T. M., Chan, K. T., 1995. A method to estimate direct and diffuse radiation in Hong Kong and its accuracy, *HKIE Transactions*, Vol. 2, no. 1, pp. 23-29.

Yoo, S. and Lee, E, 2002. Efficiency characteristic of building integrated photovoltaics as a shading device, *Building and Environment*, Vol. 37, pp. 615-623.

Zhu, Z., Zhu, X., and Sun, J., 2002. Numerical analysis of heat transfer in a photovoltaic panel, I: Indoor cases, *International Communications in Heat and Mass Transfer*, Vol. 29, issue 4, pp. 433-575.

Zondag, H.A., de Vries, D.W., van Helden, W.G.J., van Zolingen, R.J.C., van Steenhoven, A.A., 2003. The yield of different combined PV-thermal collector designs, *Solar Energy*, Vol. 74, pp. 253-269.

Zuhairy, A. A., Sayigh, A. A. M., 1995. Simulation and modeling of solar radiation in Saudi Arabia, *Renewable Energy,* Vol. 6, no. 2, pp. 107-118.

APPENDIX

Source code of the SPVHG model

```
#include "stdafx.h"
#include "stdlib.h"
#include "stdio.h"
#include "string.h"
#include "math.h"
#include <iostream.h>

#define MM 100

double tmpdtb(int p, double time, int Q);
double tilt_rad();
double Int_temp[MM+1];
double temp_trans[MM+1];            //current temp
double lasttemp_trans[MM+1];        //last result
double temp_pv[MM+1];                       //current temp
double lasttemp_pv[MM+1];                   //last result
int getlast_trans(char *filename, double temp_trans[]);
int getlast_pv(char *filename, double temp_pv[]);
double rad_heat_trans(double R, double BOLT, double temp_trans[], int p, int Q);
double rad_heat_pv(double R, double BOLT, double temp_pv[], int p, int Q);

        #define NN 10

        double A_trans[NN];
        double MRT_trans[NN];
        double A_MRT_trans[NN];
        double EMIT[NN];
        double EMIT_MRT_trans[NN];
        double T_trans[NN];
        double T_MRT_trans[NN];
        double T_AVE_trans[NN];
        double F_MRT_trans[NN];

        double A_pv[NN];
        double A_MRT_pv[NN];
        double EMIT_MRT_pv[NN];
        double T_pv[NN];
        double T_MRT_pv[NN];
        double T_AVE_pv[NN];
        double F_MRT_pv[NN];

float TO, TR;
double DX, DTIME;
double THDFF_G, ABSP_P, ABSP_PV, COND_G, COND_P, EMIT_G;
double EXCOEF, TRAN_P;
double RATED_PV_EFF;
double PV_EFF;
const double Beta    = 0.0045;
```

```
double Fo;
int L1, L2;
int M, m;
const double BOLT = 5.669e-8;          //unit: W/m2K4
double G_TOT_TILT, G_BM_TILT, G_GD_TILT, G_SKY_TILT;
double BM_IN_ANG;                      //Theta (incident angle)
double n;                              //refrective index
float G;                               //user input parameters (G in J/m^2)
float YR_DAY, HR;                      //user input parameters
double R;                              //PV to trans glass ratio
int ITR_INT;                           //Iteration interval in second (e.g. 5 min, 15 min, 1
hour etc...)
float STD_TIME;                                //local standard time
float r;                               //time index, one increment with one iteration
interval(ITR_INT)
float WIND_SPD, WIND_DIR;              //wind speed and wind direction
double FACADE_H;
double FACADE_W;
double WWR;
double GLZ_H;
double GLZ_AREA;
double t_sol, y;
double RAD_HTGAIN_trans;
double RAD_HTGAIN_pv;


main()
{
        int N;                         //number of hour to be calculated
        int L;                         //Total number of iteration in whole calculation
        FILE *fp2;

        cout << "Please input L1 and L2 (should be integer in mm):\n";
        cin >> L1 >> L2;
        cout << "Please input dx and dt:\n";
        cin >> DX >> DTIME;
        cout << "Please input THDFF_G, ABSP_P, ABSP_PV, COND_G, COND_P, EMIT_G:\n";
        cin >> THDFF_G >> ABSP_P >> ABSP_PV >> COND_G >> EMIT_G;
        cout << "Please input EXCOEF and TRAN_P\n";
        cin >> EXCOEF >> TRAN_P;
        cout << "Please input efficiency of the PV cells:\n";
        cin >> RATED_PV_EFF;
        cout << "Please input height the facade:\n";
        cin >> FACADE_H;
        cout << "Please input width the facade:\n";
        cin >> FACADE_W;
        cout << "Please input window-to-wall ratio:\n";
        cin >> WWR;
        cout << "Please input Refrective index of the glass (n):\n";
        cin >> n;
        cout << "Please input PV area ratio:\n";
        cin >> R;
        cout << "Please input the iteration interval in second:\n";
        cin >> ITR_INT;
        cout << "Please input the number of hour to be iterated (N):\n";
```

```
cin >> N;

L = N * (3600/ITR_INT);

double ELEMT_BG = (L1*0.001)/DX;
double ELEMT_FG = (L2*0.001)/DX;

int at_L1 = int(ELEMT_BG);
int at_L2 = int(ELEMT_FG);

cout << "ELEMT_BG = " << ELEMT_BG << "\n";
cout << "int of ELEMT_BG = " << int(ELEMT_BG) << "\n";
cout << "ELEMT_FG = " << ELEMT_FG << "\n";
cout << "int of ELEMT_FG = " << int(ELEMT_FG) << "\n";

if (int(ELEMT_BG)==ELEMT_BG && int(ELEMT_FG)==ELEMT_FG)
{

	Fo = (THDFF_G * DTIME)/(DX * DX);
	if (Fo <= 0.5)				//check for convergency (Fo)
	{

		M = at_L2;

		fp2 = fopen("C:\\Documents and Settings\\02902015r\\My Documents\\From
HX\\1989 weather data\\1989 weth_1 hr int_norad.txt", "r");
		fscanf(fp2,"%f %f %f %f %f %f %f %f %f",&YR_DAY, &r, &HR, &STD_TIME,
&TO, &TR, &G, &WIND_SPD, &WIND_DIR);

		getlast_trans("last_result_trans.txt", temp_trans);
		getlast_pv("last_result_pv.txt", temp_pv);

		if (getlast_trans("last_result_trans.txt", temp_trans) == -1 &&
getlast_pv("last_result_pv.txt", temp_pv) == -1)
		{
			//Initial condition (Trans): time=0
			for(m=0; m<=M; m++)
			{
				temp_trans[m] = ((TO - TR)/(L2*0.001)) * m * DX + TR;
				Int_temp[m] = temp_trans[m];
			}

			//Initial condition (PV): time=0
			for(m=0; m<=M; m++)
			{
				temp_pv[m] = ((TO - TR)/(L2*0.001)) * m * DX + TR;
			}
			cout << "No last data file exists! Use linear initial condition.\n";

		}else cout << "Last data files have been get!\n";

		fp2 = fopen("C:\\Documents and Settings\\02902015r\\My Documents\\From
HX\\1989 weather data\\1989 weth_1 hr int_norad.txt", "r");
		if (!fp2) { exit(1); }
```

```
//============================== Q loop start ==============================
                int Q;
                for(Q=0; Q<=L-1; Q++)
                {
                        fscanf(fp2,"%f %f %f %f %f %f %f %f %f\n",&YR_DAY, &r, &HR,
&STD_TIME, &TO, &TR, &G, &WIND_SPD, &WIND_DIR);

                        tilt_rad();

                        int p;
                        for(p=1; p<=ITR_INT/DTIME; p++)
                        {
                                tmpdtb(p, ITR_INT*Q+p*DTIME, Q);
                        }

                }       //Q loop end


//=========================== Q loop end================================

            }
            else cout << "Criterion for numerical stability is not fulfilled because Fo is greater
than 0.5.";

        }
        else cout << "The total number of finite element is not an integer, please re-enter L1, L2
and dx.";

        return 0;
}
//++++++++++++++++++++++++++++ Main () end ++++++++++++++++++++++++++++++

int getlast_trans(char *filename, double temp_trans[])
{
        FILE *fp5;
        int m=0;
        float tmp_trans;

        if(fp5 = fopen("C:\\Documents and Settings\\02902015r\\My Documents\\My
research\\Heat_tran_sim\\Temp result\\previous step results\\last_result_trans.txt", "r"))
        {
                for(m=0; !feof(fp5); m++)
                {
                        fscanf(fp5, "%f\n", &tmp_trans);
                        temp_trans[m] = tmp_trans;
                }
                return 0;
        }else return -1;
}

int getlast_pv(char *filename, double temp_pv[])
{
        FILE *fp6;
        int m=0;
        float tmp_pv;
```

```
	if(fp6 = fopen("C:\\Documents and Settings\\02902015r\\My Documents\\My
research\\Heat_tran_sim\\Temp result\\previous step results\\last_result_pv.txt", "r"))
	{
		for(m=0; !feof(fp6); m++)
		{
			fscanf(fp6, "%f\n", &tmp_pv);
			temp_pv[m] = tmp_pv;
		}
		return 0;
	}else return -1;
}

//********************************************** tmpdtb () **********************************************
double tmpdtb(int p, double time, int Q)
{

		const double pi = 3.1415926535;
		double BM_RE_ANG, GD_IN_ANG, GD_RE_ANG, SKY_IN_ANG,
SKY_RE_ANG;
		double TILT = 90;
				//beta
		double r_BM, r_GD, r_SKY, a_BM_FG, a_GD_FG, a_SKY_FG, a_BM_BG,
a_GD_BG, a_SKY_BG;	//reflectivity, absorptivity.
		double TRAN_BM_FG, TRAN_GD_FG, TRAN_SKY_FG;
		double TRAN_BM_BG, TRAN_GD_BG, TRAN_SKY_BG;
		double TRAN_FG, TRAN_BG, TRAN_TOT_OUTG;
		double G_BM_TILT_tau_FG, G_GD_TILT_tau_FG, G_SKY_TILT_tau_FG;
		double G_BM_TILT_tau_BG, G_GD_TILT_tau_BG, G_SKY_TILT_tau_BG;
		double I_TOT_TILT_tau_FG, I_TOT_TILT;
		double I_TOT_HOR;
		double A, B, C, D, E, F;
		double hr, ho;
		double G_TOT_TILT_tau_FG;
		double G_TOT_TILT_tau_BG;
		double heat_trans;
		double heat_pv;
		double heat;
		double CONV_HTGAIN_trans;
		double SOL_HTGAIN;
		double CONV_HTGAIN_pv;

		FILE *fp;

		GD_IN_ANG = 90 - 0.5788*TILT + 0.002693*pow(TILT,2);		//Theta 1,
ground
		SKY_IN_ANG = 59.68 - 0.1388*TILT + 0.001497*pow(TILT,2);	//Theta 1,
sky

		BM_RE_ANG = (asin((sin(BM_IN_ANG*pi/180))/n))*180/pi;		//Theta 2,
beam
		GD_RE_ANG = (asin((sin(GD_IN_ANG*pi/180))/n))*180/pi;		//Theta 2,
ground
		SKY_RE_ANG = (asin((sin(SKY_IN_ANG*pi/180))/n))*180/pi;		//Theta
2, sky
```

```
A = BM_IN_ANG-BM_RE_ANG;
B = BM_IN_ANG+BM_RE_ANG;
C = GD_IN_ANG-GD_RE_ANG;
D = GD_IN_ANG+GD_RE_ANG;
E = SKY_IN_ANG-SKY_RE_ANG;
F = SKY_IN_ANG+SKY_RE_ANG;

r_BM = 0.5 * (pow(sin((A)*pi/180),2)/pow(sin((B)*pi/180),2)
            + pow(tan((A)*pi/180),2)/pow(tan((B)*pi/180),2));
r_GD = 0.5 * (pow(sin((C)*pi/180),2)/pow(sin((D)*pi/180),2)
            + pow(tan((C)*pi/180),2)/pow(tan((D)*pi/180),2));
r_SKY = 0.5 * (pow(sin((E)*pi/180),2)/pow(sin((F)*pi/180),2)
            + pow(tan((E)*pi/180),2)/pow(tan((F)*pi/180),2));

a_BM_FG = exp(-EXCOEF*(L1*0.001/(cos(BM_RE_ANG*pi/180))));
a_GD_FG = exp(-EXCOEF*(L1*0.001/(cos(GD_RE_ANG*pi/180))));
a_SKY_FG = exp(-EXCOEF*(L1*0.001/(cos(SKY_RE_ANG*pi/180))));
a_BM_BG = exp(-EXCOEF*((L2-L1)*0.001/(cos(BM_RE_ANG*pi/180))));
a_GD_BG = exp(-EXCOEF*((L2-L1)*0.001/(cos(GD_RE_ANG*pi/180))));
a_SKY_BG = exp(-EXCOEF*((L2-L1)*0.001/(cos(SKY_RE_ANG*pi/180))));

TRAN_BM_FG = (pow((1-r_BM),2) *
a_BM_FG)/(1-pow(r_BM,2)*pow(a_BM_FG,2));          //tau,beam,fg
TRAN_GD_FG = (pow((1-r_GD),2) *
a_GD_FG)/(1-pow(r_GD,2)*pow(a_GD_FG,2));          //tau,gd,fg
TRAN_SKY_FG = (pow((1-r_SKY),2) *
a_SKY_FG)/(1-pow(r_SKY,2)*pow(a_SKY_FG,2));      //tau,sky,fg
TRAN_BM_BG = (pow((1-r_BM),2) *
a_BM_BG)/(1-pow(r_BM,2)*pow(a_BM_BG,2));          //tau,beam,bg
TRAN_GD_BG = (pow((1-r_GD),2) *
a_GD_BG)/(1-pow(r_GD,2)*pow(a_GD_BG,2));          //tau,gd,bg
TRAN_SKY_BG = (pow((1-r_SKY),2) *
a_SKY_BG)/(1-pow(r_SKY,2)*pow(a_SKY_BG,2));      //tau,sky,bg


G_BM_TILT_tau_FG = G_BM_TILT * TRAN_BM_FG;         //G in J/m^2
G_GD_TILT_tau_FG = G_GD_TILT * TRAN_GD_FG;
G_SKY_TILT_tau_FG = G_SKY_TILT * TRAN_SKY_FG;

G_BM_TILT_tau_BG = G_BM_TILT * TRAN_BM_BG;         //G in J/m^2
G_GD_TILT_tau_BG = G_GD_TILT * TRAN_GD_BG;
G_SKY_TILT_tau_BG = G_SKY_TILT * TRAN_SKY_BG;

G_TOT_TILT_tau_FG = G_BM_TILT_tau_FG    + G_GD_TILT_tau_FG +
G_SKY_TILT_tau_FG;
G_TOT_TILT_tau_BG = G_BM_TILT_tau_BG    + G_GD_TILT_tau_BG +
G_SKY_TILT_tau_BG;


if(G_TOT_TILT !=0)
{
    TRAN_FG = G_TOT_TILT_tau_FG/G_TOT_TILT;
    TRAN_BG = G_TOT_TILT_tau_BG/G_TOT_TILT;
    TRAN_TOT_OUTG = TRAN_FG * TRAN_BG;
```

```
                }else
                {
                        TRAN_FG = 0;
                        TRAN_BG = 0;
                        TRAN_TOT_OUTG = 0;
                }


                I_TOT_TILT_tau_FG = G_TOT_TILT_tau_FG/3600;            //I in W/m^2

                I_TOT_TILT = G_TOT_TILT/3600;

                I_TOT_HOR = G/3600;


                memcpy(lasttemp_trans,temp_trans,sizeof(temp_trans));
        //last temp
                memcpy(lasttemp_pv,temp_pv,sizeof(temp_pv));
        //last temp

                //Facade and glazing geometry
                GLZ_AREA = WWR * (FACADE_W * FACADE_H);
                GLZ_H = GLZ_AREA/FACADE_W;

                //ho calculation
                if (WIND_DIR>=0 && WIND_DIR<=180)             //window due east
                //if (WIND_DIR>=90 && WIND_DIR<=270)          //window due south
                //if (WIND_DIR>=180 && WIND_DIR<=360)               //window due west
                {
                        ho = 2*WIND_SPD + 8.91;               //windward
                }else
                        ho = 1.77*WIND_SPD + 4.93;            //leeward

                //hr calculation
                hr = 1.46 *
pow((fabs(((lasttemp_trans[0]*(1-R)+lasttemp_pv[0]*R))-TR)/GLZ_H), 0.25);

                double ELEMT_BG = (L1*0.001)/DX;
                double ELEMT_FG = (L2*0.001)/DX;

                int at_L1 = int(ELEMT_BG);
                int at_L2 = int(ELEMT_FG);

                //Efficiency of PV cell
                PV_EFF = RATED_PV_EFF * (1 - Beta*(lasttemp_pv[at_L1] - 298));


//********************** temp distribution of Transparent part (start) ******************************

                //Temp at boundary point facing indoor of back-glass
                temp_trans[0] = 2*Fo*lasttemp_trans[1] + (1-2*Fo)*lasttemp_trans[0] +
((2*THDFF_G*DTIME)/(COND_G*DX))

        *(-hr*(lasttemp_trans[0]-TR)-BOLT*EMIT_G*(pow(lasttemp_trans[0],4)-pow(TR,4)))
                                +
```

```
(DTIME*THDFF_G/COND_G)*(I_TOT_TILT_tau_FG*TRAN_P*EXCOEF*exp(-EXCOEF*(L1*0
.001/cos(BM_RE_ANG*pi/180))));


                //Temp at interior points of back-glass
                for (m=1; m<ELEMT_BG; m++)
                {
                        temp_trans[m] = Fo*(lasttemp_trans[m+1]+lasttemp_trans[m-1]) +
(1-2*Fo)*lasttemp_trans[m]
                                +
(THDFF_G*DTIME/COND_G)*(I_TOT_TILT*TRAN_FG*TRAN_P*EXCOEF*exp(-EXCOEF*((L
1*0.001-m*DX)/cos(BM_RE_ANG*pi/180))));
                }

                //Temp at interior points of front-glass
                for (m=(at_L1+1); m<ELEMT_FG; m++)
                {
                        temp_trans[m] = Fo*(lasttemp_trans[m+1]+lasttemp_trans[m-1]) +
(1-2*Fo)*lasttemp_trans[m]
                                +
(THDFF_G*DTIME/COND_G)*(I_TOT_TILT*EXCOEF*exp(-EXCOEF*((L2*0.001-m*DX)/cos(
BM_RE_ANG*pi/180))));
                }


                //Temp at boundary point facing outdoor of front-glass
                temp_trans[at_L2] = 2*Fo*lasttemp_trans[at_L2-1] +
(1-2*Fo)*lasttemp_trans[at_L2] + ((2*THDFF_G*DTIME)/(COND_G*DX))

        *(-ho*(lasttemp_trans[at_L2]-TO)-BOLT*EMIT_G*(pow(lasttemp_trans[at_L2],4)-pow(TO
,4)))
                                + (DTIME*THDFF_G/COND_G)*(I_TOT_TILT*EXCOEF);


                //Temp at interface of front-glass and back-glass
                temp_trans[at_L1] =
0.5*((DX/COND_G)*I_TOT_TILT*TRAN_FG*ABSP_P*1.01 + temp_trans[at_L1-1] +
temp_trans[at_L1+1]);        //trans-abp product; refer to Duffie's book p.183


//**************************** temp distribution of Transparent part (end) ****************************


//****************************** temp distribution of PV part (start) ***********************************

                //Temp at boundary point facing indoor of back-glass
                temp_pv[0] = 2*Fo*lasttemp_pv[1] + (1-2*Fo)*lasttemp_pv[0] +
((2*THDFF_G*DTIME)/(COND_G*DX))

        *(-hr*(lasttemp_pv[0]-TR)-BOLT*EMIT_G*(pow(lasttemp_pv[0],4)-pow(TR,4)));

                //Temp at interior points of back-glass
                for (m=1; m<ELEMT_BG; m++)
                {
                        temp_pv[m] = Fo*(lasttemp_pv[m+1]+lasttemp_pv[m-1]) +
```

```
(1-2*Fo)*lasttemp_pv[m];

                    }

                    //Temp at interior points of front-glass
                    for (m=(at_L1+1); m<ELEMT_FG; m++)
                    {
                          temp_pv[m] = Fo*(lasttemp_pv[m+1]+lasttemp_pv[m-1]) +
(1-2*Fo)*lasttemp_pv[m]
                                +
(THDFF_G*DTIME/COND_G)*(I_TOT_TILT*EXCOEF*exp(-EXCOEF*((L2*0.001-m*DX)/cos(
BM_RE_ANG*pi/180))));
                    }

                    //Temp at boundary point facing outdoor of front-glass
                    temp_pv[at_L2] = 2*Fo*lasttemp_pv[at_L2-1] + (1-2*Fo)*lasttemp_pv[at_L2] +
((2*THDFF_G*DTIME)/(COND_G*DX))

      *(-ho*(lasttemp_pv[at_L2]-TO)-BOLT*EMIT_G*(pow(lasttemp_pv[at_L2],4)-pow(TO,4)))
                                + (DTIME*THDFF_G/COND_G)*(I_TOT_TILT*EXCOEF);


                    //Temp at interface of front-glass and back-glass
                    temp_pv[at_L1] =
0.5*((DX/COND_G)*I_TOT_TILT*TRAN_FG*(ABSP_PV*1.01 - PV_EFF) + temp_pv[at_L1-1] +
temp_pv[at_L1+1]);          //trans-abp product; refer to Duffie's book p.183



//******************************** temp distribution of PV part (end) **********************************

                    //Radiative heat gain (transparent part)
                    rad_heat_trans(R, BOLT, temp_trans, p, Q);

                    //Radiative heat gain (PV part)
                    rad_heat_pv(R, BOLT, temp_pv, p, Q);

                    CONV_HTGAIN_trans = hr*(temp_trans[0] - TR)*(1-R);
                    RAD_HTGAIN_trans = RAD_HTGAIN_trans*(1-R);
                    SOL_HTGAIN = I_TOT_TILT * TRAN_TOT_OUTG * TRAN_P *(1-R);

                    CONV_HTGAIN_pv = hr*(temp_pv[0] - TR)*R;
                    RAD_HTGAIN_pv = RAD_HTGAIN_pv*R;


                    if(SOL_HTGAIN>=0)
                    {
                          SOL_HTGAIN = SOL_HTGAIN;
                    }else SOL_HTGAIN = 0;


                    heat_trans = CONV_HTGAIN_trans + RAD_HTGAIN_trans + SOL_HTGAIN;

                    heat_pv = CONV_HTGAIN_pv + RAD_HTGAIN_pv;
                    heat = heat_trans + heat_pv;
```

```
                double CNTR = ITR_INT*Q/DTIME+p;
                if(CNTR/(ITR_INT/DTIME) == int(CNTR/(ITR_INT/DTIME)))
                {

                //Output results to file
                fp = fopen("C:\\Documents and Settings\\02902015r\\My Documents\\My
research\\Heat_tran_sim\\Temp result\\result.txt", "a+");

                        fprintf(fp, "%0.1f ", CNTR);
                        fprintf(fp, "%0.1f ", time);

                        for (m=0; m<=M; m++)
                        {
                                fprintf(fp, "%0.3f ", temp_trans[m]);
                        }
                        for (m=0; m<=M; m++)
                        {
                                fprintf(fp, "%0.3f ", temp_pv[m]);
                        }

                        fprintf(fp, "%0.3f ", TO);
                        fprintf(fp, "%0.3f ", TR);
                        fprintf(fp, "%0.3f ", I_TOT_TILT);
                        fprintf(fp, "%0.3f ", CONV_HTGAIN_trans);
                        fprintf(fp, "%0.3f ", RAD_HTGAIN_trans);
                        fprintf(fp, "%0.3f ", SOL_HTGAIN);
                        fprintf(fp, "%0.3f ", heat_trans);
                        fprintf(fp, "%0.3f ", CONV_HTGAIN_pv);
                        fprintf(fp, "%0.3f ", RAD_HTGAIN_pv);
                        fprintf(fp, "%0.3f ", heat_pv);
                        fprintf(fp, "%0.3f ", heat);
                        fprintf(fp, "%0.3f ", ho);
                        fprintf(fp, "%0.3f ", hr);
                        fprintf(fp, "%0.3f ", TRAN_TOT_OUTG);
                        fprintf(fp, "%0.3f ", TRAN_FG);
                        fprintf(fp,"\n");
                        fclose(fp);

                }

        return 0;
}

//******************************************** tmpdtb () ***********************************************

//++++++++++++++++++++++++++++++ tilt_rad () ++++++++++++++++++++++++++++++++

double tilt_rad()
{

        double G_BM_HOR, G_DIFF_HOR;
        double Rb, Go, Kt;
        double ZEN_ANG, DCLNE_ANG, HR_ANG;                      //zenith angle,
declination, hr angle
```

```
	double Et, a, b;
	const double RHO = 0.2, TILT = 90, LAT = 22.3, AZI_ANG =0;
	const double pi = 3.1415926535;
	double c, d, e;


	Et = 9.87*(sin((2*(360*(YR_DAY-81)/364))*pi/180))
		- 7.53*(cos((360*(YR_DAY-81)/364)*pi/180))
		- 1.5*(sin((360*(YR_DAY-81)/364)*pi/180));

	y = -5.8/15 + Et/60;

	c = r*(ITR_INT)/60 + 30;				//plus 30 means take the hourly rad
value at half hr time; ie. at 0:30, 1:30, 2:30...etc
	d = y*60;

	t_sol = HR+(c+d)/60;

	//Omega (Hour angle)
	HR_ANG = 15*(HR+((c+d)/60)-12);				//HR = Hour number

	//Delta (Declination angle)
	DCLNE_ANG = 23.45 * sin((360*(284 + YR_DAY)/365)*pi/180);

	//Theta (incedent angle)
	BM_IN_ANG =
(acos((cos(DCLNE_ANG*pi/180))*(sin(LAT*pi/180))*(cos(AZI_ANG*pi/180))*(cos(HR_ANG*pi
/180))
			- (sin(DCLNE_ANG*pi/180))*(cos(LAT*pi/180))*(cos(AZI_ANG*pi/180))
			+
(cos(DCLNE_ANG*pi/180))*(sin(AZI_ANG*pi/180))*(sin(HR_ANG*pi/180))))*180/pi;

	//Theta Z (Zenith angle)
	ZEN_ANG =
(acos((cos(DCLNE_ANG*pi/180))*(cos(LAT*pi/180))*(cos(HR_ANG*pi/180))
			+ (sin(DCLNE_ANG*pi/180))*(sin(LAT*pi/180))))*180/pi;

	Rb = (cos(BM_IN_ANG*pi/180))/(cos(ZEN_ANG*pi/180));

	a = (12*3600*1367/pi)*(1+0.033*cos((360*YR_DAY/365)*pi/180));
	b =
cos(LAT*pi/180)*cos(DCLNE_ANG*pi/180)*(sin(HR_ANG*pi/180)-sin((HR_ANG-15)*pi/180));

	e = 2*pi*(HR_ANG-(HR_ANG-15))/360*sin(LAT*pi/180)*sin(DCLNE_ANG*pi/180);


	Go = a * (b+e);				//Go in J/m^2

	if (Go<=0)
	{
		Kt = 0;
	}
	else
	{
		Kt = G/Go;
```

```
	}

	if (Kt>=0 && Kt<0.325)
	{
		G_DIFF_HOR = G * (1-0.435*Kt);

	}
	else if (Kt>=0.325 && Kt<0.679)
	{
		G_DIFF_HOR = G * (1.41-1.695*Kt);
	}
	else
	{
		G_DIFF_HOR = G * 0.259;
	}

	G_BM_HOR = G - G_DIFF_HOR;

	G_BM_TILT = G_BM_HOR*Rb;
	G_GD_TILT = (G_BM_HOR+G_DIFF_HOR)*RHO*((1-cos(TILT*pi/180))/2);
	G_SKY_TILT =
G_DIFF_HOR*((1-(G_BM_HOR/Go))*((1+cos(TILT*pi/180))/2)*(1+(sqrt(G_BM_HOR/G))*pow(
sin((TILT*pi/180)/2),3))
				+ G_BM_HOR*Rb/Go);

	if (G_BM_TILT>=0)
	{
		G_BM_TILT = G_BM_TILT;
	}else G_BM_TILT = 0;

	if (G_GD_TILT>=0)
	{
		G_GD_TILT = G_GD_TILT;
	}else G_GD_TILT = 0;

	if (G_SKY_TILT>=0)
	{
		G_SKY_TILT = G_SKY_TILT;
	}else G_SKY_TILT = 0;


	if (BM_IN_ANG>=90 || ZEN_ANG>=90)
	{
		G_BM_TILT = 0;
	}

	G_TOT_TILT = G_BM_TILT + G_GD_TILT + G_SKY_TILT;



	return 0;
}
//+++++++++++++++++++++++++++++ tilt_rad () +++++++++++++++++++++++++++++++
```

```
//------------------------------------------ rad_heat_trans() start-------------------------------------------

double rad_heat_trans(double R, double BOLT, double temp_trans[], int p, int Q)
{


	const double RM_D=6, RM_W=8, RM_H=3.6;
	const double GLZ_W=8;
	const double EMIT_G=0.86, EMIT_WALL=0.91;
	float T_WALL=295;					//interior wall surface temp

	int i, j;
	double x_trans=0;
	double y_trans=0;
	double a;

	A_trans[1] = GLZ_H * GLZ_W * (1-R);		//glazing
	A_trans[2] = RM_D * RM_H;				//right side wall, if stand inside rm
and facing the window
	A_trans[3] = RM_W * RM_H;				//back wall
	A_trans[4] = RM_D * RM_H;				//left side wall, if stand inside rm
and facing the window
	A_trans[5] = RM_D * RM_W;				//floor
	A_trans[6] = RM_D * RM_W;				//roof

	//emittance of glass and walls
	EMIT[1] = EMIT_G;
	for (i=2; i<=6; i++)
	{
		EMIT[i] = EMIT_WALL;
	}

	//temperature of glass and walls
	T_trans[1] = temp_trans[0];
	for (i=2; i<=6; i++)
	{
		T_trans[i] = T_WALL;
	}


if (p==1 && Q==0)
{
	for (i=1; i<=6; i++)
	{
		//MRT areas
		for (j=1; j<=6; j++)
		{
			if (i !=j)
			{
				A_MRT_trans[i] += A_trans[j];

			}
		}

		//MRT emittance
```

```
            for (j=1; j<=6; j++)
            {
                if (i !=j)
                {
                    EMIT_MRT_trans[i] += (A_trans[j]*EMIT[j])/A_MRT_trans[i];
                }
            }

            //MRT temperature
            for (j=1; j<=6; j++)
            {
                if (i !=j)
                {
                    T_MRT_trans[i] +=
(A_trans[j]*EMIT[j]*T_trans[j])/(A_MRT_trans[i]*EMIT_MRT_trans[i]);
                }
            }

        }

}else
for (i=1; i<=6; i++)
{
        A_MRT_trans[i] = A_MRT_trans[i];
        EMIT_MRT_trans[i] = EMIT_MRT_trans[i];
        T_MRT_trans[i] = T_MRT_trans[i];

}

            for (i=1; i<=6; i++)
            {

                T_AVE_trans[i] = (T_MRT_trans[i]+temp_trans[0])/2;

                //MRT view factors
                F_MRT_trans[i] =
1/((1-EMIT[i])/EMIT[i]+1+A_trans[i]*(1-EMIT_MRT_trans[i])/(A_MRT_trans[i]*EMIT_MRT_trans
[i]));
            }

        for (j=1; j<=6; j++)
            {
                x_trans +=
BOLT*A_trans[j]*F_MRT_trans[j]*(pow(T_MRT_trans[j],4)-pow(T_trans[j],4));
                y_trans += A_trans[j];
            }

        a = x_trans/y_trans;

        if (i=1)
        {
            RAD_HTGAIN_trans =
4*BOLT*F_MRT_trans[i]*pow(T_AVE_trans[i],3)*(T_trans[i]-T_MRT_trans[i])-a;
        }
```

```
        return 0;

}

//------------------------------------------ rad_heat_trans() end-----------------------------------------------

//------------------------------------------ rad_heat_pv() start-----------------------------------------------

double rad_heat_pv(double R, double BOLT, double temp_pv[], int p, int Q)
{


        const double RM_D=0.8, RM_W=1, RM_H=0.8;
        const double GLZ_W=1;
        const double EMIT_G=0.86, EMIT_WALL=0.91;
        float T_WALL=295;                                       //interior wall surface temp

        int i, j;
        double x_pv=0;
        double y_pv=0;
        double b;

        A_pv[1] = GLZ_H * GLZ_W * R;                    //glazing
        A_pv[2] = RM_D * RM_H;                                  //right side wall, if stand
inside rm and facing the window
        A_pv[3] = RM_W * RM_H;                                  //back wall
        A_pv[4] = RM_D * RM_H;                                  //left side wall, if stand inside
rm and facing the window
        A_pv[5] = RM_D * RM_W;                                  //floor
        A_pv[6] = RM_D * RM_W;                                  //roof

        //emittance of glass and walls
        EMIT[1] = EMIT_G;
        for (i=2; i<=6; i++)
        {
                EMIT[i] = EMIT_WALL;
        }

        //temperature of glass and walls
        T_pv[1] = temp_pv[0];
        for (i=2; i<=6; i++)
        {
                T_pv[i] = T_WALL;
        }



if (p==1 && Q==0)
{

        for (i=1; i<=6; i++)
        {
                //MRT areas
                for (j=1; j<=6; j++)
                {
```

```
                if (i !=j)
                {
                        A_MRT_pv[i] += A_pv[j];

                }
        }

        //MRT emittance
        for (j=1; j<=6; j++)
        {
                if (i !=j)
                {
                        EMIT_MRT_pv[i] += (A_pv[j]*EMIT[j])/A_MRT_pv[i];
                }
        }

        //MRT temperature
        for (j=1; j<=6; j++)
        {
                if (i !=j)
                {
                        T_MRT_pv[i] +=
(A_pv[j]*EMIT[j]*T_pv[j])/(A_MRT_pv[i]*EMIT_MRT_pv[i]);
                }
        }
    }

}else
for (i=1; i<=6; i++)
{
    A_MRT_pv[i] = A_MRT_pv[i];
    EMIT_MRT_pv[i] = EMIT_MRT_pv[i];
    T_MRT_pv[i] = T_MRT_pv[i];

}

        for (i=1; i<=6; i++)
        {
                T_AVE_pv[i] = (T_MRT_pv[i]+temp_pv[1])/2;

                //MRT view factors
                F_MRT_pv[i] =
1/((1-EMIT[i])/EMIT[i]+1+A_pv[i]*(1-EMIT_MRT_pv[i])/(A_MRT_pv[i]*EMIT_MRT_pv[i]));
        }



    for (j=1; j<=6; j++)
        {
                x_pv += BOLT*A_pv[j]*F_MRT_pv[j]*(pow(T_MRT_pv[j],4)-pow(T_pv[j],4));
                y_pv += A_pv[j];
        }

    b = x_pv/y_pv;
```

```
        if (i=1)
        {
                RAD_HTGAIN_pv =
4*BOLT*F_MRT_pv[i]*pow(T_AVE_pv[i],3)*(T_pv[i]-T_MRT_pv[i])-b;
        }

        return 0;

}
//------------------------------------------------ rad_heat_pv() end-----------------------------------------------
```